Gerald Hörack, BSc

Wideband Propagation Channel Model for Ship-to-Shore Communications Considering Sea Surface Effects

MASTERARBEIT

zur Erlangung des akademischen Grades

Diplom-Ingenieur

Masterstudium Space Sciences and Earth from Space

eingereicht an der

Technischen Universität Graz

Betreuer

Ao.Univ.-Prof. Dipl.-Ing. Dr. Erich Leitgeb

Institut für Hochfrequenztechnik

Fakultät für Elektrotechnik und Informationstechnik

Graz, March 2015

EIDESSTATTLICHE ERKLÄRUNG

AFFIDAVIT

Ich erkläre an Eides statt, dass ich die vorliegende Arbeit selbstständig verfasst, andere als die angegebenen Quellen/Hilfsmittel nicht benutzt, und die den benutzten Quellen wörtlich und inhaltlich entnommenen Stellen als solche kenntlich gemacht habe. Das in TUGRAZonline hochgeladene Textdokument ist mit der vorliegenden Masterarbeit identisch.

I declare that I have authored this thesis independently, that I have not used other than the declared sources/resources, and that I have explicitly indicated all material which has been quoted either literally or by content from the sources used. The text document uploaded to TUGRAZonline is identical to the present master‘s thesis.

Datum / Date

Unterschrift / Signature

Wideband Propagation Channel Model for Ship-to-Shore Communications Considering Sea Surface Effects

Master's thesis

Gerald Hörack

Institute of Microwave and Photonic Engineering
Graz University of Technology

in cooperation with

Institute of Communications and Navigation
German Aerospace Center (DLR)

Supervisors: Ao. Univ.-Prof. Dr. Erich Leitgeb (TU Graz)
Dr. Wei Wang (DLR)
Dr. Ronald Raulefs (DLR)

Graz, March 2015

Abstract

The design of future maritime wireless communication systems requires a comprehensive knowledge of the maritime radio channel. The wideband characteristics of the channel are of particular interest for this purpose. To get information about the maritime radio channel, the German Aerospace Center (DLR) performed a broadband channel measurement campaign in the Baltic Sea. The measurements were done in C-band at 5.2 GHz with a bandwidth of 100 MHz, where the transmitter was located on a ship and the receiver on land. Based on the measurement results, three state-of-the-art maritime narrowband channel models, i.e. the Recommendation ITU-R P.1546-2, the Round Earth Loss model and Karasawa's model, are investigated and checked for validity in terms of path loss at 5.2 GHz. The narrowband model results are presented and compared to the measurements as received power as a function of distance between transmitter and receiver. The best agreement with the measurement data is found for Karasawa's model, where a special focus lies on the scattering phenomenon due to the roughness of the sea surface. Furthermore, a maritime wideband channel model for C-band is proposed, based on the physical optics theory. The wideband model takes the shape and the dimensions of the sea surface into account and allows to compute the channel impulse response. The wideband model results are presented and compared to the measurements in terms of power delay profile and time dispersion parameters for different distances between transmitter and receivers.

Kurzfassung

Die Entwicklung zukünftiger, drahtloser Kommunikationssysteme im maritimen Bereich erfordert ein umfassendes Wissen über den maritimen Funkausbreitungskanal. Dafür sind besonders die Breitbandeigenschaften des Kanals von Interesse. Um Informationen über den maritimen Funkausbreitungskanal zu gewinnen, organisierte das Deutsche Zentrum für Luft- und Raumfahrt (DLR) eine Breitband-Messkampagne in der Ostsee. Die Messungen wurden im C-Band bei 5.2 GHz mit einer Bandbreite von 100 MHz durchgeführt, wobei der Sender auf einem Schiff und der Empfänger an Land platziert wurde. Basierend auf den Messergebnissen wurden drei State-of-the-Art Schmalband-Kanalmodelle, im Speziellen das ITU-Modell Recommendation ITU-R P-1546-2, das Round-Earth-Loss-Modell und das Karasawa-Modell auf ihre Gültigkeit bezüglich Übertragungsdämpfungs-Vorhersagen für 5.2 GHz untersucht. Die Modellergebnisse für die Vorhersagen der Übertragungsdämpfung werden in dieser Arbeit als Empfangsleistung abhängig von der Distanz zwischen Sender und Empfänger präsentiert und mit den Messungen verglichen. Die beste Übereinstimmung mit den Messdaten wird durch das Karasawa-Modell erreicht, welches besonderen Fokus auf das Scattering-Phänomen von elektromagnetischen Wellen aufgrund der Rauigkeit der Meeresoberfläche legt. Darüberhinaus wird ein maritimes Breitband-Kanalmodell für Frequenzen im C-Band vorgestellt, welches auf der Theorie der Wellenoptik basiert. Dieses neue Modell berücksichtigt die Form und die Dimensionen der Meeresoberfläche und erlaubt eine Vorhersage der Kanalimpulsantwort. Die Ergebnisse des Breitband-Modells werden mit den Messungen bezüglich des Leistungsverzögerungsdiagramm und der Zeitdispersions-Parameter für unterschiedliche Distanzen zwischen Sender und Empfänger verglichen.

Acknowledgments

First of all the author likes to thank Prof. Erich Leitgeb, the leader of the Optical Communications Group at the Institute of Microwave and Photonic Engineering at Graz University of Technology, for his guidance and helpful advice.
The author gratefully acknowledges the continuous and assistant support of his supervisors Dr. Ronald Raulefs and Dr. Wei Wang, researchers at the Institute of Communications and Navigation of the German Aerospace Center (DLR), during the course of this thesis.
Furthermore the author wishes to thank Dr. Thomas Jost and Michael Walter, also researchers at the Institute of Communications and Navigation of the German Aerospace Center (DLR), for sharing their knowledge in channel modeling and for their helpful contributions to this thesis.
Finally, I want to express my deep gratitude to my family, for their unconditional love and support. Without them, it would not have been possible to carry out this work.

Graz, March 2015 Gerald Hörack

Contents

List of Tables

List of Figures

1 Introduction

Maritime applications have been significantly developed in the last years. The maritime traffic, and therefore also collisions and navigational incidents, are increasing. This trend can especially be observed in offshore regions and in the vicinities of harbors. In order to efficiently manage the growing marine traffic, a large amount of data, like radar and environmental information, needs to be transmitted. Apart from that, expanding ship-based search for natural resources and also Tele-Health applications are reliant on high data rate communication systems. The main maritime communication systems, however, operate in the VHF band where approximately 6 MHz is reserved for the entire worldwide marine communication purpose. For the required high data rate transmission the dedicated bandwidth is not sufficient. Apart from that, satellite based systems are in use, which are able to cover large areas. However, those alternative systems are comparatively expensive and can only offer limited data rates. Therefore, the demand for a future maritime communication system for high data rate applications between ship and land is growing.
In the C-band, spectrum resources are identified by the European Conference of Postal and Telecommunications Administration (CEPT) in association with the European Telecommunications Standards Institute (ETSI) to enable maritime broadband communications in the future. In order to develop such new wireless broadband communication systems, it is essential to understand the properties of the wireless channel, since it considerably influences the systems design.

1.1 Motivation

The development of new algorithms for future wireless communication systems and navigational applications requires detailed knowledge of the maritime radio channel. One possible way to gain information about the characteristics of the wireless channel is to perform channel measurements. In the past years several maritime channel measurement campaigns have already been conducted ([1]). Due to the fact, that each of those campaigns was performed with a narrow bandwidth, they are not suitable for the design and modeling of broadband radio channels. Therefore, a broadband measurement campaign was conducted by the Institute of Communications and Navigation of the German Aerospace Center (DLR) on the Baltic Sea in March 2014. This measurement campaign will be described in detail later in this work.
Based on channel measurements, new models for simulations of communication and navigation applications can be developed. Of particular interest are predictions of the path loss. Although maritime path loss models already exist, none of them is based on broadband measurements. Therefore, a main objective of this thesis is to investigate existing maritime path loss models and to evaluate, how well the models fit to the performed broadband measurements. For this reason, these models and the used propagation mechanisms are explained in detail in the following chapter.

1.2 Contribution

In this thesis three different state-of-the-art maritime channel models are investigated, i.e. the Recommendation ITU-R P.1546-2 [2], the Round Earth Loss (REL) model [3] and Karasawa's model [4]. The Recommendation ITU-R P.1546-2 is a prediction method for terrestrial services for the frequency range 30 - 3000 MHz. It is based on a step-by-step interpolation and/or extrapolation procedure. The REL model considers a two-ray propagation of electromagnetic (EM) waves, consisting of line-of-sight (LOS) signal and specular reflection from the sea surface. This enables a prediction of constructive and destructive interferences. Additional to the two-ray propagation, Karasawa's model uses the Kirchhoff approximation theory, to take scattering phenomena from the sea surface into account. Therefore, a detailed description of the sea surface is required, which is presented at the beginning of the next chapter. Using Karasawa's findings, a path loss model is developed, where the sea surface is divided into small tiles. For each tile the scattering is computed separately. This channel model is denoted as *Physical Optics (PO) Model*. The path loss simulation results of ITU-R P.1546-2, REL model and PO model are then compared with the broadband measurements.
In a further step, the principle of the PO model is used, to develop a wideband channel model. Therefore, a random sea surface is created and divided into small tiles. Since all tiles have different orientations, their normal vectors are used, to compute the scattering from each tile. This allows a prediction of the channel impulse response (CIR), as well as the multipath power. From the CIR, the power delay profile (PDP) and parameters of a multipath channel can be calculated. The comparison between simulated and measured CIRs and channel parameters, respectively, is then presented.

1.3 Structure

This thesis is organized as follows: In chapter 2 the theoretic background considering the mechanisms of electromagnetic (EM) wave propagation over the sea, as well as the modeling of the sea surface is discussed in detail. Moreover, the applied path loss models are introduced and investigated. Chapter 3 contains the description of the conducted broadband channel measurement campaign in the Baltic Sea in Spring 2014. Additionally, results of a preceding internship, which was focused on the visualization of the measurement campaign, are presented. Chapter 4 deals with the evaluation of the three used path loss models for maritime conditions. Here the model predictions are compared to the obtained broadband channel measurement data. In the following chapter 5 a novel wideband propagation model for maritime environments is proposed. This part contains a description of the used modeling approach, as well as the comparison of the results to the measurement data. Chapter 6 shows a summary of the results of this thesis, together with an outlook to future work.

2 Survey of maritime propagation models

This chapter aims to review the theoretical background of electromagnetic wave propagation with interactions on irregular surfaces. In particular the phenomenon of scattering caused by the sea surface is considered. Furthermore three existing models for radio propagation over sea are introduced and investigated.

2.1 Characterization of the sea surface

The shape of the sea surface is irregular and steadily changing. This is mainly caused by environmental effects like wind and tides. Therefore it can be treated as a random process with certain statistical properties. The following subsections discuss the characterization of an irregular or rough surface, like that of the sea. This is done in terms of qualitative considerations of the criteria of roughness and the statistical properties of a rough surface.

2.1.1 Statistical parameters of a rough surface

A random rough surface can be basically described by two fundamental parameters: the standard deviation of the random surface height and the surface correlation length. Throughout this thesis, the standard deviation height (or root-mean-square (RMS) surface height) will be denoted as h_0, and the surface correlation length as l_0. The first parameter h_0 provides information about the height of peaks and valleys of the surface, whereas the second parameter l_0 determines the separation between them. The mean surface provides a reference, from which the coincidental height of the random rough surface is measured. Based on h_0 and l_0, the RMS surface slope β_0 can be derived as a third parameter to describe the shape of a rough surface. These three parameters will be examined in further detail in the following subsections.

2.1.1.1 Standard deviation height

As aforementioned the random surface height h is measured from a reference mean surface. In the following this mean surface is defined as the xy-plane in the Cartesian coordinates, which means, the random surface height $h(x,y)$ is the deviation from the xy-plane in z-direction at given coordinates x and y. Figure 2.1 illustrates the definition of $h(x, y)$, where the y-axis of the Cartesian coordinate systems shows into the paper. Hence, a perfectly smooth random surface would be the mean surface (e.g. the xy-plane) itself. For presentation convenience, $h(x, y)$ is denoted as h in the following. The mean value (which will be denoted by the angle brackets $\langle\rangle$ throughout this work) of the surface height h is assumed to be

$$\langle h \rangle = 0. \tag{2.1}$$

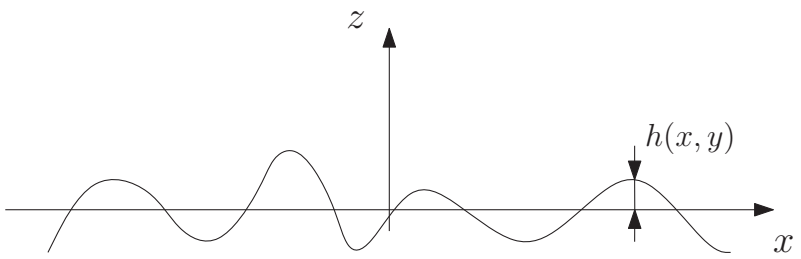

Figure 2.1: Surface height of a rough surface

To obtain the surface parameter h_0, the statistical distribution of the surface height, i.e. the probability density function (pdf) of h, has to be specified. Natural surfaces are usually described by a Gaussian distribution ([5]). Therefore, the pdf of the surface height h is defined as

$$p(h) = \frac{1}{\sqrt{2\pi}h_0} \exp(-\frac{h^2}{2h_0^2}), \tag{2.2}$$

with standard deviation height h_0 and zero mean ($\langle h \rangle = 0$). The RMS surface height h_0 is then given by

$$h_0 = \sqrt{\langle h^2 \rangle} = \sqrt{\left[\int_{-\infty}^{+\infty} h^2 p(h) dh\right]}. \tag{2.3}$$

2.1.1.2 Surface correlation length

The determination of the surface correlation length l_0, is based on an appropriate formulation of the surface auto correlation function (ACF). The ACF is considered in terms of the surface height h, which is a function of (x, y). Therefore, the surface correlation function for two points on the surface at positions (x_1, y_1) and (x_2, y_2) is defined as

$$B(x_1, x_2, y_1, y_2) = \langle h(x_1, y_1) h(x_2, y_2) \rangle \tag{2.4}$$

and consequently its normalized version is

$$C(x_1, x_2, y_1, y_2) = \frac{\langle h(x_1, y_1) h(x_2, y_2) \rangle}{h_0^2}. \tag{2.5}$$

A further assumption is that the randomly changing surface height h is isotropic with x and y ([5]). This means that the value of the surface correlation function is constant for a fixed lateral distance between two points on the two-dimensional rough surface for all azimuthal directions. This enables the simplified representation of the normalized surface correlation function as

$$C(\xi) = \frac{\langle h(x_1, y_1) h(x_2, y_2) \rangle}{h_0^2}, \tag{2.6}$$

where ξ is the lateral displacement between the two positions (x_1, y_1) and (x_2, y_2) and is defined as

$$\xi = \sqrt{(x_1 - x_2)^2 + (y_1 - y_2)^2}. \tag{2.7}$$

The correlation function of a random rough surface decreases with increasing lateral separation ξ. The surface correlation length l_0 is now defined as the displacement, where

$$C(l_0) = \frac{1}{e} \approx 0.368 \tag{2.8}$$

with the mathematical constant $e \approx 2.71828$ (Euler's number).
The models for EM scattering from random rough surfaces considered in this thesis ([6], [7]) are using closed forms of the normalized correlation function, which depend on the lateral displacement and the surface correlation length. According to literature, the most common forms are the Gaussian and the exponential correlation function ([5] page 196). They are defined as

$$\text{Exponential:} \qquad C(\xi) = \exp(-\frac{\xi}{l_0}) \tag{2.9}$$

$$\text{Gaussian:} \qquad C(\xi) = \exp(-\frac{\xi^2}{l_0^2}) \tag{2.10}$$

Since we focus on EM scattering, the Gaussian form is used in this thesis, similar to the findings in [6].

2.1.1.3 Surface slope

To describe a random rough surface the two previously discussed parameters h_0 and l_0 are sufficient. However, because the EM scattering model proposed in [6] utilizes the RMS surface slope β_0, this parameter will also be examined in more detail. As mentioned before in Subsection 2.1.1, the RMS surface slope can be calculated from the RMS surface height and the surface correlation length. This derivation is presented in the following and is closely referred to [5] (page 423 et seq.). The surface slope will be denoted by β.
Due to the definitions in Eq. (2.4) and Eq. (2.5), the surface correlation function $B(\xi)$ can be expressed as

$$B(\xi) = h_0^2 C(\xi), \tag{2.11}$$

which we use later.
Proceeding from the previously made assumption that the randomly changing surface height *h(x,y)* is isotropic with x and y, the two-dimensional rough surface can be simplified as a one-dimensional height profile *h(x)* in the xz-plane. Based on this assumption, the surface slope at a certain position x is given as

$$\beta(x) = \lim_{\Delta x \to 0} \frac{h(x + \Delta x) - h(x)}{\Delta x}, \tag{2.12}$$

and the average of β^2 is represented by

$$\begin{aligned} \langle \beta(x)^2 \rangle &= \lim_{\Delta x \to 0} \left\langle \frac{h^2(x + \Delta x) - 2h(x)h(x + \Delta x) + h^2(x)}{(\Delta x)^2} \right\rangle \\ &= \lim_{\Delta x \to 0} \left[\frac{h_0^2 - 2h_0^2 C(\Delta x) + h_0^2}{(\Delta x)^2} \right] \\ &= 2h_0^2 \lim_{\Delta x \to 0} \left[\frac{1 - C(\Delta x)}{(\Delta x)^2} \right], \end{aligned} \tag{2.13}$$

where $C(\Delta x)$ is the normalized surface correlation function for a lateral displacement $\xi = \Delta x$. $C(\Delta x)$ can be written as a Taylor series around $\Delta x = 0$. Therefore, the derivatives of $C(\Delta x)$ are required, where $C'(\Delta x)$ denotes the first derivative, $C''(\Delta x)$ the second derivative and so on. After the Taylor expansion of $C(\Delta x)$ the above expression can be written as

$$\langle \beta(x)^2 \rangle = 2h_0^2 \lim_{\Delta x \to 0} \left[\frac{1 + \left[1 - C'(0)\Delta x + C''(0)\frac{(\Delta x)^2}{2} + ... \right]}{(\Delta x)^2} \right]. \tag{2.14}$$

Since $C(\xi)$ is an even function, we can use its properties, to simplify Eq. (2.14). The Taylor series of an even function at the origin (i.e. $\Delta x = 0$), only contains even powers. The terms with odd powers cancel out. Furthermore, the even form causes the second derivative of the correlation function $C''(\Delta x)$ to be negative. Hence, Eq. (2.14) can be approximated by taking only the second order term into account as

$$\langle \beta(x)^2 \rangle \approx h_0^2 \left[-C''(0) \right], \tag{2.15}$$

and the expression for the RMS surface slope results in

$$\beta_0 = \sqrt{\langle \beta(x)^2 \rangle} = \sqrt{-h_0^2 C''(0)}. \tag{2.16}$$

Especially for a Gaussian surface correlation function as given in Eq. (2.10) the RMS surface slope can be expressed in terms of the RMS surface height and the surface correlation length as

$$\beta_0 = \frac{\sqrt{2} h_0}{l_0}. \tag{2.17}$$

2.1.2 Definition of surface roughness

In the context of rough surfaces an elementary question arises, which has already been discussed several times in the past ([6], [5], [7]). Under which conditions could a surface be considered as electromagnetically "rough"? However, there is no well-defined bound between a smooth and a rough surface. In practice the so-called Rayleigh roughness criterion is a widely used method to determine or estimate the degree of roughness of a surface (see [7] page 826 et seq.). Another definition of surface roughness, which can also be found in this literature, is obtained by the Fraunhofer roughness criterion. Both criteria will be discussed in more detail in the following subsections.

Rayleigh roughness criterion

A typical geometry of a rough surface is shown in Figure 2.2. Two incident rays are reflected from the surface at points A and B. If the surface is perfectly smooth (represented by the horizontal dashed line), there will be no path difference between the reflected rays and thus also no phase difference. Figure 2.2(a) represents two rays, impinging orthogonally on a rough surface, where point B is higher than A by a height difference Δh. Therefore, the ray reflected at point B has to travel a shorter distance by $2\Delta h$. This results in a phase difference between the two reflected rays of

$$\Delta\phi = 2k\Delta h = \frac{4\pi\Delta h}{\lambda}, \tag{2.18}$$

where

$$k = 2\pi/\lambda, \tag{2.19}$$

is the wavenumber and λ is the electromagnetic wavelength. For an oblique incidence as shown in Figure 2.2(b) the phase difference is

$$\Delta\phi = 2k\Delta h \cos\Theta = \frac{4\pi\Delta h}{\lambda}\cos\Theta \tag{2.20}$$

where Θ is the angle of incidence. For the definition shown in Figure 2.2, Θ is measured from the normal to the perfectly smooth surface indicated by the horizontal dashed line. Referring to Cartesian coordinates x, y and z, where the surface lies in the xy-plane, the normal to the surface will be the z-axis.
According to the Rayleigh roughness criterion the surface can be considered smooth, if the phase difference $\Delta\phi < \pi/2$. This constraint results in the following condition for a smooth surface:

$$\Delta h < \frac{\lambda}{8\cos\Theta}. \tag{2.21}$$

Regarding random surfaces, the height parameter Δh in the above inequality may be replaced by the RMS surface height h_0. From Eq. (2.21), it can be seen, that the Rayleigh roughness criterion is a simple combination of only three parameters: the height difference Δh, the electromagnetic wavelength λ and the angle of incidence Θ. Due to its simple formulation, this criterion is very popular in practice. This relation will be applied in combination with specular reflection later in this thesis (see Section 2.2.1).

Fraunhofer roughness criterion

Another method for classifying the roughness of surfaces, is the Fraunhofer roughness criterion. It is based on the definition of the far-field distance for an antenna ([7] page 827). According to this definition, a surface may be considered as electromagnetically smooth, for a phase difference between reflected rays of $\Delta\phi < \pi/8$. Therefore, the resulting relation between Δh, λ and Θ under the Fraunhofer roughness criterion differs from that of the Rayleigh roughness criterion:

$$\Delta h < \frac{\lambda}{32\cos\Theta}. \tag{2.22}$$

For random rough surfaces, the height parameter Δh can be replaced by the standard deviation of the surface height h_0.
Since we focus on the findings in [6], we use the Rayleigh criterion in the following.

2.2 Electromagnetic Wave Propagation over Sea

The EM wave propagation in a maritime environment is influenced by several mechanisms and effects. Besides the direct LOS path between transmitter (TX) and receiver (RX), multipath components occur due to reflection and scattering from the sea surface. Additional effects like diffraction, divergence and shadowing result from the curvature of the earth and the roughness of the sea. All these mechanisms will be discussed briefly in the subsections below.

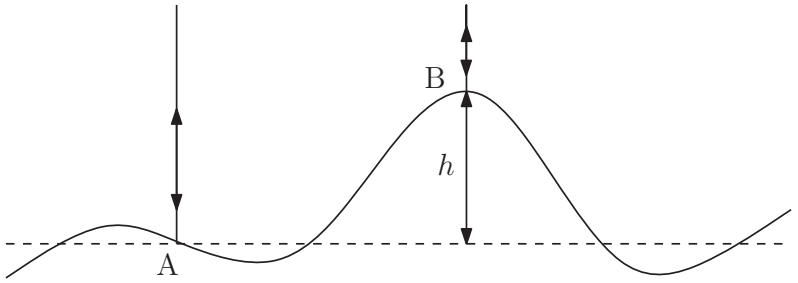

(a) Normal incidence

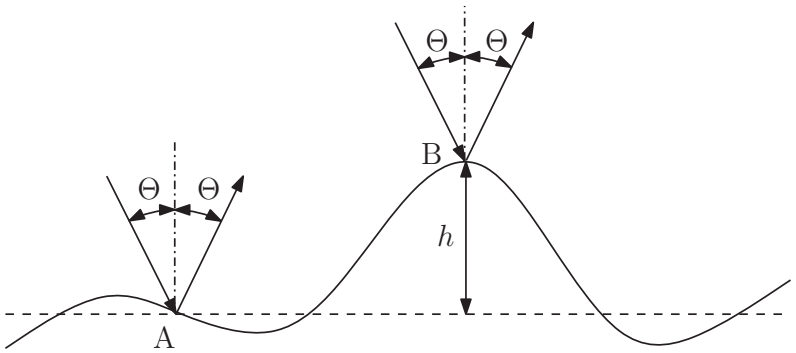

(b) Oblique incidence

Figure 2.2: Geometry for Rayleigh and Fraunhofer roughness criteria

2.2.1 Reflection

Reflection occurs, when an electromagnetic wave propagating in a medium 1 impinges onto another medium 2 with different electrical properties (e.g. permittivity ϵ, electromagnetic permeability μ and/or electrical conductivity σ). Reflection happens in combination with transmission of EM waves into medium 2. The energy of the reflected wave is always less than or equal to the energy of the incident wave. Furthermore, the amount of reflected energy also depends on the polarization of the EM wave (i.e. the orientation of the electric field vector with respect to the surface boundary between medium 1 and 2).
A typical geometry is illustrated in Figure 2.3. The quantities associated with the incident wave are denoted by subscript i, those associated with the reflected and transmitted waves by subscript r and t, respectively. The angles, marked by Θ, are measured from the normal to the boundary layer between medium 1 and 2 (i.e., the z-axis), where $\Theta_i = \Theta_r$ according to Snell's law of reflection [5] (page 55). Therefore, the impinging wave is reflected specularly. For our case, Medium 1 is considered as air and Medium 2 as sea water in the following.
The wavevectors of incident, reflected and transmitted waves are generally defined as

$$\vec{k} = \frac{2\pi}{\lambda}\frac{\vec{k}}{|\vec{k}|}, \tag{2.23}$$

where

$$k = |\vec{k}| = \frac{2\pi}{\lambda} \tag{2.24}$$

is denoted as the wavenumber.
In order to quantify the reflected electric field in terms of the incident one, the well known Fresnel reflection coefficients for vertical and horizontal polarizations of the incident electric field are applied. According to Figure 2.3 vertical polarization corresponds to an electric field vector in the vertical xz-plane. Whereas a horizontal polarized EM wave contains an E-field vector in the horizontal xy-plane. The Fresnel reflection coefficients for vertical and horizontal polarizations are defined as

$$\Gamma_v = \frac{\eta_1 \cos(\Theta_i) - \eta_2 \cos(\Theta_t)}{\eta_1 \cos(\Theta_i) + \eta_2 \cos(\Theta_t)}, \tag{2.25}$$

and

$$\Gamma_h = \frac{\eta_2 \cos(\Theta_i) - \eta_1 \cos(\Theta_t)}{\eta_2 \cos(\Theta_i) + \eta_1 \cos(\Theta_t)}, \tag{2.26}$$

where η_1 and η_2 are the intrinsic impedances of medium 1 and 2, given by $\sqrt{\mu_1/\epsilon_1}$ and $\sqrt{\mu_2/\epsilon_2}$, respectively.

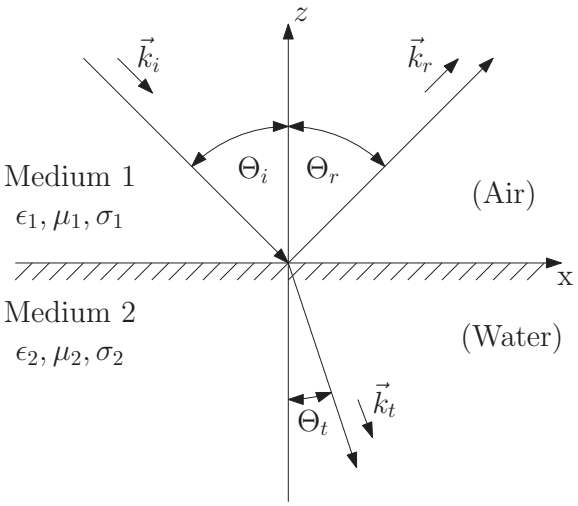

Figure 2.3: Reflection and transmission of an EM wave

2.2.2 Scattering

Scattering is a propagation mechanism related to reflection. Whether reflection or scattering occurs, is determined by the ratio of the wavelength λ of the incident wave and the dimensions of the reflecting object ([8], page 113 et seq.). Since this thesis is focused on reflection and scattering from the sea, the dimensions of the reflecting object will be represented by the degree of surface roughness. Therefore, reflection occurs when λ is small, and scattering takes place when λ is large compared to the surface roughness. In contrast to specular reflection, the outgoing energy of the incident wave is not focused into one specific direction (e.g. $\Theta_i = \Theta_r$), but is scattered diffusely into all directions. The transition from specular reflection to diffuse scattering dependent on the surface roughness is illustrated in Figure 2.4. For a perfectly smooth surface the incident wave is specularly reflected and there is no

diffusely scattered component. In this case the outgoing electric field is quantified by the Fresnel reflection coefficient as mentioned above. With increasing degree of surface roughness the specularly reflected power decreases and the scattered part increases, until the entire incident wave is scattered diffusely, in case of a very rough surface (see Figure 2.4(b) and (c)). To account for the decrease in power of the specularly reflected part the scattering loss factor ρ_s is introduced ([8] page 135 et seq.), which is based on the Rayleigh roughness criterion. Related publications ([6]) denote this factor as specular scattering coefficient and is given by

$$\rho_s = \exp\left(-\frac{u^2}{2}\right), \tag{2.27}$$

where the roughness parameter u is defined as

$$u = kh_0(\cos\Theta_i + \cos\Theta_r) = \frac{2\pi}{\lambda}h_0(\cos\Theta_i + \cos\Theta_r). \tag{2.28}$$

Therefore, the modified reflection coefficient for a rough surface is defined as

$$\Gamma_{rough} = \Gamma\rho_s = \Gamma\exp\left[-\frac{1}{2}u^2\right] = \Gamma\exp\left[-\frac{1}{2}\left(\frac{2\pi h_0(\cos\Theta_i + \cos\Theta_r)}{\lambda}\right)^2\right]. \tag{2.29}$$

with the Fresnel reflection coefficient Γ given in Eqs. (2.25) and (2.26) for vertival and horizontal polarization, respectively.
The propagation mechanism of diffuse scattering from the sea surface will be discussed again in more detail in Section 2.3.3.

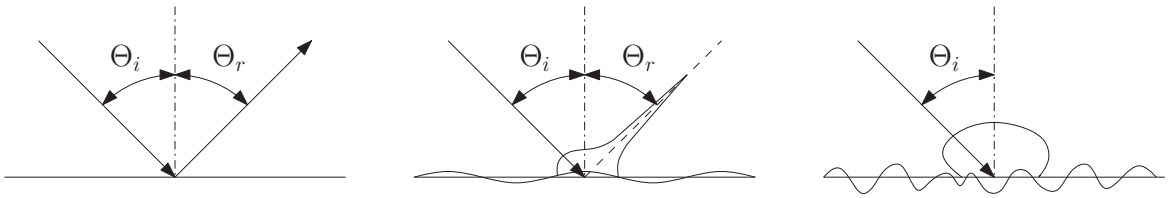

(a) perfectly smooth surface (b) slightly rough surface (c) very rough surface

Figure 2.4: Scattering from surfaces with various degrees of roughness

2.2.3 Diffraction

From a geometrical point of view the radio transmission over sea between transmitter and receiver will be blocked at a certain point, due to the curvature of the earth. However, diffraction enables electromagnetic waves to propagate, even if the LOS path is blocked. This phenomenon can be explained by the Huygen-Fresnel principle ([8], page 126). According to this, all points of an EM wavefront may be described as individual point sources, which produce secondary wavelets. The resulting wavefront in the direction of propagation can then be computed as the vector sum of the electric and/or magnetic field vectors of all secondary wavelets. Therefore, EM waves are able to propagate even into obstructed regions. The field strength, however, decreases rapidly with increasing angle ψ. Considering a curved earth, this

corresponds to an increasing distance between TX and RX and diffraction may be considered as an additional propagation loss.
The wave propagation over a curved Earth beyond LOS is depicted in Figure 2.5, where the radius of a spherical earth is illustrated as r_e and the path of the EM wave is shown as dashed line. The arc lengths from TX and RX to the horizon are given as

$$d_1 = \sqrt{2k_e r_e h_{TX}}, \tag{2.30}$$

and

$$d_2 = \sqrt{2k_e r_e h_{RX}}, \tag{2.31}$$

where h_{TX} and h_{RX} denote the heights of the transmitter and receiver above a spherical earth ([3]). The factor k_e is the ratio between true and effective earth's radius. The complete horizontal distance d between TX and RX therefore consists of the arc lengths d_1, d_2 and d_3:

$$d = d_1 + d_2 + d_3, \tag{2.32}$$

where d_3 is the arc length beyond the horizons of TX and RX. Another representation for d is

$$d = r_e \delta, \tag{2.33}$$

with the angle δ between TX and RX measured at the center of the spherical earth.
The diffraction mechanism is considered in the REL model and will be further examined in Section 2.3.2.

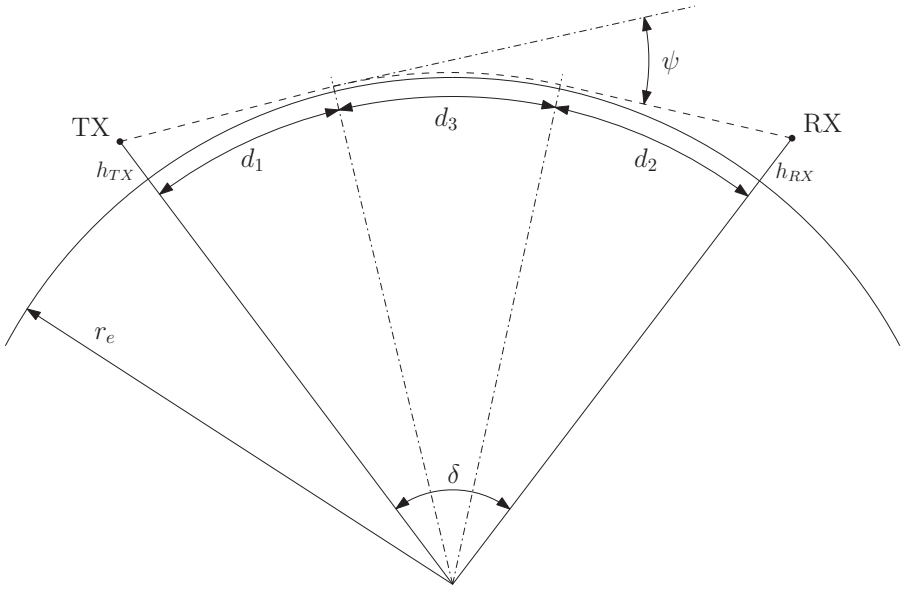

Figure 2.5: Diffraction by the curvature of the Earth

2.2.4 Divergence

The divergence phenomenon describes an additional decrease of the power density of an EM wave caused by the reflection from a curved earth. Figure 2.6 represents a simple geometry of

radio transmission effected by divergence, where D_1 and D_2 are the horizontal distances over ground measured from the geometrical point of reflection to the TX and RX, respectively. Let r_1 be the distance between TX and reflection point, r_2 the distance between RX and reflection point and γ the elevation angle of the incident (and reflected) ray. Again, h_{TX} and h_{RX} are the heights of TX and RX above a spherical earth.
Due to the curvature of the earth the incident angle of the wave front is not the same for all points on the curved surface. Therefore, the impinging EM wave diverges after reflection, indicated by the dashed lines in Figure 2.6. In order to appropriately account for this effect, the Fresnel reflection coefficient is multiplied by the divergence coefficient, which is defined in ([6] page 222 et seq.) as

$$D = \frac{1}{\sqrt{\left(1 + \frac{2r_1r_2}{a(r_1+r_2)\sin\gamma}\right)\left(1 + \frac{2r_1r_2}{b(r_1+r_2)}\right)}}, \tag{2.34}$$

where a and b are the semi-major and semi-minor axis, respectively, of the ellipsoidal earth. For small angles of incidence γ and the spherical earth with radius r_e this equation may be simplified to

$$D \approx \frac{1}{\sqrt{1 + \frac{2r_1r_2}{r_e(r_1+r_2)\sin\gamma}}}. \tag{2.35}$$

The resulted reflection coefficient considering the divergence effect may then be written as

$$\Gamma_{Div} = D\Gamma, \tag{2.36}$$

where Γ denotes the Fresnel reflection coefficient for a specified polarization, given in (2.25) and (2.26), respectively.

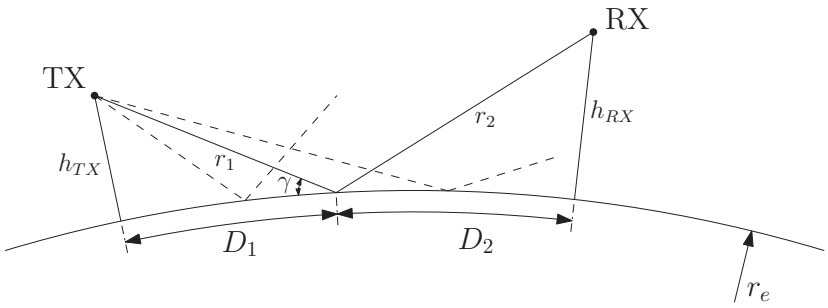

Figure 2.6: Divergence effect

2.2.5 Shadowing

In contrast to the diffraction and the divergence, which occur due to the curved shape of the earth, shadowing is caused by the roughness of the surface, as illustrated in Figure 2.7. The incident EM wave is reflected from a rough surface. The mean surface is indicated by the dashed line and the angle of incidence Θ is measured from the normal of the mean surface. Due to the undulations some regions of the surface are not illuminated (shaded area) and,

therefore, no reflection occurs for these shadowed areas. Similar to the divergence effect, shadowing is taken into account by multiplying the Fresnel reflection coefficient (for a smooth surface) with a shadowing factor S. In literature this coefficient has different definitions. Throughout this thesis two definitions according to [9] and [10] will be used.
The shadowing factor derived by [10] is defined as

$$S = \frac{1 - 0.5\mathrm{erfc}(\frac{\cot\Theta_i}{\sqrt{2}\beta_0})}{\Lambda(\Theta_i, \beta_0), +1} \tag{2.37}$$

where β_0 is the RMS surface slope, erfc is the complementary error function and Λ is given by

$$\Lambda(\Theta_i, \beta_0) = \frac{1}{2}\left[\sqrt{\frac{2}{\pi}}\frac{\beta_0}{\cot\Theta_i}\exp\left(-\frac{\cot^2\Theta_i}{2\beta_0^2}\right) - \mathrm{erfc}\left(\frac{\cot\Theta_i}{\sqrt{2}\beta_0}\right)\right]. \tag{2.38}$$

In the context of bistatic scattering, another shadowing factor is defined in [9] as

$$S = \frac{1}{1 + \Lambda(\Theta_i, \beta_0) + \Lambda(\Theta_r, \beta_0)}. \tag{2.39}$$

Independent of the definition, S is ranging between 0 and 1 and reduces the Fresnel reflection coefficient Γ. Hence, the effective reflection coefficient considering shadowing is given by

$$\Gamma_S = S\Gamma. \tag{2.40}$$

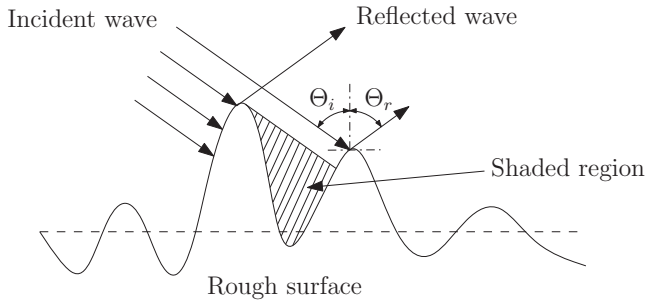

Figure 2.7: Shadowing effect caused by rough surfaces

2.3 State-of-the-art maritime channel models

2.3.1 Recommendation ITU-R P.1546-2

As reported in [2] the Recommendation ITU-R P.1546-2 is a method for predictions of point-to-area propagation for terrestrial services in the frequency range from 30 MHz to 3000 MHz. The ITU-R model is based on propagation curves, which represent E-field strength values in dB(μV/m) as a function of the distance d in km (from 1 km to 1000 km). The curves in the provided document ([2]) are given for the following parameters:

- transmit power of 1 kW effective radiated power (ERP),

- nominal frequencies f of 100 MHz, 600 MHz and 2000 MHz,
- receiver height h_2 of 10 m,
- transmitter heights h_1 of 10, 20, 37.5, 75, 150, 300, 600 and 1200 m,
- percentage times t of 50%, 10% and 1%.

The percentage times mean, that the corresponding field strength values of the propagation curves are exceeded for 50%, 10% or 1% of time. The method is not valid for percentage times <1% or >50%. Furthermore, the curves are different for propagation over land, cold sea (e.g., the North Sea) and warm sea (e.g., the Mediterranean Sea). Independent from the parameters listed above, all provided propagation curves show the field strength values exceeded for 50% of locations (within an area of 500 m times 500 m).
Since the required parameters (f, h_1, h_2 and t) may not coincide with the provided values, the prediction method is basically a step-by-step interpolation and/or extrapolation procedure to obtain the field strength value. The entire procedure consists of 17 steps and is described in the Recommendation ITU-R P.1546-2, which will be referred to as *ITU model* in the following chapters. The prediction procedure is examined in detail in Section 4.2.1, where the required parameters are applied to the model and the results are discussed.

2.3.2 Round Earth Loss model for open-sea radio propagation

The REL model proposed in [3] is a path loss model for maritime environments in the open-sea region (i.e., no influence by coastal areas and harbors). It is based on the two-ray method over a spherical earth, where only the direct LOS path and the specular reflected path are considered. Further propagation phenomena taken into account are shadowing, divergence and diffraction. The basic geometry used for the REL model is illustrated in Figure 2.8. All quantities shown in the figure can also be found in [3] and will be explained in the following.
The LOS distance D_{LOS} between the transmitter and the receiver, as well as the distances X_1 and X_2 from the specular reflection point to the transmitter and to the receiver, respectively, are derived from geometry as

$$D_{LOS} = \sqrt{(r_e + h_1)^2 + (r_e + h_2)^2 - 2(r_e + h_1)(r_e + h_2)\cos(\frac{d}{r_e})}, \tag{2.41}$$

$$X_1 = \sqrt{(r_e + h_1)^2 + r_e^2 - 2(r_e + h_1)r_e\cos\alpha}, \tag{2.42}$$

and

$$X_2 = \sqrt{(r_e + h_2)^2 + r_e^2 - 2(r_e + h_2)r_e\cos\beta}. \tag{2.43}$$

h_1 is the transmitter height above the spherical earth and h_2 the receiver height. The quantity r_e is the earth radius and the angles α and β are given by the transcendental equation

$$\arccos\left(\frac{r_e + h_1 - r_e\cos\alpha}{X_1}\right) + \alpha = \arccos\left(\frac{r_e + h_2 - r_e\cos\beta}{X_2}\right) + \beta, \tag{2.44}$$

with

$$\alpha + \beta = \frac{d}{r_e}, \tag{2.45}$$

and d is the arc length between TX and RX written as

$$d = D_1 + D_2 = \alpha r_e + \beta r_e. \tag{2.46}$$

The path difference D_{Diff} between direct and reflected path is given by

$$D_{Diff} = X_1 + X_2 - D_{LOS}. \tag{2.47}$$

The dashed heights h_1' and h_2' are measured from the tangential plane of the reflection point to the positions of TX and RX, respectively, and are calculated by

$$h_1' = h_1 - 0.5 r_e \alpha^2, \tag{2.48}$$

and

$$h_2' = h_2 - 0.5 r_e \beta^2. \tag{2.49}$$

The incidence and reflection angles may be written as

$$\Theta_i = \frac{\pi}{2} - \arcsin\left(\frac{h_1'}{X_1}\right) = \frac{\pi}{2} - \arcsin\left(\frac{h_2'}{X_2}\right) = \Theta_r. \tag{2.50}$$

The REL model proposes a calculation of the path loss L_P for open sea environments as

$$L_P = 20 \log_{10}\left(\frac{\lambda}{4\pi D_{LOS}} \left|1 + SD\Gamma_{rough} \exp(jkD_{Diff})\right|\right) + L, \tag{2.51}$$

where the shadowing factor S is given by Eq. (2.37), the divergence coefficient D by (2.34) and (2.35), the reflection coefficient for a rough surface Γ_{rough} by (2.29) and the diffraction loss L is defined in Appendix A. In this definition the path loss L_P represents a negative quantity.

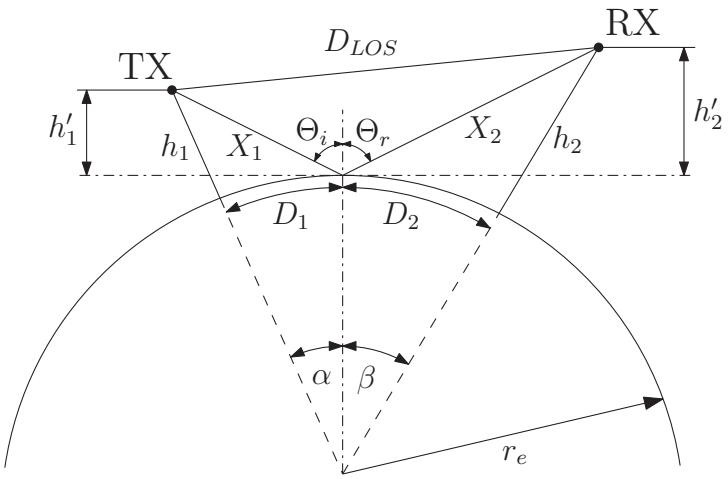

Figure 2.8: Geometric representation of the REL model

2.3.3 Karasawa's model

In contrast to the previously discussed models in Sections 2.3.1 and 2.3.2, Karasawa's model ([4]) considers three components: the direct LOS component, the specularly reflected component and in addition the diffusely scattered component from the sea surface. In the following the specular and diffuse components are also denoted as *coherent* and *incoherent* component, respectively.
According to Karasawa, interferences between LOS and reflected waves cause multipath fading, where the reflections from the sea surface are composed of the specular reflection (i.e., the coherent component) and the diffuse scattering (i.e., incoherent component).
The specular reflection can be geometrically treated to happen at a specific reflection point. It is computed, using the Fresnel reflection coefficient defined in Eq. (2.29). Since the diffuse scattering occurs over a larger area of the sea surface, than the specular reflection, a 3-dimensional coordinate system has to be considered. To compute the scattering from a certain point on the sea surface, Karasawa defined a local Cartesian coordinate system as depicted in Figure 2.9, where the origin is located at the scattering point. The $x'y'$-plane corresponds with the mean sea surface and the negative x'-axis is directed to the TX position. The incidence and scattering angles Θ_i and Θ_s, respectively, are measured from the z'-axis. The azimuth angle Φ_s is measured in the $x'y'$-plane, starting from the x'-axis. The wavevectors $\vec{k}_i$ and $\vec{k}_s$ indicate the TX and RX directions, respectively.

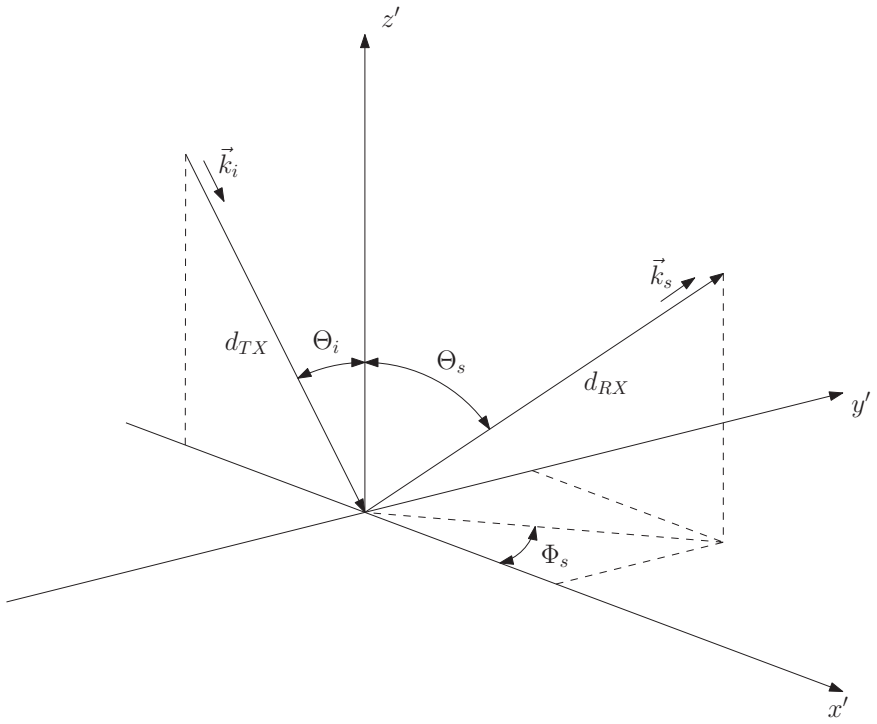

Figure 2.9: Coordinate system for Karasawa's model

To obtain the diffusely scattered power and the corresponding electric field strength, Karasawa integrated over the sea surface. Furthermore, he considered the coherent and the incoherent

components relative to the incident field strength.
Using the normalized coherent and incoherent components, Karasawa investigated L-Band multipath fading characteristics caused by the sea surface.

2.4 Physical Optics Model

A new maritime channel model for path loss predictions is proposed in this section, based on Karasawa's findings ([4]). This model is denoted as PO model and takes the LOS component, the coherent component and the incoherent component into account. In contrast to Karasawa's model, which focuses on the characteristics of multipath fading, the PO model is suitable, to predict the received power in a maritime environment. In the following, the PO model is described in detail. We start with the calculation of the diffuse scattering, where we refer to the local Cartesian coordinate system, shown in Figure 2.9.
To compute the received power of the incoherent component $P_{r,inc}$, the bistatic radar equation is used, which is defined as

$$P_{r,inc} = \frac{P_t G_t}{4\pi d_{TX}^2} \sigma \frac{1}{4\pi d_{RX}^2} G_r \frac{\lambda^2}{4\pi} = \frac{P_t G_t}{4\pi d_{TX}^2} \sigma_0 A \frac{1}{4\pi d_{RX}^2} G_r \frac{\lambda^2}{4\pi} \tag{2.52}$$

where P_t is the transmit power, G_t and G_r are the gains of transmitting and receiving antenna, respectively, d_{TX} and d_{RX} are the distances from the scattering point to the transmitter and the receiver, respectively, λ is the electromagnetic wavelength, A is the considered scattering area, σ denotes the radar cross section (RCS) and the scattering coefficient σ_0 is given by

$$\sigma_0(\Theta_i, \Theta_s, \Phi_s) = \begin{cases} \frac{u^4}{2\beta_0^2} \sec^4 \exp\left(-u^2 \left[1 + \frac{\tan^2\gamma}{m2\beta_0^2}\right]\right) |S\Gamma_{rough}|^2, & u^2 \ll 1 \text{ (smooth sea)}, \\ \frac{1}{2\beta_0^2} \sec^4 \exp\left(-\frac{\tan^2\gamma}{m2\beta_0^2}\right) |S\Gamma_{rough}|^2, & u^2 \gg 1 \text{ (rough sea)}, \end{cases} \tag{2.53}$$

where the angle γ is defined in [6] (page 89) and [4] as

$$\gamma = \arctan\left\{ \frac{\sqrt{\sin^2\Theta_i - 2\sin\Theta_i \sin\Theta_s \cos\Phi_s + \sin^2\Theta_s}}{\cos\Theta_i + \cos\Theta_s} \right\}. \tag{2.54}$$

The shadowing factor S according to (2.39), as well as the modified Fresnel reflection coefficient Γ_{rough} given in (2.29) are already included. The quantities σ and σ_0 are described in detail in Appendix B.
In order to simplify the geometry and to decrease the computational complexity of the diffuse scattering component, a plane earth is assumed in the PO model. It is worth to note, that without the incoherent component, the PO model is similar to the REL model. In this case the only difference between these two models would be the distinct consideration of the plane or the curved earth.
Figure 2.10 illustrates the geometry for the PO model. The mean sea surface lies in the xy-plane and is divided into tiles with dimensions $A_{tile} = d_f^2$, as indicated by the red grid. TX and RX are located at $(0, 0, h_{TX})^T$ and $(d, 0, h_{RX})^T$, respectively, where h_{TX} and h_{RX} are the antenna heights above mean sea level (MSL) and d is the horizontal distance between TX and RX. The dashed lines represent three different components, where black denotes

the LOS component, purple the coherent component and blue the incoherent component. Since the scattering coefficient $\sigma_0(\Theta_i, \Theta_s, \Phi_s)$ is angle-dependent, it is different for each tile on the grid. Therefore, the total incoherent power at the receiver is the sum of the scattering contributions from all tiles, which can be written as

$$P_{r,inc} = \frac{P_t A_{tile} \lambda^2}{(4\pi)^3} \sum_{n=1}^{N} \frac{G_{t,inc,n} G_{r,inc,n} \sigma_{0,n}}{d_{TX,n}^2 d_{RX,n}^2}, \tag{2.55}$$

where N is the number of tiles and the subscript n denotes the different tiles. $G_{t,inc}$ and $G_{r,inc}$ are the gains of transmitting and receiving antenna in the direction of the different tiles.
The received power of the LOS and coherent component are calculated by

$$P_{r,LOS} = \frac{P_t G_{t,LOS}}{4\pi d_{LOS}^2} G_{r,LOS} \frac{\lambda^2}{4\pi}, \tag{2.56}$$

and

$$P_{r,coh} = \frac{P_t G_{t,coh}}{4\pi (d_{TX,coh} + d_{RX,coh})^2} \left| S\Gamma_{rough} \right|^2 G_{r,coh} \frac{\lambda^2}{4\pi}, \tag{2.57}$$

where S is the shadowing factor according to Eq. (2.39), Γ_{rough} is the Fresnel reflection coefficient for a rough surface and specified polarization defined in (2.29) and d_{LOS} is the direct LOS distance between TX and RX. Especially for the coherent component, $d_{TX,coh}$ and $d_{RX,coh}$ are the distances from the specular reflection point to TX and RX, respectively. $G_{t,LOS}$ and $G_{r,LOS}$ are the transmitting and receiving antenna gains in the direction of RX and TX, respectively. $G_{t,coh}$ and $G_{r,coh}$ are the transmitting and receiving antenna gains in the direction of the specular reflection point.
Due to the fact, that Eqs. (2.55) to (2.57) denote powers, no phase informations are available. Therefore, we will pass to the electric field representation for each component. This enables us to coherently add up the field components to get a resulted field at the receiver.
In general the received power P_r is the product of the power density P_d and the effective antenna area A_e

$$P_r = P_d A_e, \tag{2.58}$$

where

$$A_e = \frac{G_r \lambda^2}{4\pi}, \tag{2.59}$$

and

$$P_d = \frac{P_t G_t}{4\pi d^2} = \frac{|E|^2}{\eta} = \frac{|E|^2}{120\pi}, \tag{2.60}$$

with the intrinsic impedance of free space $\eta = 120\pi\ \Omega$. From (2.60) we can compute the magnitude of the electric field and its phase is determined by the traveled distance from the transmitter to the receiver. Therefore, we obtain the following expressions for the electric fields of the direct LOS, the coherent and the incoherent components at the receiver

$$E_{LOS} = |E_{LOS}| \exp(-j\phi_{LOS}) = \sqrt{30 P_t G_{t,LOS} G_{r,LOS}} \frac{1}{d_{LOS}} \exp\left(-j \frac{2\pi}{\lambda} d_{LOS}\right), \tag{2.61}$$

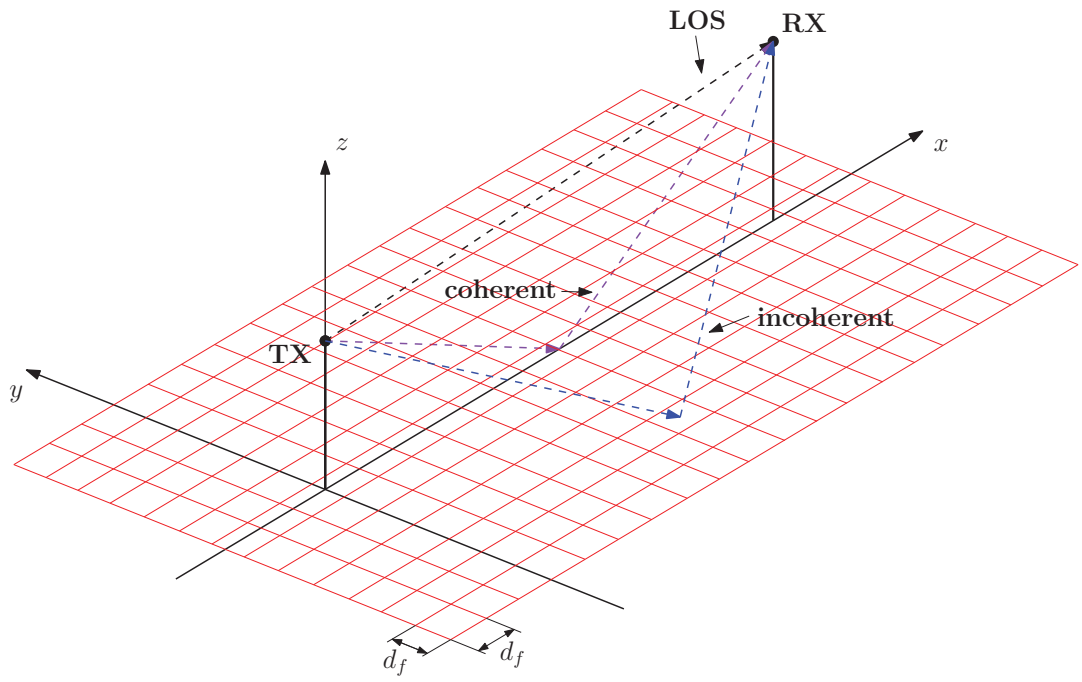

Figure 2.10: Geometry of the PO model

$$\begin{aligned} E_{coh} &= |E_{coh}| \exp(-j\phi_{coh}) \\ &= \sqrt{30 P_t G_{t,coh} G_{r,coh}} \frac{S\Gamma_{rough}}{d_{TX,coh} + d_{RX,coh}} \exp\left(-j\frac{2\pi}{\lambda}(d_{TX,coh} + d_{RX,coh})\right), \end{aligned} \tag{2.62}$$

and

$$\begin{aligned} E_{inc} &= |E_{inc}| \exp(-j\phi_{inc}) \\ &= \sqrt{\frac{30 P_t A_{tile}}{4\pi}} \sum_{n=1}^{N} \frac{\sqrt{G_{t,inc,n} G_{r,inc,n} \sigma_{0,n}}}{d_{TX,n} d_{RX,n}} \exp\left(-j\frac{2\pi}{\lambda}(d_{TX,n} + d_{RX,n})\right) \exp\left(-j\phi_R\right), \end{aligned} \tag{2.63}$$

where a random phase shift ϕ_R is added to the incoherent component, to account for the random sea surface, as assumed in [6]. The phase shift is uniformly distributed over $[0, 2\pi)$. The total received electric field E is then obtained by

$$E = E_{LOS} + E_{coh} + E_{inc}, \tag{2.64}$$

and the total received power P_r is given as

$$P_r = \frac{|E|^2}{\eta}\frac{\lambda^2}{4\pi} = \frac{|E|^2}{120\pi}\frac{\lambda^2}{4\pi} = \frac{|E|^2\lambda^2}{480\pi^2}. \tag{2.65}$$

3 Channel measurement campaign

In order to develop new communication and navigation systems for the maritime environment, the characteristics of the radio propagation channel over sea must be known. One way to gather information about the wireless channel characteristics are measurement campaigns. For this reason the Mobile Radio Transmission Group at the Institute of Communications and Navigation of the German Aerospace Center (DLR) performed a broadband channel measurement campaign in the Baltic Sea in March 2014 as reported in [1]. The difference to former maritime channel measurement campaigns, which were focusing on narrow bandwidths of maximum 20 MHz (cf. [1]), is the broadband approach with a bandwidth of 100 MHz at a center frequency of 5.2 GHz. This enables the measurement of the CIR with a high delay-resolution of 10 ns (which corresponds to a path difference of about 3 m) and therefore a more precise investigation of distinct multipath components (MPCs).
The complete measurement campaign has taken place from 17 to 21 March 2014 in the harbor and near the coast of Warnemünde, Germany. In this thesis we focus on the measurements of 18 and 19 March 2014 (Tuesday and Wednesday), where the transmitter was on a ship and the receiver was located on two different land sites. The ship *Rosenort*, visualized in Figure 3.1, was provided by the German Federal Waterways and Shipping Administration (WSV). The mast with the mounted transmit and GPS antennas is shown in Figure 3.2. The receiver sites were at the lighthouse of Warnemünde and the Hotel *Neptun*. The latter building is the highest building along the coast. The positions of transmitter and receiver during the campaign were measured by GPS receivers. In Figure 3.3 both receiver sites are shown, as well as the approximate ship position in the harbor of Warnemünde for the calibration reference measurements. These reference measurements were necessary to calibrate the two Rubidium clocks of the transmitter and the receiver before measurements on each day. During the reference measurements a clear LOS-path between transmitter and receiver was present.

Figure 3.1: Ship *Rosenort* provided by WSV, where the transmit antenna was mounted on

Figure 3.2: Ship mast with transmit and GPS antennas

Figure 3.3: Receiver sites and ship position for LOS reference measurements

3.1 Channel measurement equipment

For the measurements a *MEDAV RUSK-DLR* channel sounder was used, which is described in detail in [11](page 29 et seq.). The channel sounder operated at a center frequency of 5.2 GHz (i.e. C-band) with a bandwidth of 100 MHz. The transmitter output was a periodic spread spectrum multitone signal with a transmit power of 43 dBm and a period of 12.8 µs. The complete bandwidth was separated into 1281 sub-carriers, with equal gain and an inter-carrier space of 78.125 kHz. The CIR snapshots were saved every 40 ms, which results in approximately 25 snapshots per second. Corresponding to the used bandwidth of $B = 100$ MHz, the CIR was recorded with a delay-resolution of $\Delta\tau = \frac{1}{B} = 10$ ns. Assuming the speed of light of approximately $c \approx 3 \times 10^8$ $^{\mathrm{m}}/_{\mathrm{s}}$, this delay-resolution results in a resolvable path difference between distinct MPCs of $\Delta s = c \times \Delta\tau \approx 3 \times 10^{8\,\mathrm{m}}/_{\mathrm{s}} \times 10$ ns $= 3$ m.
During the campaign, Single-Input-Single-Output (SISO), as well as Single-Input-Multiple-Output (SIMO) measurements were performed. We will concentrate on the SIMO measurements throughout this thesis, where an omni-directional antenna was used on transmitter side and a circular patched antenna array on receiver side. The antenna array consists of 32 elements, which are arranged concentrically in two equal rings placed one above the other as shown in Figure 3.4. Each antenna element is dual-polarized, such that both vertically and horizontally polarized waves ca be measured. However, we will focus on the results for vertical polarization. The antenna array measurement data enabled the usage of only those elements, which directed towards the ship. Therefore, unwanted reflections from the receiver sites or the harbor were suppressed.

Figure 3.4: Antenna array for SIMO measurements

Figure 3.5 indicates the calibrated pattern of a single antenna element for the entire azimuth range (from -180° to +175° in 5°-step) and three different elevation angles, measured from the cylinder axis showing upwards (see Figure 3.4).

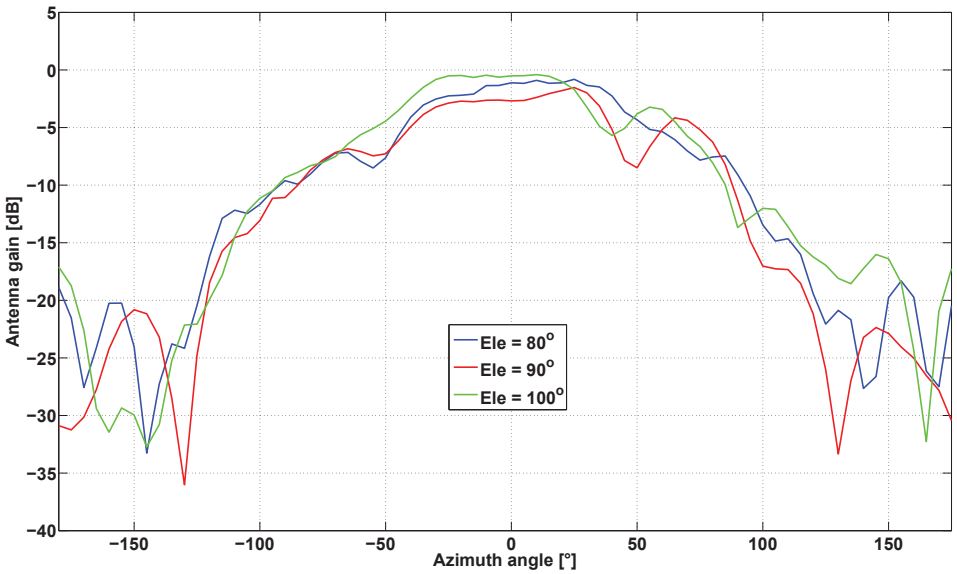

Figure 3.5: Calibrated pattern of a single antenna array element

The settings of the channel sounder equipment are summarized in Table 3.1 as in [1].

Parameter	**Value**
Center frequency	5.2 GHz
Bandwidth	100 MHz
Number of sub-carriers	1281
Sub-carrier spacing	78.125 kHz
Transmit power	43 dBm
Signal period	12.8 μs
Time between CIR snapshots	$\sim$40 ms
Transmit antenna	vertically polarized omni-directional
Receive antenna	dual-polarized cirular antenna array (only vertical polarization used)

Table 3.1: Overview of the channel sounder settings

3.2 Channel measurement scenarios

For each land site, measurements were conducted on two different floors. This means we distinguish among four receiver heights or scenarios, which are listed chronologically below:

1. Tuesday, March 18 - receiver on lighthouse/2nd (*upper*) floor - 32.9 m above MSL
2. Tuesday, March 18 - receiver on lighthouse/1st (*lower*) floor - 21.6 m above MSL
3. Wednesday, March 19 - receiver on hotel/15th (*upper*) floor - 48.0 m above MSL
4. Wednesday, March 19 - receiver on hotel/9th (*lower*) floor - 32.3 m above MSL

The corresponding ship tracks during the four scenarios are illustrated in Figure 3.6, where the ship, used for the measurements, was moving away from the harbor on the green track (outgoing ship) and was approaching the harbor (incoming ship) on the other three tracks (i.e. red, black and violet) at an average speed of ~ 4 $^{m}/_{s}$.
Due to technical reasons, the measurement on the lighthouse/lower floor has not been performed. Therefore, this scenario is omitted in this thesis.

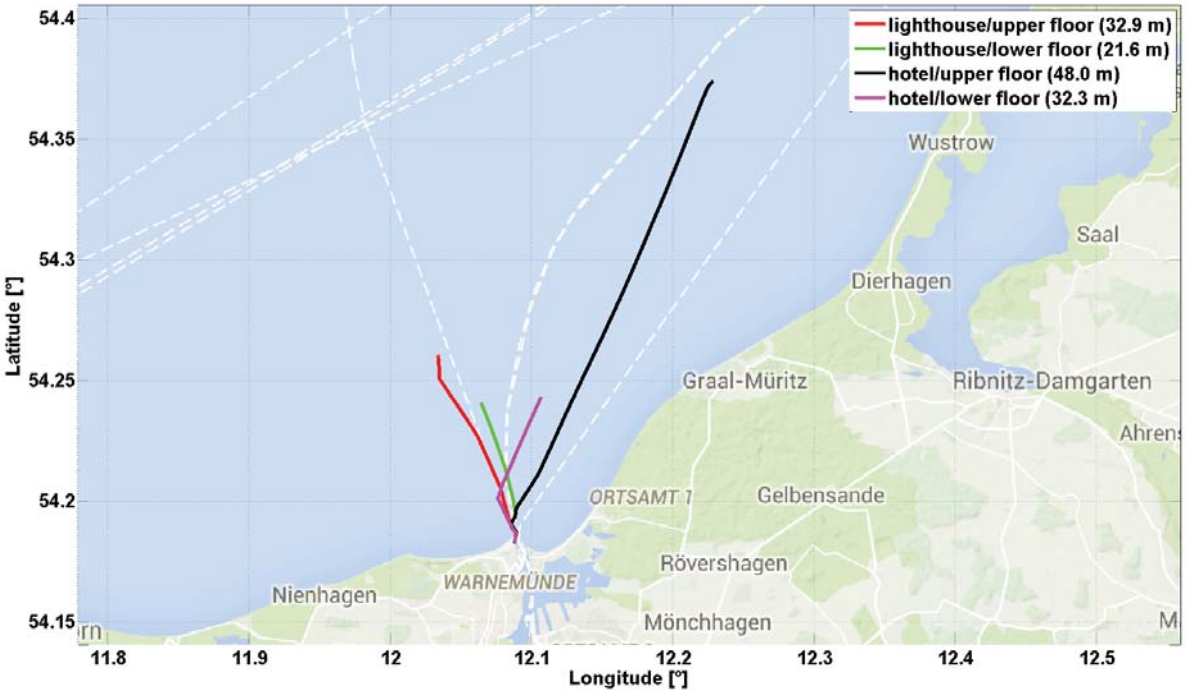

Figure 3.6: Ship tracks for SIMO measurements

3.3 GPS measurements of transmitter and receiver positions

For the determination of TX and RX positions during the channel measurements, Septentrio GPS receivers were used on both sides. On the transmitter side, the raw data of the GPS measurements were saved in the format of receiver independent exchange format (RINEX), including pseudo-range measurements and clock informations. A dual-frequency GPS measurement has been applied to achieve the precise point positions (PPP). On the receiver side the antenna position was fixed and, therefore, an average over the measured position for hours was performed, to increase the accuracy. The measured GPS information was used as an input to the receiver of the channel sounder, where each measured CIR was triggered by a time-synchronized GPS measurement. In every record information about latitude, longitude, GPS height H above the reference ellipsoid defined in the World Geodetic System (WGS84) and corresponding UTC time were saved. The GPS height H is also denoted as ellipsoidal height.
For the PO model, introduced in Section 2.3.3, the height h above MSL (i.e. orthometric height) is required for TX and RX. The MSL is represented by the geoid defined in the Earth Gravitational Model 1996 (EGM96), which is an approximation in terms of spherical harmonics. Figure 3.7 illustrates the relationship between the reference ellipsoid defined in the WGS84, the geoid given by the EGM96 and the topography of land and sea. The quantity N_{G} denotes the geoid height (height of the mean sea level) above the WGS84 reference ellipsoid. The relation between them can be expressed as

$$H = h + N_{\mathrm{G}}. \tag{3.1}$$

Since latitude and longitude are included in each GPS position measurement the corresponding geoid height N_{G} was derived from the EGM96. Therefore we were able to calculate the orthometric height h for every position record.

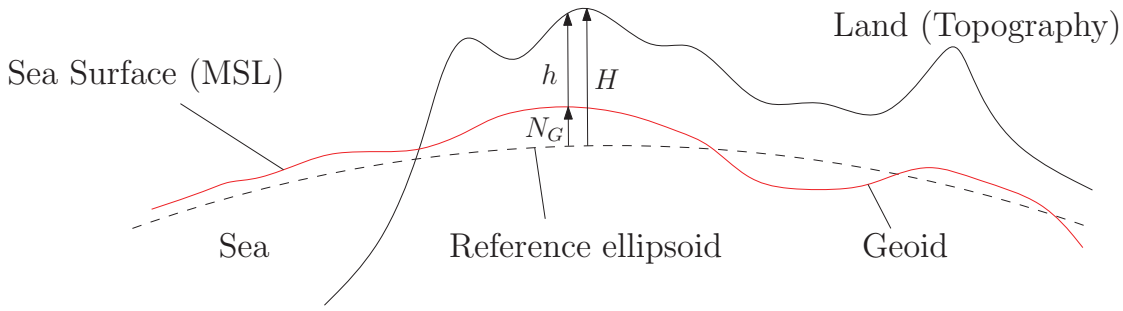

Figure 3.7: Relation among ellipsoidal height H, orthometric height h and geoid height N_{G}

4 Path loss model evaluation

In this chapter we first discuss the SIMO measurement results in terms of received power as a function of distance between transmitter and receiver. The subsequent section focuses on the simulation results of ITU model (Section 2.3.1), REL model (Section 2.3.2) and PO model (Section2.3.3). It is worth noting that in this chapter only the path loss model results corresponding to the SIMO measurements of Tuesday/lighthouse/upper floor (32.9 m above MSL) are discussed in detail. The path loss simulation results for the remaining three scenarios can be found in Appendix C.

4.1 Measurement results

Figures 4.1 to 4.3 show the received power P_r as a function of TX-RX-distance for the SIMO measurements. According to [8] (page 106), the mean received power, averaged over a traveled measurement distance of 5λ to 40λ, is relevant for path loss models. Therefore, the following results for the received power were averaged over $\sim$1 m. Additionally, each figure contains a plot, depicting the changing transmit antenna height h_TX on the ship above MSL level. In order to make the figures easier to compare, the scalings of the distance (x-axis) and received power (y-axis, upper plot) are equal for all plots.
In Figure 4.1 the SIMO results for Tuesday/lighthouse/upper floor (32.9 m above MSL) are illustrated. Measurements were recorded for distances from 220 m to 9 km. The received power decreases continuously with increasing distance, due to the Free Space Loss (FSL). For TX-RX-distances greater than $\sim$ 1 km, a typical fading behavior for two-ray propagation can be observed, where alternating constructive and destructive interferences between direct LOS-path and the specular reflected path appear. The destructive superimpositions result in deep fades. At shorter distances, this interfering behavior is no longer recognizable and the received power is primarily dominated by random fluctuations superimposed on the LOS signal. This indicates, that the specular reflected signal decreases with decreasing distance. The fluctuations are mainly caused by the random and steadily changing shape of the sea surface and the corresponding diffusely scattered power. However, additional fluctuations are induced by the changing height of the transmitting antenna on the ship. For short distances in the vicinity of the harbor theses changes are obviously small. The height variations become more significant at further distances, where the ship is moving in the open sea region. The mean height of the transmitter during this measurement is approximately 7.8 m above MSL and is depicted as red line. The standard deviation h_0 from the mean height is 0.135 m and was used for the simulations of REL and PO model (i.e. h_0 defined in Section 2.1.1.1).
In Figure 4.2 the received power for Wednesday/hotel/upper floor (48.0 m above MSL) is illustrated. The main difference to the result for Tuesday/lighthouse/upper floor is, that the received power flattens out for distances beyond 9 km. It is assumed, that the signal level

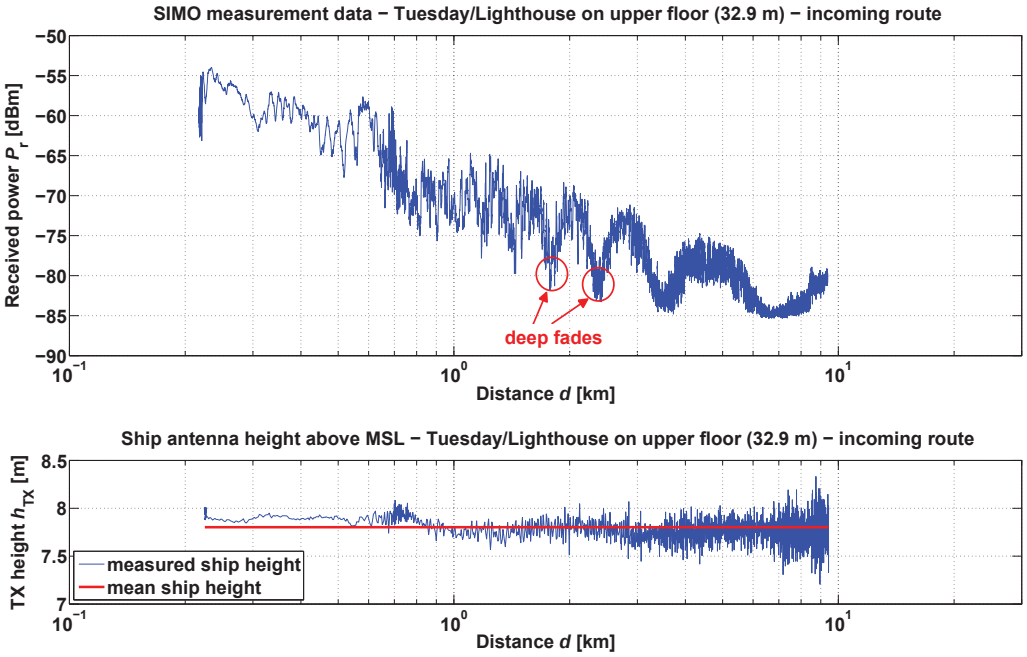

Figure 4.1: Received power and ship antenna height for lighthouse/upper floor

starts to approach the noise floor above ~ 9 km. In general, the noise power is defined as

$$N_{\mathrm{P}} = k_{\mathrm{B}} T B, \tag{4.1}$$

where $k_{\mathrm{B}} \approx 1.38 \times 10^{-23}$ J/K is the Boltzmann constant, T is the noise temperature and B is the bandwidth. Assuming a noise temperature of $T = 20°\mathrm{C} \approx 293$ K, we obtain a noise power or noise floor, respectively, of $N_{\mathrm{P}} \approx -123$ dBW $= -93$ dBm. The sensitivity described by the channel sounder is approximately -87 dBm ([12]).
For this scenario the ship was close to the harbor or even in the harbor at TX-RX-distances around 1 km. Therefore, it is expected, that the strong power fluctuations at distances around 1 km are caused by reflections from the land. For this scenario the calculated dynamic transmitting antenna height has a mean of approximately 8 m and a standard deviation of 0.146 m.
The last SIMO measurement results for Wednesday/hotel/lower floor (32.3m above MSL) are given in Figure 4.3. The signal fading behavior is comparable to the plots above. Also the TX height shows similar variations as before with a mean height of approximately 7.9 m and a standard deviation of 0.195 m. Similar to the scenario Wednesday/hotel/upper floor, the ship was close to the harbor or even in the harbor at TX-RX-distances around 1 km, and the strong power fluctuations are expected to be caused by land reflections.

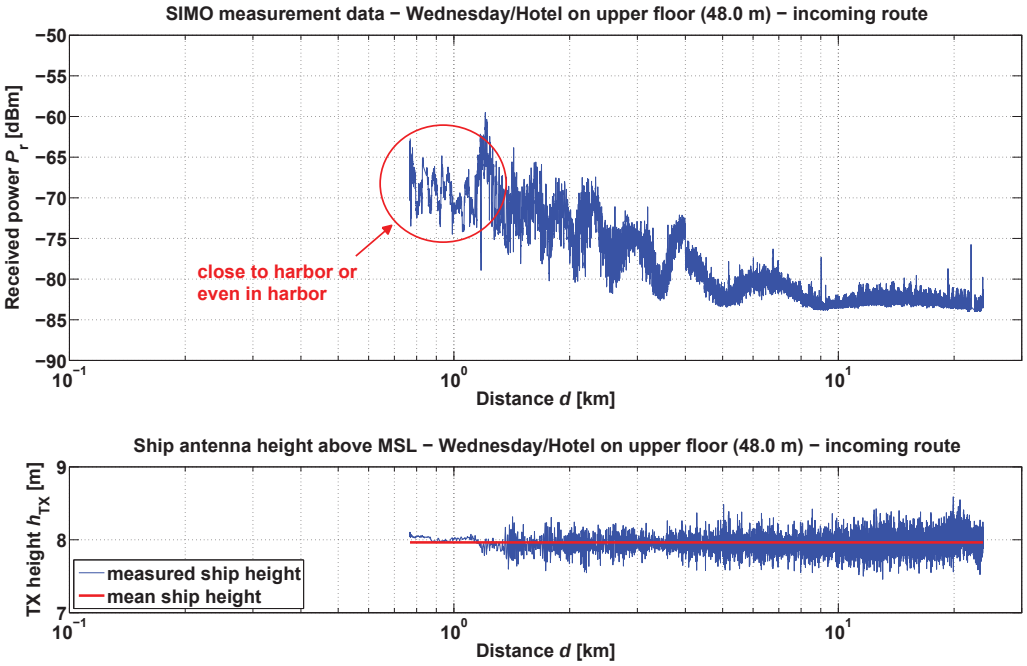

Figure 4.2: Received power and ship antenna height for hotel/upper floor

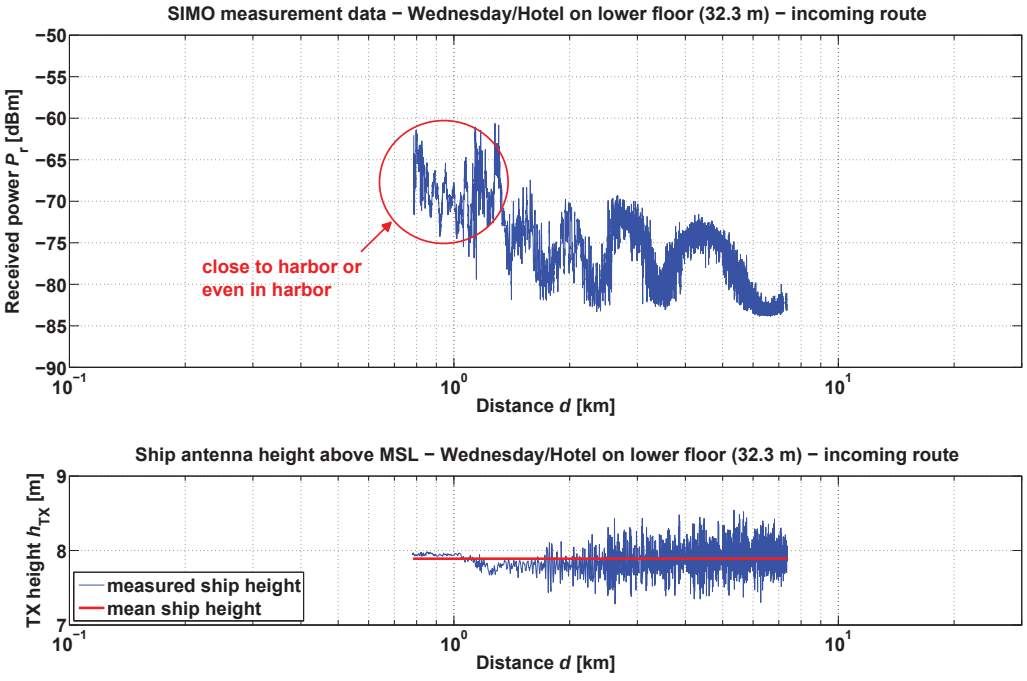

Figure 4.3: Received power and ship antenna height for hotel/lower floor

It is worth noting, that the fading period (i.e. the distance between consequent deep fadings) depends on the heights of transmitter and receiver, because they influence the phases at which the signals arrive at the receive antenna. Since the receiver heights are approximately the same for Tuesday/lighthouse/upper floor (32.9 m above MSL) and Wednesday/hotel/lower floor(32.3 m above MSL), the received power for both scenarios were compared and are depicted in Figure 4.4. We can observe very similar fading periods of the received signal at distances above $\sim$ 1 km, where the two-ray propagation (LOS path + specular reflection) becomes dominant. However, at further distances the received power starts to differ between the two scenarios in terms of received power. Above 3 km the received power is higher for Wednesday/hotel/lower floor than for Tuesday/lighthouse/upper floor. This can be caused by different sea states, which results in different variations of the transmit antenna height and also changes the magnitude of coherent and incoherent signal components. Furthermore the antenna patterns of transmitter and receiver have impacts on the received signal. The distance between the last two deep fades is approximately the same for both scenarios.

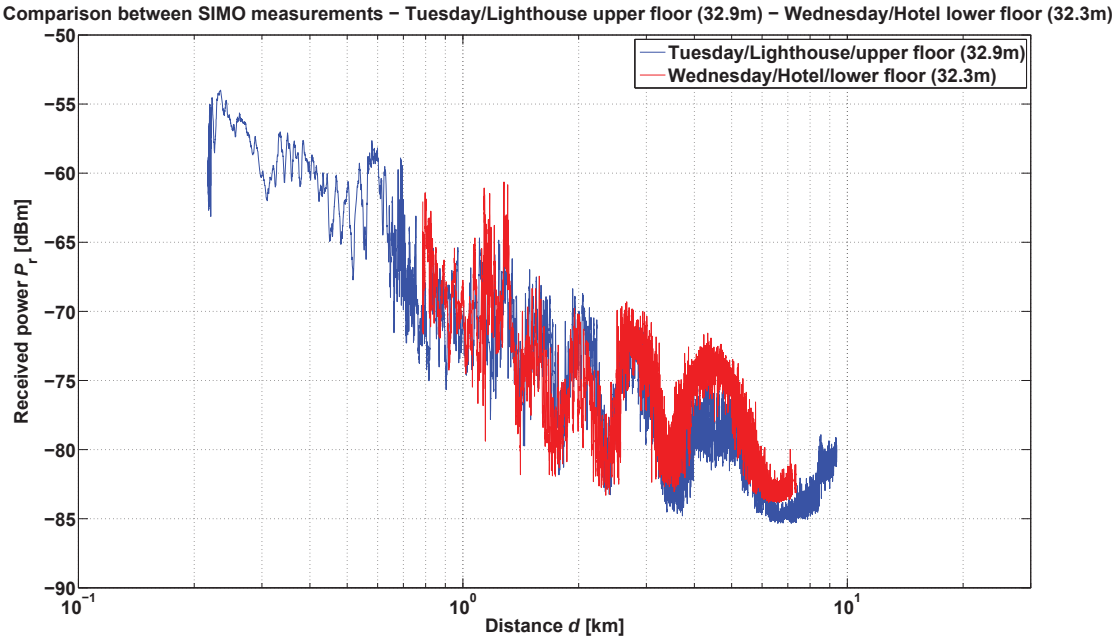

Figure 4.4: Comparison of the received power on lighthouse and hotel

4.2 Model results

In the following subsections the simulation results of the ITU model, the REL model and the PO model corresponding to the measurement scenario on Tuesday/lighthouse/upper floor are presented and discussed. The required input parameters for different models are listed in Table 4.1. The receiver height h_{RX} and the RMS surface height h_0 were calculated from the GPS measurements with PPP. Although the mean transmitter height $h_{\mathrm{TX,m}}$ could have also been computed from the GPS data, it was estimated for each scenario together with the RMS surface slope β_0, to obtain a good match for the fading behavior between measurements and model results (i.e. for the REL and the PO model). Therefore, the mean transmitter heights $h_{\mathrm{TX,m}}$ used for the model simulations differ from the mean TX heights calculated in Section 4.1.
For the estimation a root-mean-square error (RMSE) based estimator was used to minimize the RMSE between the measured and the calculated received power. The REL model was used for the estimation process, because of its simplicity.
The distance d was taken from the GPS measurements, the carrier frequency f_{c} and transmit power P_{t} are shown in Table 3.1 and the antenna gains G_{t} and G_{r} are assumed to be 0 dBi. The water temperature T was set to 4 °C and the salinity to 1.2 %, which are typical values for the Baltic Sea in March. According to 2.3.1 the percentage time, used for the ITU model, was 50%, 10% and 1%.

Input parameter	**ITU model**	**REL model**	**PO model**
Distance d	Yes	Yes	Yes
Transmitter height $h_{\mathrm{TX,m}}$	Yes	Yes	Yes
Receiver height h_{RX}	Yes	Yes	Yes
Carrier frequency f_{c}	Yes	Yes	Yes
Rms surface height h_0	No	Yes	Yes
Rms surface slope β_0	No	Yes	Yes
Water temperature T	No	Yes	Yes
Water salinity S	No	Yes	Yes
Transmit power P_{t}	Yes	Yes	Yes
Transmit antenna gain G_{t}	Yes	Yes	Yes
Receive antenna gain G_{r}	Yes	Yes	Yes
Percentage time t	Yes	No	No

Table 4.1: Required parameters for the models

4.2.1 ITU model results

The ITU simulation results for Tuesday/lighthouse/upper floor are depicted in Figure 4.5, where the RX height is 32.9 m and the estimated mean TX height is 6.29 m above the MSL. This method predicts the signal level exceeded for a specified percentage time and a certain distance, where the model is only valid for distances $d \geq 1$ km. The simulation from 1 km to 10 km results in the illustrated lines. The model delivers good predictions for the different percentage times, e.g. the red line is approximately exceeded for 50% of the time. The alternating constructive and destructive interferences between LOS and specular reflected path, as well as the random fluctuations are not considered in the ITU model.
The ITU model results for the other scenarios can be found in Appendix C.

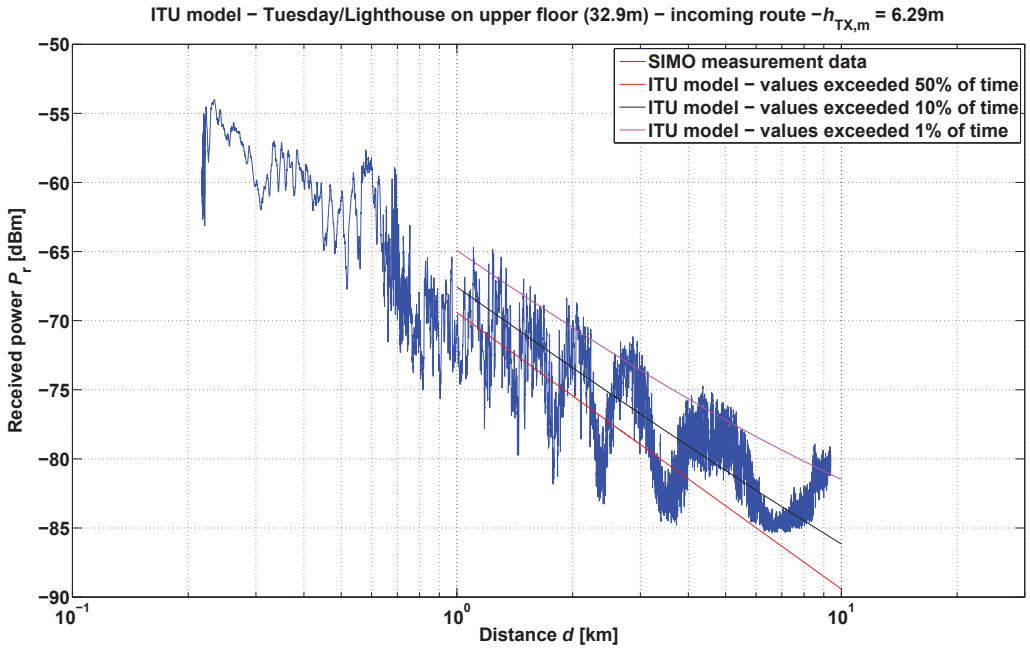

Figure 4.5: ITU model results for lighthouse/upper floor

4.2.2 REL model results

Figure 4.6 illustrates the SIMO measurement data of Tuesday/lighthouse/upper floor (32.9 m above MSL) and the corresponding REL model results. For this measurement the calculated RMS surface height is 0.135 m and the estimated parameters are $\beta_0 = 0.0252$ and $h_{\mathrm{TX,m}} = 6.29$ m. The REL model considers two-ray propagation, it accounts for the interferences of LOS signal and the specular reflection. The effects of shadowing, divergence and diffraction diminish the specular reflection with increasing distance. This means, that the deep fades, caused by destructive interferences, become less significant at further distances. Furthermore the REL model was simulated with the dynamic TX height (see Figure 4.5, lower plot), where its mean was set to the estimated mean height of 6.29 m.
Especially for distances above ~ 1 km, the REL model fits well to the measurement, particularly with regard to the position and significance of constructive and destructive interferences. The fast power variations are caused by the dynamic ship height. The model cannot account for the random signal fluctuations below 1 km, which are assumed to be caused by diffuse scattering from the sea surface. The deep fades disappear for short distances, because the coherent component decreases for smaller angles of incidence (i.e. higher elevation angles) according to (2.29).
The growing difference between measured and simulated received power at distances above 5 km may be caused by the fact, that the measured signal reaches the noise floor, whereas the simulation was performed without noise.
The REL model results for the other scenarios with brief discussions can be found in Appendix C.

Effects of a changing RMS surface height h_0

With growing wave height and corresponding RMS surface height h_0, the specular component decreases according to (2.29). In case of the REL model, only the LOS component (i.e. a straight line) would remain, if the specular reflection diminishes to zero. On the other hand, deep fades would also occur at short distances for a smooth sea surface(i.e. $h_0 = 0$). The RMS surface height does not affect the distance between two subsequent deep fades.

Effects of a changing RMS surface slope β_0

With respect to the REL model the RMS surface slope only has an effect on the shadowing factor S defined in Eq. (2.37). In case of a perfectly smooth surface (i.e. $\beta_0 = 0$) no shadowing occurs and the reflection coefficient is not diminished. With increasing surface roughness and therefore increasing β_0, the shadowing effect becomes more important and S decreases. This causes a decline of the reflection coefficient and less significant interferences. Similar to h_0, the RMS surface slope does not influence the distance between two subsequent deep fades.

Effects of changing heights h_{TX} and h_{RX}

In contrast to h_0 and β_0, the TX and RX heights do not have much impact on the fading depth, but on the fading periods. Changing heights of transmitter and/or receiver result in changing path differences between LOS component and specular reflection. Therefore, the heights influence where constructive and destructive interferences appear.

To summarize, it can be noted, that the RMS surface height and the RMS slope affect the significance of the signal fadings, whereas the heights of transmitter and receiver have an impact on the fading period.

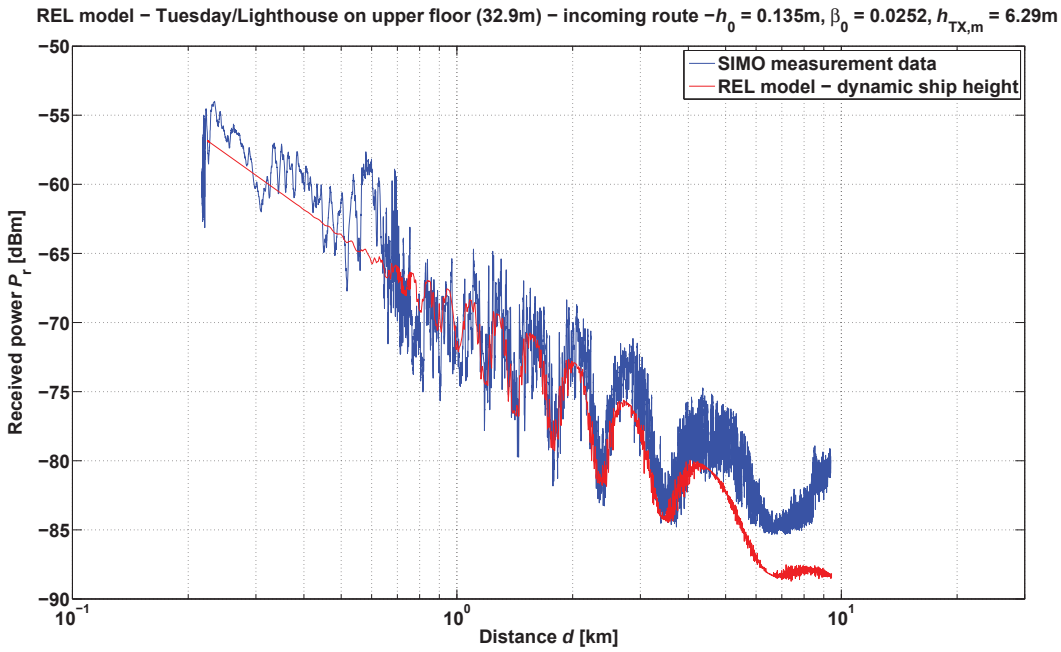

Figure 4.6: REL model results for lighthouse/upper floor

4.2.3 PO model results

Figure 4.7 shows the results for Tuesday/lighthouse/upper floor (32.9 m above MSL) for the proposed PO model. The used values for h_0, β_0 and $h_{\mathrm{TX,m}}$ are the same as for the REL model in Section 4.2.2. In contrast to the REL model in the previous section, the transmitter height is assumed to be static for the PO model. Due to the additional consideration of the incoherent component, this prediction method considers random fluctuations of the received power, induced by the diffuse scattering from the sea surface. Thus the PO model achieves a very good match with the measurement results over the entire distance range. At distances beyond 5 km the measured signal starts to approach the noise floor and the computed P_r deviates from the measurement, since noise is not considered in the model.
For short distances below ∼1 km, the incoherent component is predominant and superimposes random fluctuations on the LOS signal. With increasing distance the specular reflection starts to grow stronger and the diffuse scattering decreases at the same time. Therefore the typical constructive and destructive interferences between LOS and coherent component appear at distances above ∼1 km, still superimposed by the fast variations of the incoherent component.

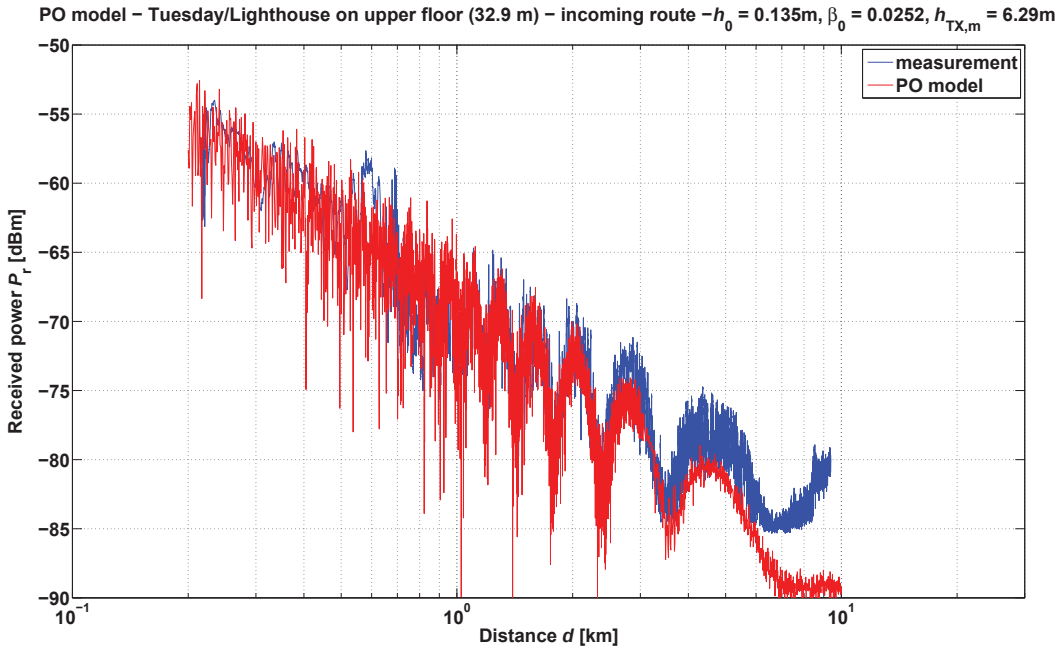

Figure 4.7: PO model results for lighthouse/upper floor

This behavior can be observed in detail in Figure 4.8, where the different signal components are depicted separately. The solid black line represents the LOS signal, which corresponds to the FSL. The green line shows the PO model result for a two-ray propagation (LOS and specular reflection), which is similar to the REL model. As shown in Figure 4.8, the superposition of all three components (i.e. the total received power) is illustrated in red. The interesting parts are the trends of coherent and incoherent component. The behavior of both

can be best explained by the roughness parameter u, which is defined in Eq. (2.28). Since the electromagnetic wavelength is fixed, u depends on the RMS surface height h_0, the angle of incidence Θ_i and the scattering angle Θ_s.
For a perfectly smooth sea (i.e. $h_0 = 0$ and $u = 0$) the coherent component reaches a maximum and the incoherent component decreases to zero. This would result in a simple two-ray propagation without random signal variations, where the coherent component only depends on the Fresnel reflection coefficient. With growing h_0 the coherent component is decreased and the diffuse scattering increases.
Since h_0 is assumed to be constant during the simulations, the roughness parameter is only affected by the angles Θ_i and Θ_s, where u has its maximum for $\Theta_i = \Theta_s = 0$ (vertical incidence and reflection) and it decreases with increasing angles Θ_i and Θ_s (i.e. decreasing elevation angles). Therefore, the coherent component is very weak at short distances. For increasing TX-RX-distances the specular reflection becomes stronger and it exceeds the incoherent component between 1 and 2 km (cf. Figure 4.8). Above this distance the constructive and destructive interferences between direct LOS signal and coherent component become dominant. At the same time the diffuse scattering looses the significance with increasing separation of transmitter and receiver.

The effects of h_0, β_0 and the heights of TX and RX on the fading depth and period are discussed in Section 4.2.2. The PO model results for the other scenarios with brief discussions can be found in Appendix C.

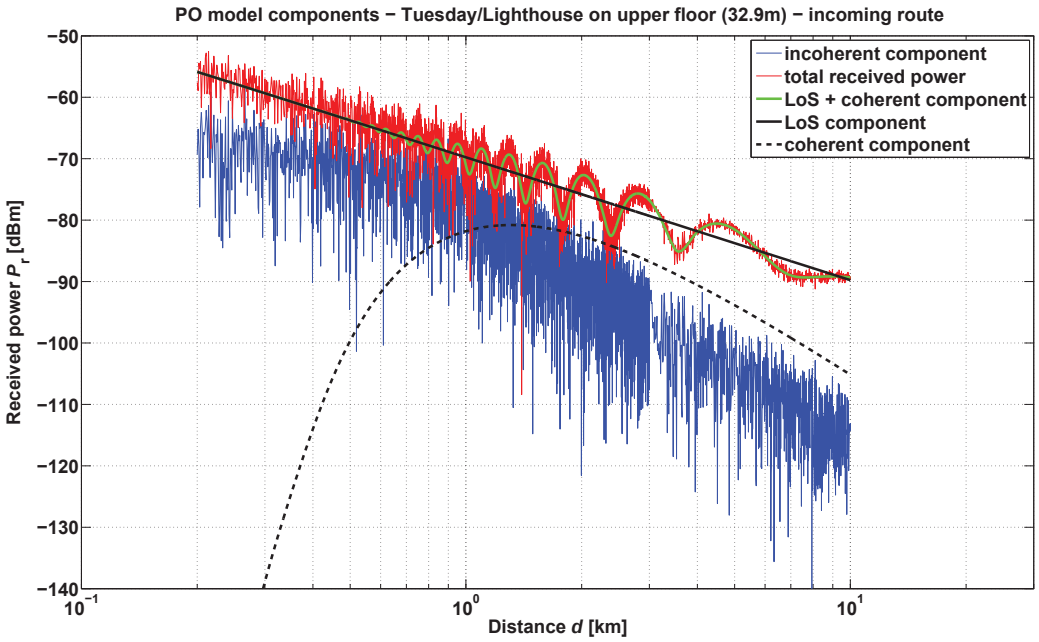

Figure 4.8: PO model - separated components for lighthouse/upper floor

In Figure 4.9 the scattering coefficient σ_0 given in Eq. (2.53) is visualized. The distance between transmitter and receiver is 500 m in x-direcion. σ_0 is dimensionless and is represented linearly. It is important to note, that x- and y-axis are not equally scaled. This means, scattering mainly occurs within a narrow and elongated region between TX and RX.

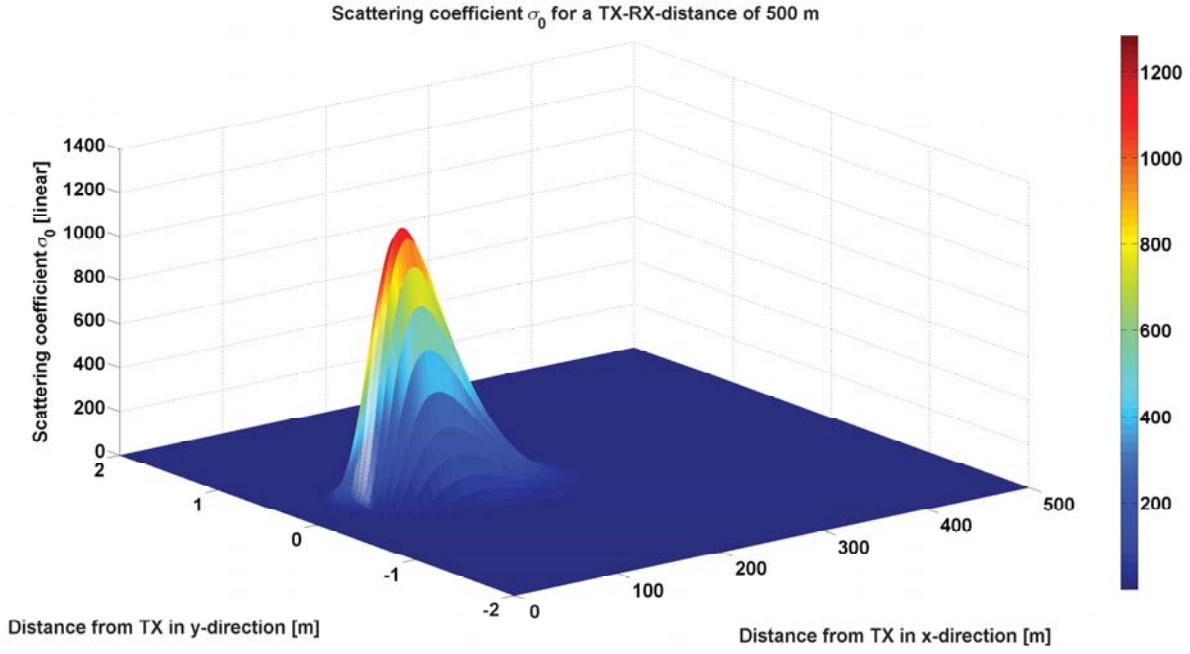

Figure 4.9: Scattering coefficient for lighthouse/upper floor for a TX-RX-distance of 500 m

5 Wideband propagation model

Currently, there are no available maritime channel models for the simulation of terrestrial wideband communications. Therefore, a novel maritime wideband channel model is proposed, based on the principle of the PO model. The output of the wideband channel model is a prediction of the CIR.
First, we focus on the development of the wideband model, followed by a comparison between the measurements and the model results in terms of PDP, mean delay and RMS delay spread.

5.1 Proposed channel model

The wideband channel model is based on the same geometric background as for the PO model, shown in Figure 2.10. In the PO model, the sea surface lies in the xy-plane and is divided into equally sized tiles (cf. Figure 2.10). The diffuse scattering contribution of each tile is computed separately, where the normal vectors of all tiles show in the z-direction. Regarding path loss predictions, this approach of wave propagation delivers good results. However, it is only suitable to a limited extend for the modeling of a realistic wave propagation over the sea, particularly with respect to multipath propagation. The reason for this can be observed in Figure 4.9, where the scattering coefficient σ_0 of the sea surface is illustrated. σ_0 is limited to a narrow area between TX and RX. Consequently, the PO model would not be able to account for MPCs, originating from a region outside this limited scattering area, e.g. behind the TX or RX, respectively.
Therefore, a virtual sea surface is created in the xy-plane for the wideband propagation model. The method to create the sea surface is based on the findings in [13], where a Gaussian PDF is assumed for the wave height. The main input parameter for the surface generation is the significant wave height h_s, which is related to the RMS surface height h_0 as $h_s \approx 4h_0$ ([4]). Hence, it is possible to generate a random sea surface according to the values of h_0 obtained from the different measurement scenarios. Figure 5.1 shows an exemplary sea surface for h_s = 1 m, with dimensions of 200 m × 200 m in x- and y-direction, respectively. Similar to the PO model, the sea surface is then divided into tiles, as indicated by the black grid.
Since each tile has different orientation, the normal vectors are calculated for all tiles. Using these normals, we assume a local Cartesian coordinate system (cf. Figure 2.9) for each tile. In this way the local incidence, scattering and azimuth angles Θ_i, Θ_s and Φ_s, respectively, with respect to the TX and RX positions, are computed for each tile.
To calculate the scattering coefficient σ_0 of each tile, the surface roughness of the tiles is required. Therefore, we assume, that the sea surface is composed of meter scale waves and superimposed centimeter scale capillary waves ([5], page 783 et seq.). The large scale waves are represented by the generated sea surface. The small centimeter scale waves are used, to describe the surface roughness of the tiles. For the computation of σ_0, we assume small scale

waves in the centimeter and sub-centimeter region, e.g. a RMS surface height of the small waves $h_{0,\mathrm{s}} = 0.5$ cm.
This allows us to compute the magnitude of the scattered field from each tile of the surface. The phase shift due to scattering from the rough sea surface is assumed to be uniformly distributed over $[0, 2\pi)$. The LOS signal is calculated according to the distance between TX and RX. Therefore, the LOS component and the diffuse scattering components from all tiles can be described in terms of their magnitudes and phases.
With this approach, we can describe multipath propagation over sea in a more realistic way, compared to the PO model. Due to the fact, that the orientations of the tiles are considered, MPCs can originate from a larger area and even from behind the TX and the RX.
It is worth noting, that the wideband model is not suitable for short TX-RX-distances below 1 km, since it can not account for reflections from objects on land or ships.

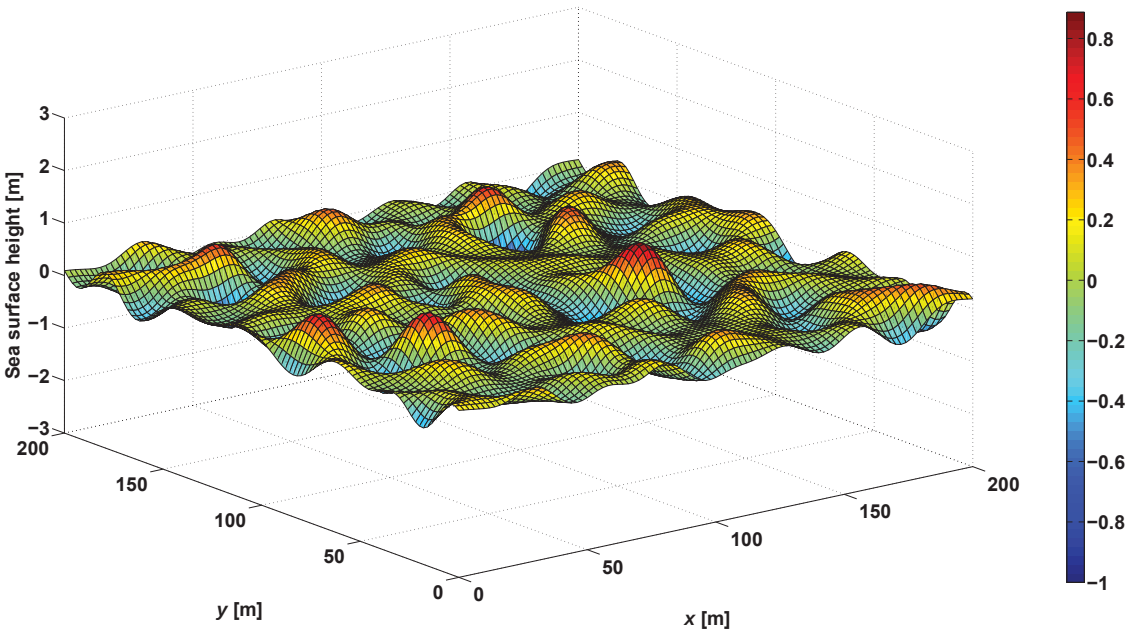

Figure 5.1: Random sea surface for the wideband propagation model for $h_{\mathrm{s}} = 1$ m

In the following, we focus on the mathematical description of the CIR. In the next section the measurements are compared to the corresponding wideband model simulations in terms of the PDP, the mean excess delay m_{D} and the RMS delay spread σ_{D}.
The outputs of the wideband channel model are the amplitudes of the LOS component, the specularly reflected component and the scattered components from the tiles, as well as the corresponding propagation distances and delays, respectively. In the following the amplitudes are denoted by the quantity α, the distances by d and the delays by τ.

The time-variant CIR can be written as

$$\begin{aligned} h(t,\tau) &= \alpha_{\mathrm{LOS}}(t)\delta\left(\tau - \frac{d_{LOS}(t)}{c}\right) + \alpha_{\mathrm{Refl}}(t)\delta\left(\tau - \frac{d_{\mathrm{Refl}}(t)}{c}\right) + ... \\ &\quad ... + \sum_{m=1}^{M} \alpha_m(t)\delta\left(\tau - \frac{d_{\mathrm{TX},m}(t) + d_{\mathrm{RX},m}(t)}{c}\right) \\ &= \alpha_{\mathrm{LOS}}(t)\delta(\tau - \tau_{LOS}(t)) + \alpha_{\mathrm{Refl}}(t)\delta(\tau - \tau_{\mathrm{Refl}}(t)) + \sum_{m=1}^{M} \alpha_m(t)\delta(\tau - \tau_m(t)), \end{aligned} \tag{5.1}$$

with the δ-function defined as

$$\delta(x) = \begin{cases} 1 & \text{for } x = 0, \\ 0 & \text{for } x \neq 0, \end{cases} \tag{5.2}$$

where α_{LOS} is the amplitude of the electric field strength of the LOS component and d_{LOS} is the distance between TX and RX. α_{Refl} is the amplitude of the specularly reflected electric field strength and d_{Refl} is the sum of the distances from the TX to the specular reflection point and from the RX to the specular reflection point. M is the total number of tiles and m denotes the indices of the tiles. α_m is the amplitude of the electric field of the m-th tile and $d_{\mathrm{TX},m}$ and $d_{\mathrm{RX},m}$ are the distances from the m-th tile to the TX and RX, respectively. The continuous propagation delays of the LOS component, the specularly reflected component and the scattered components are given by τ_{LOS}, τ_{Refl} and τ_m, respectively. The continuous time variable t indicates, that the CIR varies with time. The quantity δ denotes the Dirac delta function.
The CIR in Eq. (5.1) can alternatively be written in the frequency domain as the transfer function of the channel as

$$\begin{aligned} H(t,f) &= \alpha_{\mathrm{LOS}}(t)\exp\left(-j2\pi f\frac{d_{\mathrm{LOS}}(t)}{c}\right) + \alpha_{\mathrm{Refl}}(t)\exp\left(-j2\pi f\frac{d_{\mathrm{Refl}}(t)}{c}\right) + ... \\ &\quad ... + \sum_{m=1}^{M} \alpha_m(t)\exp\left(-j2\pi f\frac{d_{\mathrm{TX},m}(t) + d_{\mathrm{RX},m}(t)}{c}\right)\exp(j\Phi_R) \\ &= \alpha_{\mathrm{LOS}}(t)\exp(-jkd_{\mathrm{LOS}}(t)) + \alpha_{\mathrm{Refl}}(t)\exp(-jkd_{\mathrm{Refl}}(t)) + ... \\ &\quad ... + \sum_{m=1}^{M} \alpha_m(t)\exp(-jk(d_{\mathrm{TX},m}(t) + d_{\mathrm{RX},m}(t)))\exp(j\Phi_R) \\ &= \alpha_{\mathrm{LOS}}(t)\exp\left(-j2\pi f\tau_{\mathrm{LOS}}(t)\right) + \alpha_{\mathrm{Refl}}(t)\exp\left(-j2\pi f\tau_{\mathrm{Refl}}(t)\right) + ... \\ &\quad ... + \sum_{m=1}^{M} \alpha_m(t)\exp\left(-j2\pi f(\tau_m(t))\right)\exp(j\Phi_R), \end{aligned} \tag{5.3}$$

where f is the frequency, k is the corresponding wavenumber and Φ_{R} denotes the uniformly distributed random phase of the scattered components (cf. Section 2.4).
Eq. (5.1) and (5.3) show the CIR and the transfer function, respectively, in a general and continuous form with respect to time t, delay τ and frequency f. To enable a comparison between measurements and simulations, the transfer function has to be discretized with respect to time and frequency. Therefore, we assume a broadband signal, with a total

bandwidth B, consisting of N_C sub-carriers with a sub-carrier spacing of B_{sc}. The sub-carrier frequencies are given by

$$f_n = f_c + nB_{\text{sc}} \tag{5.4}$$

with

$$n = \begin{cases} -\frac{N_{\text{C}}-1}{2} \ldots \frac{N_{\text{C}}-1}{2} & \text{for odd } N_{\text{C}}, \\ -\frac{N_{\text{C}}}{2} \ldots \frac{N_{\text{C}}}{2} - 1 & \text{for even } N_{\text{C}}, \end{cases} \tag{5.5}$$

where f_c is the RF center frequency and n denotes the indices of the sub-carriers. Hence, the discrete transfer function is given as

$$\begin{aligned} H(t_v, f_n) &= \alpha_{\text{LOS}}(t_v) \exp\left(-j2\pi f_n \frac{d_{\text{LOS}}(t_v)}{c}\right) + \alpha_{\text{Refl}}(t_v) \exp\left(-j2\pi f_n \frac{d_{\text{Refl}}(t_v)}{c}\right) + \ldots \\ &\quad \ldots + \sum_{m=1}^{M} \alpha_m(t_v) \exp\left(-j2\pi f_n \frac{d_{\text{TX},m}(t_v) + d_{\text{RX},m}(t_v)}{c}\right) \exp(j\Phi_R) \\ &= \alpha_{\text{LOS}}(t_v) \exp\left(-j2\pi f_n \tau_{\text{LOS}}(t_v)\right) + \alpha_{\text{Refl}}(t_v) \exp\left(-j2\pi f_n \tau_{\text{Refl}}(t_v)\right) + \ldots \\ &\quad \ldots + \sum_{m=1}^{M} \alpha_m(t_v) \exp\left(-j2\pi f_n (\tau_{\text{TX}}(t_v) + \tau_{\text{RX}}(t_v))\right) \exp(j\Phi_R) \\ &= \alpha_{\text{LOS}}(t_v) \exp(-jk_n d_{\text{LOS}}(t_v)) + \alpha_{\text{Refl}}(t_v) \exp(-jk_n d_{\text{Refl}}(t_v)) + \ldots \\ &\quad \ldots + \sum_{m=1}^{M} \alpha_m(t_v) \exp(-jk_n (d_{\text{TX},m}(t_v) + d_{\text{RX},m}(t_v))) \exp(j\Phi_R), \end{aligned} \tag{5.6}$$

with the discrete time variable

$$t_v = v\Delta t \qquad (v = 0,1,\ldots), \tag{5.7}$$

where Δt is the time difference between consecutive CIRs. The length of the transfer function corresponds to the number of sub-carriers.
To obtain the sampled CIR, we have to transform the transfer function $H(t_v, f_n)$ into the time domain. Using the inverse discrete Fourier Transform (IDFT), the time varying, sampled CIR is given as

$$h(t_v, \tau_l) = \frac{1}{N_{\text{C}}} \sum_{n=0}^{N_{\text{C}}-1} H(t_v, f_n) \exp\left(-\frac{j2\pi f_n \tau_l}{N_{\text{C}}}\right), \tag{5.8}$$

with the discrete delay τ_l as

$$\tau_l = l\Delta\tau \qquad (l = 0,1,\ldots,N_{\text{C}} - 1), \tag{5.9}$$

where the delay resolution $\Delta\tau = 1/B$. The CIR has the same length as the transfer function and the duration of a single CIR is $\Delta\tau(N_{\text{C}} - 1)$.
For the LOS condition between TX and RX, the maximum of the CIR, i.e. the LOS path, arrives first at the receiver at a certain delay τ_0. It is worth to note, that the delay is normalized to the LOS path delay, such that $\tau_0 = 0$. Since this condition may not be fulfilled by the computed CIRs, their maxima have to be shifted in terms of the delay τ_l towards τ_0. An illustration of the shifted, time varying CIR is shown in Figure 5.2.

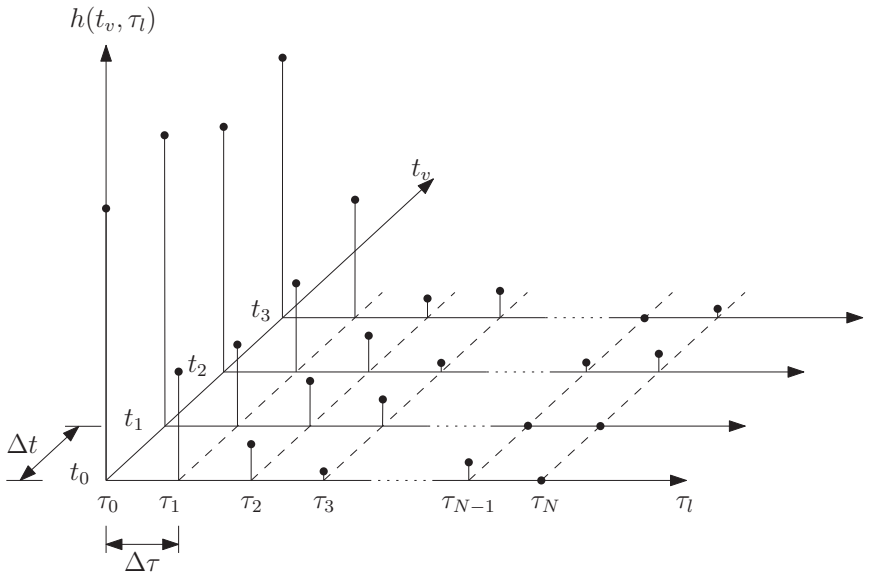

Figure 5.2: Example of a shifted and time varying channel impulse response

5.2 Comparison between measurements and wideband channel model

To compare the measurements and the simulations in terms of wideband channel characteristics, the PDP and the time dispersion parameters m_{D} and σ_{D} are considered. The time dispersion parameters are discussed in detail in Section 5.2.4. In order to compute these parameters, the PDP is required. According to [8] (page 185), the PDP is the average of the shifted and squared CIR, i.e. $|h(t_v, \tau_l)|^2$, over a local area and a certain number of snapshots at consecutive times t_v. In this work, we average over a traveled distance over sea of 10 m, which corresponds to approximately 50 CIR snapshots during the measurement. Therefore, we use $K_{\mathrm{M}} = 50$ consecutive CIR snapshots to compute the PDPs of the measurements. Due to computational reasons, we only use $K_{\mathrm{S}} = 10$ CIR snapshots to compute the PDPs of the simulations. Since the SIMO measurements are considered, the CIRs were measured by each antenna array element separately. Therefore, we additionally take the average of the measured CIRs of the selected elements, to compute the PDP of the measurement. The number of selected elements is given by A_{S} and the different elements are denoted by the index a, where $a = 1, 2, ..., A_{\mathrm{S}}$.
Hence, the PDP of the measurement is calculated as

$$P_{meas}(\tau_l) = \frac{1}{A_{\mathrm{S}} K_{\mathrm{M}}} \sum_{a=1}^{A_{\mathrm{S}}} \sum_{v=0}^{K_{\mathrm{M}}-1} |h_a(t_v, \tau_l)|^2 \tag{5.10}$$

and the PDP of the simulation as

$$P_{sim}(\tau_l) = \frac{1}{K_{\mathrm{S}}} \sum_{v=0}^{K_{\mathrm{S}}-1} |h(t_v, \tau_l)|^2. \tag{5.11}$$

In the next subsections the PDPs of the measurements and the simulations for a certain TX-RX-distance are shown and discussed. Furthermore, we compare them in terms of mean excess delay and RMS delay spread. We used a center frequency of $f_c = 5.2$ GHz, a bandwidth of $B = 100$ MHz, a number of sub-carriers of $N_C = 1281$ and a sub-carrier spacing of $B_{\text{sc}} = 78.125$ kHz as input-parameters for the wideband model simulations, corresponding to the broadband measurement signal (cf. Section 3.1, Table 3.1). The total bandwidth of the measurement signal results in a delay resolution of $\Delta\tau = 1/B = 10$ ns.

5.2.1 Power delay profiles of the measurements

The power delay profiles of the measurements were calculated for all three scenarios for TX-RX-distances of 3 km, 4 km and 5 km. At these distances, there was always a clear LOS between the transmitter and the receiver.
The PDP of the measurement for Tuesday/lighthouse/upper floor for a TX-RX-distance of 5 km is shown and discussed in the following. The remaining PDPs for the scenarios Tuesday/lighthouse/upper floor (3 km and 4 km) and Wednesday/hotel/upper and lower floor, respectively, are illustrated and discussed in Appendix D.
This work focuses only on reflections and scattered components from the sea surface and it does not account for reflections from the land. Since the reflections from the sea surface have short delays, we only consider the first 1000 ns of the PDPs of the measurements and omit any reflections from the land or other vessels, that arrive later.

Figure 5.3 shows the PDP for the lighthouse measurement. We can see, that the strong LOS path arrives at first. It decreases very fast until it converges to a level of about -35 dB below the LOS power. This level represents the noise floor, which means that the signal-to-noise ratio (SNR) is about 35 dB. It is worth to note, that due to averaging over 50 CIR snapshots, the theoretic noise power of $N_\mathrm{P} \approx -93$ dBm (cf. Eq. (4.1)) decreases to a level of about -115 dBm. After the LOS peak, no reflections occur within 1000 ns. The PDPs for the different distances are compared in Section 5.2.4 in terms of mean excess delay and RMS delay spread.

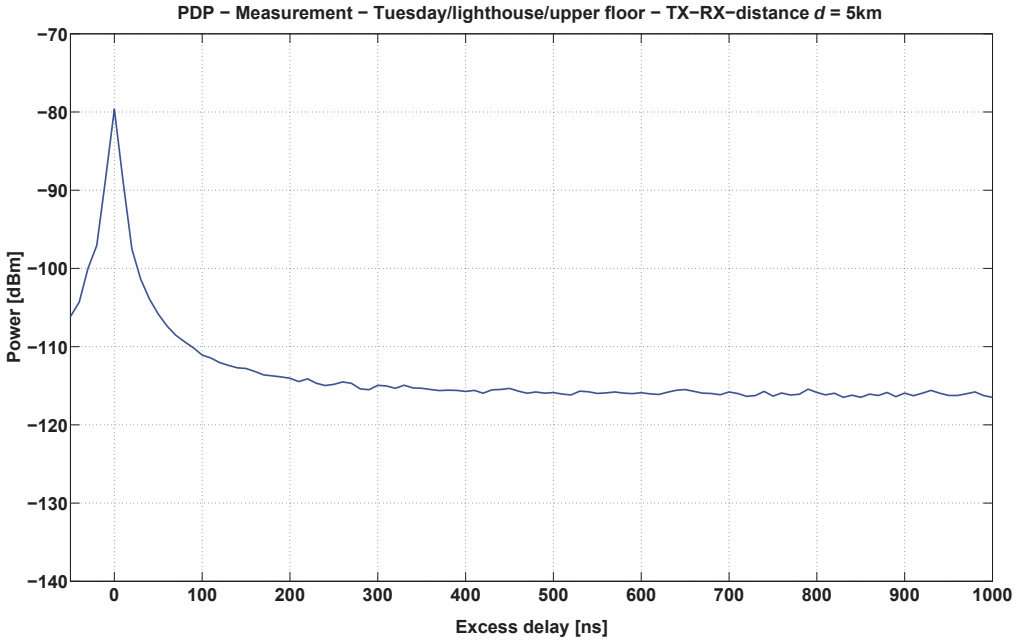

Figure 5.3: PDP of the measurement on lighthouse/upper floor for a TX-RX-distance of 5 km

5.2.2 Power delay profiles of the simulations

For the simulations, the following parameters were used:

- $h_{\mathrm{RX}} = 32.9$ m above MSL,
- estimated $h_{\mathrm{TX},m} = 6.26$m above MSL,
- RMS surface height of the large scale waves: $h_0 = 0.1347$ m,
- assumed RMS surface height of the small scale waves: $h_{0,\mathrm{s}} = 0.5$ cm,
- assumed RMS surface slope of the small scale waves: $\beta_{0,\mathrm{s}} = 0.05$.

The values for $h_{0,\mathrm{s}}$ and $\beta_{0,\mathrm{s}}$ of the small scale waves define the roughness of the tiles.
Figure 5.4 visualizes the PDP of the simulation of Tuesday/lighthouse/upper floor for a TX-RX-distance of 5 km. Since no multipaths from reflecting objects can occur in the simulations, the excess delay is limited to 1000 ns. Similar to the PDP of the measurement in the previous section, the first arriving LOS path falls off rapidly. However, compared to the measurement, the power decreases to lower values in the simulations. The reason for this is, that no noise is considered in the wideband model. Therefore, the calculated power can drop even below the computed noise floor of the measurement of about -115 dBm (cf. Section 5.2.1). The direct comparisons between the PDPs of the measurement and the simulation are shown in the following Section 5.2.3.
The PDPs of the simulations of Tuesday/lighthouse/upper floor (3 km and 4 km) and Wednesday/hotel/upper and lower floor, respectively, are shown in Appendix D.

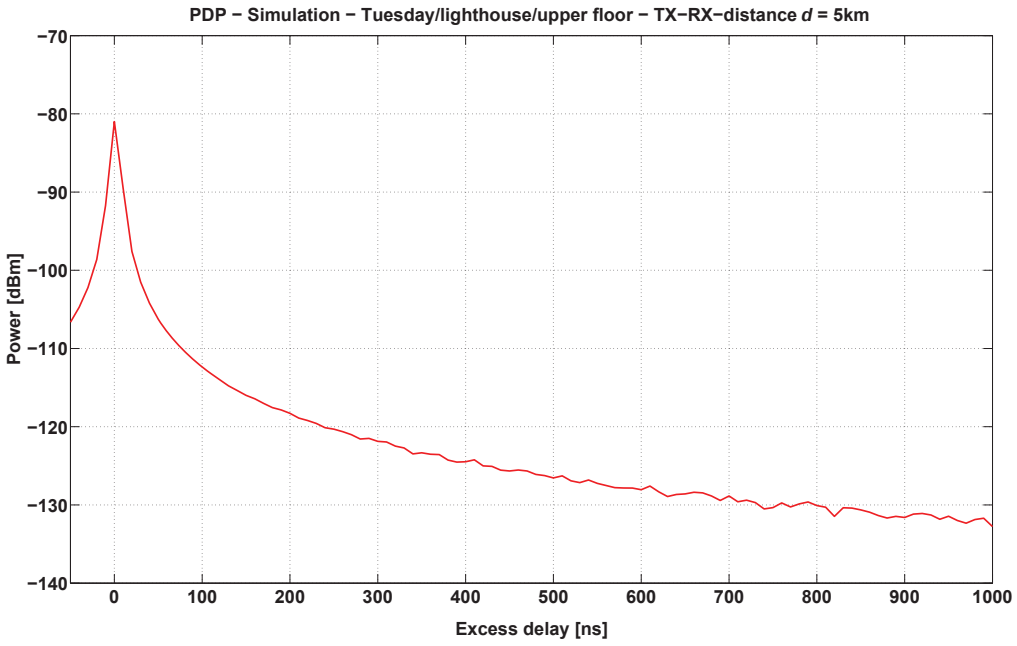

Figure 5.4: PDP of the simulation for lighthouse/upper floor for a TX-RX-distance of 5 km

5.2.3 PDP comparison between measurements and simulations

Figure 5.5 compares the PDPs of the measurement and the simulation of Tuesday/lighthouse/upper floor for a TX-RX-distance of 5 km. We can observe a very good match between measurement and simulation below 100 ns in terms of power and width of the PDP. For higher delays, the deviation between them becomes more significant. The PDP of the measurement reaches the noise floor, whereas the one of the simulation decreases to lower values. Additionally, the PDP of the LOS component is visualized in black. The power of the LOS component is below the total received powers of the measurement and the simulation. The reason for this can be explained referring to Figure 4.8, where the components of the PO model for Tuesday/lighthouse/upper floor are illustrated. Due to constructive interference between LOS component and specular component, the total received power is above the LOS power. Superimposed onto the LOS component and the specular component is the scattering component, which decreases with increasing distance. Therefore, the scattering component is already very weak at the simulation distance of 5 km. Since the heights of transmitter and receiver are very small compared to the large TX-RX-distance, the LOS component, the specular reflected component and the major part of the scattered component arrive within the first delay bin, i.e. within 10 ns. Therefore, the PDP consists of one narrow peak. For shorter distances, the path difference between LOS component and reflected and scattered components, respectively, becomes larger. Hence, the width of the PDP is expected to get wider with decreasing TX-RX-distance.
The comparisons for the scenarios Tuesday/lighthouse/upper floor (3 km and 4 km) and Wednesday/hotel/upper and lower floor, respectively, are illustrated in Appendix D.

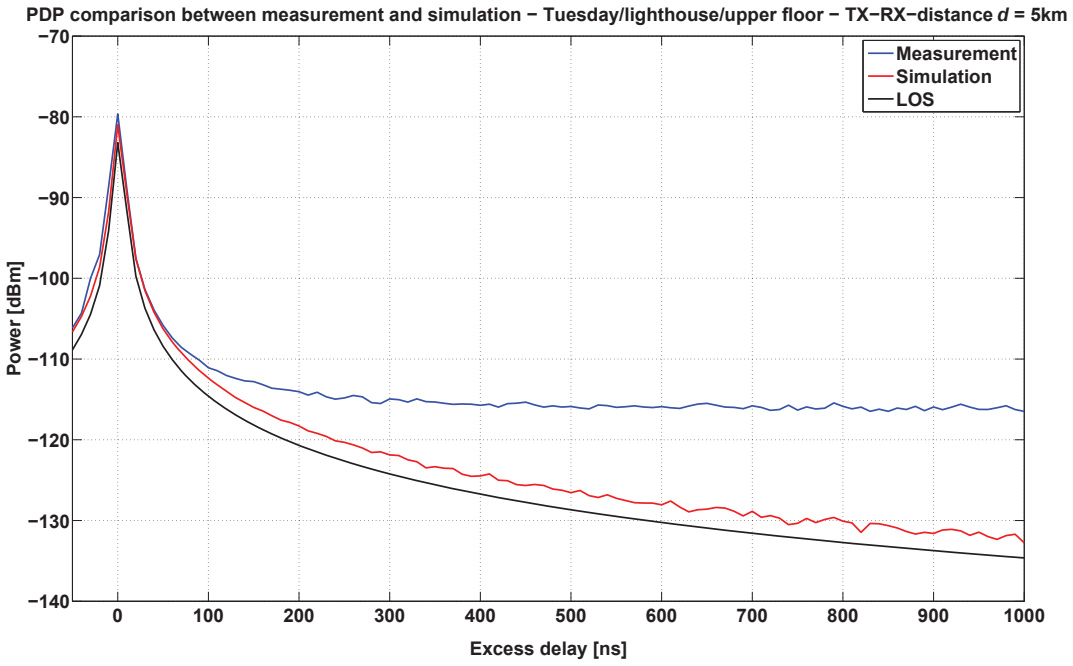

Figure 5.5: PDP comparison for lighthouse/upper floor for a TX-RX-distance of 5 km

5.2.4 Time dispersion parameters

The time dispersion parameters m_{D} and σ_{D} are used, to characterize a multipath channel. They enable a comparison of different wireless channels and are used for the design of wireless communication systems. In the following, these parameters are calculated, to compare the measurement and the simulation. The mean excess delay m_{D} and the RMS delay spread σ_{D} are computed, similar to the definitions in [8](page 199), as

$$m_{\mathrm{D}} = \frac{\sum_{l=0}^{N_{\mathrm{C}}-1} \Gamma\left(P(\tau_l)\right) \tau_l}{\sum_{l=0}^{N_{\mathrm{C}}-1} \Gamma\left(P(\tau_l)\right)} \tag{5.12}$$

and

$$\sigma_{\mathrm{D}} = \sqrt{\frac{\sum_{l=0}^{N_{\mathrm{C}}-1} \Gamma\left(P(\tau_l)\right) \tau_l^2}{\sum_{l=0}^{N_{\mathrm{C}}-1} \Gamma\left(P(\tau_l)\right)} - m_{\mathrm{D}}^2}, \tag{5.13}$$

where the threshold function $\Gamma(P(\tau_l))$ is defined as

$$\Gamma(P(\tau_l)) = \begin{cases} P(\tau_l) & \text{for } P(\tau_l) \geq P_t(\tau_l) \\ 0 & \text{otherwise.} \end{cases} \tag{5.14}$$

The threshold function is used, to consider only strong multipath components above the threshold P_t and omit weaker components and noise samples. In the following, we assume the threshold to be 20 dB below the maximum of the PDP. For the calculation of the time dispersion parameters of the measurements and the simulations, we use the definitions of the PDP in (5.10) and (5.11), respectively.
In Table 5.1 the results of m_{D} for the measurements and the simulations of all scenarios are summarized for different TX-RX-distances. Regarding the measurement, we can observe, that the mean delay is similar for the most scenarios. Only the scenario Wednesday/hotel/upper floor has higher mean delays compared to the other two scenarios at distances of 4 km and 5 km. The simulation results of m_{D} fit well to the measurement results, except for Tuesday/lighthouse/upper floor at 3 km and Wednesday/hotel/upper floor at 5 km. For this case, the deviation between measurement and simulation is larger, compared to the rest. Especially for the shorter distance of 3 km, this deviation can be caused by the increasing impact of the scattering.
In Table 5.2 we can see the corresponding results of σ_{D} for the measurements and the simulations. As for the mean delay, the values for the delay spread are approximately the same for most scenarios. Only the simulation of Tuesday/lighthouse/upper floor at 3 km and the measurements of Wednesday/hotel/upper floor at 4 km and 5 km show higher values for σ_{D}. Similar to the result for m_{D} before, the measurements and the simulations show a good match in terms of RMS delay spread. Slight differences between measurements and simulations only appear for Tuesday/ Wednesday/hotel/upper floor at 4 km and 5 km.

		Mean excess delay m_{D}	
	Distance	Measurement	Simulation
	km	ns	ns
Tuesday/lighthouse/upper floor	3	1.28	2.83
	4	1.31	1.21
	5	1.34	1.59
Wednesday/hotel/upper floor	3	1.30	1.07
	4	1.74	1.34
	5	2.75	1.53
Wednesday/hotel/lower floor	3	1.17	1.12
	4	1.21	1.20
	5	1.34	1.59

Table 5.1: Mean excess delay m_{D} for measurements and simulations at different distances

		RMS delay spread σ_{D}	
	Distance	Measurement	Simulation
	km	ns	ns
Tuesday/lighthouse/upper floor	3	3.81	6.02
	4	3.82	3.72
	5	3.81	4.14
Wednesday/hotel/upper floor	3	3.89	3.56
	4	4.98	3.87
	5	6.64	4.09
Wednesday/hotel/lower floor	3	3.71	3.61
	4	3.77	3.71
	5	3.90	4.15

Table 5.2: RMS delay spread σ_{D} for measurements and simulations at different distances

6 Conclusion

The development of new algorithms for future maritime wireless communication systems and navigational applications requires a comprehensive knowledge of the maritime radio propagation channel. The objective of this thesis was to investigate the electromagnetic propagation characteristics over sea for C-Band at 5.2 GHz, with a main focus on the scattering phenomenon caused by the sea surface. Therefore, the characterization of the sea surface, as well as the major electromagnetic propagation mechanisms over sea were discussed in detail at the beginning of this thesis. Based on this theoretic background, three state-of-the-art maritime channel models, i.e. the Recommendation ITU-R P.1546-2, the Round Earth Loss model and Karasawa's model, were introduced. All three models were proposed for frequencies below 5.2 GHz. In contrast to the first two models, Karasawa's model takes the scattering phenomenon into account, but it is not suitable for path loss calculations. Therefore, the Physical Optics model was developed for path loss predictions, using the findings of Karasawa. The Physical Optics model divides the sea surface into small tiles and computes the scattering from each tile individually. Hence, it was possible to simulate the influence of the scattering phenomenon on the path loss by summing up over all tiles. The ITU model, as well as the Round Earth Loss model consider a curved earth. The Physical Optics model uses a plane earth, to reduce the computational complexity for scattering.
To obtain the propagation characteristics over sea, the Mobile Radio Transmission Group of the Institute of Communications and Navigation of the German Aerospace Center conducted a broadband measurement campaign. The measurements were performed in the Baltic Sea in March 2014, where the transmitter was on a ship and the receiver was located on two different land sites. The measured data consisted of snapshots of the channel impulse response. The data were processed and compared to the three models in terms of path loss.
Since no maritime channel model is available for the simulation of terrestrial broadband communication and navigation services, a novel wideband channel model was proposed in a further step, based on the Physical Optics model. This new model uses a randomly generated, irregular sea surface, to allow a more realistic simulation of the electromagnetic wave propagation over sea. With the help of the wideband model, it was possible to simulate channel impulse responses. Out of the channel impulse responses, the power delay profile and the corresponding time dispersion parameters, i.e. the mean delay and the RMS delay spread, were computed. The results were then compared to the broadband measurements.

Regarding path loss predictions, the three models deliver very different results. The Recommendation ITU-R P.1546-2 accounts for the free-space loss and losses due to reflections and diffraction, but it does not separate the line-of-sight signal and the signal reflections. The output of this model is the mean power, which is exceeded at 50 %, 10 % and 1 % of time at a certain distance. Hence, the ITU model is only suitable for rough path loss predictions and does not take interferences between the different signal components into account.
The Round Earth Loss model is based on the two-ray propagation over a curved earth, where the line-of-sight component and the specular reflected component are separated. Therefore, this model is able to predict signal fading, due to constructive and destructive interferences between the signal components. The Round Earth Loss model provides a good match to the measurements at distances between transmitter and receiver above $\sim$2 km. However, it is not able to account for fast and random power fluctuations of the measurements, mainly caused by the diffuse scattering from the sea surface.
In contrast to the ITU model and the Round Earth Loss model, the Physical Optics model delivers good agreement with the measurement data over the entire distance range. On the one hand, it predicts the signal fading for large distances, where the interferences between line-of-sight signal and the specular reflection are dominant. On the other hand it is also able to account for the fast power variations, due to the scattering phenomenon. Particularly, at short distances, the diffuse scattering component is more significant than the specularly reflected component. Therefore, the Physical Optics model is more suitable for path loss predictions over sea, compared to the ITU model and the Round Earth Loss model.
The proposed wideband channel model, which is based on the principle of the Physical Optics model, also shows a very good agreement with the measurement data. The simulations of the channel impulse responses were performed for three different distances between transmitter and receiver, i.e. 3 km, 4 km and 5 km. Based on the channel impulse responses, the power delay profiles and the corresponding wideband characteristics, i.e. mean delay and RMS delay spread, were computed. The predicted power delay profiles and wideband characteristics fit very well to the measurement data. As conclusion it can be said, that the investigated scattering phenomenon, caused by the roughness of the sea surface, has an increasing impact on the received signal with decreasing distances between transmitter and receiver.

In the future, a novel channel model for maritime communication and navigation applications is going to be proposed. This model will consist of three major parts, which account for different aspects of the maritime radio propagation channel. The three model parts can be summarized as following:

1. modeling of the scattering phenomenon, caused by the roughness of the sea surface,
2. modeling of reflections from the land, i.e. from the harbor and coastal regions,
3. and modeling of reflections caused by the vessel itself.

The first part was investigated in the course of this work in terms of path loss computations and wideband simulations.
Further improvements and possible future work, considering the first part, are

- assuming a curved earth for the PO model and the wideband channel model,
- considering a change in the ship antenna gain, according to the ship movement,
- taking the influence of wind speed and wind direction on the shape of the sea surface into account.

The investigated scattering phenomenon due to the roughness of the sea surface has an influence on the received power, which is not negligible, particularly for short distances between transmitter and receiver. Therefore, the impact of scattering has to be considered for the design and the development of future maritime broadband communication systems. The proposal of the wideband channel model is a first step towards this goal and provides a starting point for further investigations of the maritime radio channel.

List of Abbreviations

CEPT European Conference of Postal and Telecommunications Administration

CIR Channel Impulse Response

DLR German Aerospace Center

EGM96 Earth Gravitational Model 1996

EM Electromagnetic

ERP Equivalent Radiated Power

ETSI European Telecommunications Standards Institute

FFZ First Fresnel Zone

FSL Free Space Loss

GPS Global Positioning System

IDFT Inverse Discrete Fourier Transform

ITU International Telecommunication Union

ITU-R ITU Radiocommunication Sector

LOS Line Of Sight

MPC Multipath Component

PDF Probability Density Function

PDP Power Delay Profile

PO Physical Optics

PPP Precise Point Position

RCS Radar Cross Section

RMS Root Mean Square

REL Round Earth Loss

RINEX Receiver Independent Exchange Format

RX Receiver

SISO Single-Input Single-Output

SIMO Single-Input Multiple-Output

SNR Signal-to-Noise Ratio

TX Transmitter

VHF Very High Frequency

WGS84 World Geodetic System 1984

WSV German Federal Waterways and Shipping Administration

Bibliography

[1] W. Wang, R. Raulefs, T. Jost, A. Dammann, C. Gentner, and S. Zhang, "Ship-to-Land Broadband Channel Measurement Campaign at 5.2 GHz," *OCEANS'14 MTS/IEEE St. John's*, September 2014.

[2] Rec. ITU-R P.1546-2, *Method for point-to-area predictions for terrestrial services in the frequency range 30 MHz to 3000 MHz*, ITU, 2005.

[3] K. Yang, A. F. Molisch, T. Ekman, and T. Roste, "A Deterministic Round Earth Loss Model for Open-Sea Radio Propagation," *Vehicular Technology Conference (VTC Spring)*, pp. 1–5, June 2013.

[4] Y. Karasawa and T. Shiokawa, "Characteristics of L-Band Multipath Fading due to Sea Surface Reflection," *IEEE Transactions on Antennas and Propagation*, vol. 32, no. 6, pp. 618–623, June 1984.

[5] F. Ulaby and D. Long, *Microwave Radar and Radiometric Remote Sensing.* The University of Michigan Press, 2014.

[6] P. Beckmann and A. Spizzichino, *The Scattering of Electromagnetic Wave from Random Rough Surfaces.* Artech House, Norwood, MA, 1987.

[7] F. Ulaby, R. Moore, and A. Fung, *Microwave Remote Sensing: Active and Passive.* Artech House, Norwood, MA, 1982, vol. 2.

[8] T. Rappaport, *Wireless Communications: Principles and Practice*, 2nd ed. Pearson Education Ltd., 2002.

[9] A. Fung, W. Liu, K. Chen, and M. Tsay, "An Improved IEM Model for Bistatic Scattering from Rough Surfaces," *Journal of Electromagn. Waves and Appl.*, vol. 16, no. 5, pp. 689–702, 2002.

[10] B. Smith, "Geometrical Shadowing of a Random Rough Surface," *IEEE Transactions on Antennas and Propagation*, vol. 15, no. 5, pp. 668–671, September 1967.

[11] Wei Wang, *Channel Measurement and Modeling for Mobile Radio Based Positioning.* Shaker Verlag, 2014.

[12] 2015. [Online]. Available: http://www.channelsounder.de/

[13] D. Hauser et al., "SWIMSAT: A Real-Aperture Radar to Measure Directional Spectra of Ocean Waves from Space (Main Characteristics and Performance Simulation)," *Journal of Atmospheric and Oceanic Technology*, pp. 421–437, 03 2001.

[14] K. Bullington, "Radio Propagation at Frequencies Above 30 Megacycles," *Proceedings of the I.R.E.-Waves and Electrons Section*, pp. 1122–1136, October 1947.

[15] A. Fung, *Microwave Scattering and Emission Models and Their Applications.* Artech House, Norwood, MA, 1994.

Appendix A: Diffraction loss of the REL model

The diffraction loss L used in the REL model ([3]) is based on the findings in [14]. For the derivation of L we will refer to the definitions in Section 2.2.3 in combination with Figure 2.5.
The total horizontal distance d between TX and RX over the spherical earth is the sum of d_1, d_2 and d_3. Each of these parts causes a corresponding loss L_1, L_2 and L_3, which are defined in decibels (dB) as

$$L_1 = 20\log_{10}\left(\frac{N_1}{\sqrt{5.656\pi\zeta_1}}\right), \tag{A.1}$$

$$L_2 = 20\log_{10}(N_2), \tag{A.2}$$

and

$$L_3 = 0.0086\zeta_3^2 + 0.2063\zeta_3^2 + 11.0997\zeta_3 - 0.8934, \tag{A.3}$$

where

$$20\log_{10}(N_n) = -0.5 + 35\log_{10}(\zeta_n) + 10\log_{10} F_{s,n} \qquad (\text{n} = 1{,}2), \tag{A.4}$$

$$\zeta_n = \left(\frac{2\pi d_n}{\lambda}\right)\left(\frac{2\pi k_e r_e}{\lambda}\right)^{-\frac{2}{3}} \qquad (\text{n} = 1{,}2{,}3), \tag{A.5}$$

and

$$20\log_{10}(F_{s,n}) = -0.048\zeta_n + 1.0875\zeta_n + 4.0782\zeta_n - 0.8806. \tag{A.6}$$

The losses L_1 and L_2 are negative quantities, whereas the loss L_3 can be positive or negative. The total diffraction loss for the path loss calculation as in Eq. (2.51) is given by

$$L = \begin{cases} L_1 + L_2 - |L_3| & \text{if } d \geq d_1 + d_2, \\ L_1 + L_2 + |L_3| & \text{if } D_{06} < d < d_1 + d_2, \\ 0 & \text{if d} < D_{06}, \end{cases} \tag{A.7}$$

where the quantity D_{06} is defined in [2] as the *0.6 Fresnel clearance path length* (the path length where 60 % of the first Fresnel zone (FFZ) is cleared, regarding a curved earth). This quantity depends on the frequency f and the heights of the transmitter h_1 and the receiver h_2. It is given by

$$D_{06} = \frac{D_f D_h}{D_f + D_h}, \tag{A.8}$$

with

$$D_f = 0.0000389 f h_1 h_2 \tag{A.9}$$

as the frequency-dependent term and the term D_h is given by

$$D_h = 4.1\left(\sqrt{h_1} + \sqrt{h_2}\right) \tag{A.10}$$

as an asymptotic term depending on the horizon distances from TX and RX. In the definition f is in MHz, the heights h_1 and h_2 are in m above ground and the results for D_{06}, D_f and D_h are given in km.
It is worth to note, that according to Eq. (A.7), L depends on the total horizontal distance d between TX and RX. We can distinguish between three different cases:

1. For $d \geq d_1 + d_2$ the total diffraction loss L rapidly increases, because the LOS path is beyond the horizon. In this case $d_3 \geq 0$ and the corresponding diffraction loss L_3 is negative.

2. When $D_{06} < d < d_1 + d_2$ a direct LOS path is present between TX and RX. The horizontal distance d_3 becomes *mathematically negative* and therefore, the corresponding diffraction loss L_3 is assumed to be *positive*.

3. For the case when $d < D_{06}$, the diffraction effect is not present and L is set to zero.

In order to avoid jumps in the total diffraction loss L, the component L_3 has to be zero at the transition between case 1 and 2, i.e., $d = d_1 + d_2$. For the transition between case 2 and 3 (i.e., $d = D_{06}$), the total diffraction loss L has to be zero, which means $|L_3| = |L_1| + |L_2|$.

Appendix B: Derivation of the scattering coefficient used by Karasawa's model

For the derivation of the bistatic scattering coefficient σ_0 we will refer to the coordinate system and the corresponding quantities shown in Figure 2.9. The term *bistatic* means, that the transmitter and the receiver are at different positions (in contrast to the classical monostatic radar scenario, where the locations are the same for both transmitter and receiver). Since we focus on bistatic scattering throughout this thesis, the term *bistatic* is omitted in the following. In general the scattering coefficient σ_0 describes the ratio between scattered and incident power at the scattering position (i.e., on the rough surface). It is defined in [15] (page 3) as

$$\sigma_0^{qp}(\Theta_i, \Theta_s, \Phi_s) = \frac{\langle \sigma^{qp} \rangle}{A} = \frac{4\pi R^2}{A} \frac{\langle |E_s^q|^2 \rangle}{|E_i^p|^2}, \tag{B.11}$$

where σ is the RCS given in m^2, R is the distance between receiver and scattering position on the surface, A is the considered area on the sea surface. The subscripts i and s denote the incident and scattered wave strength on the sea surface. The superscripts q and p denote the polarizations of the scattered and incident wave, respectively. Due to the fact, that we assume vertical polarization for transmit and receive antennas (i.e., q and p are the same), these superscripts are omitted throughout this thesis. Furthermore σ_0 depends on the angles Θ_i, Θ_s and Φ_s defined in Figure 2.9. According to the definition in Eq. (B.11) the RCS σ is normalized by the scattering area A. Therefore σ_0 is also denoted as *radar cross section per unit area* or *normalized RCS* and is a dimensionless quantity.
However, the result for σ_0 used in [4] is based on the findings in [6]. In this literature the scattering coefficient is defined slightly different as the ratio between electric field strengths at the receiver position ([6], page 22 et seq.) and is given by

$$\rho = \frac{E_s}{E_{s0}}, \tag{B.12}$$

where E_s is the received electric field strength scattered from a random rough surface for specific incident angle Θ_i, scattered angle Θ_s and azimuth angle Φ_s. E_{s0} is the field strength at the receiver for the same angles, but for a smooth and perfectly conducting surface (i.e., for specular reflection). It is defined as

$$E_{s0} = \frac{2jk \exp(jkR)\, XY \cos\Theta_i}{\pi R}, \tag{B.13}$$

where k is the wavenumber according to (2.24), R is the distance between the scattering point and the receiver and Θ_i is the angle of incidence. The quantities X and Y denote the dimensions of the scattering surface in x- and y-direction, respectively, where the surface extends from $-X$ to X and from $-Y$ to Y. Therefore, the considered area A is

$$A = 4XY. \tag{B.14}$$

For the derivation of σ_0 we start from Eq. (B.12) and we will finally end up with an expression for σ_0, which corresponds to the definition in (B.11).
According to Eq. (B.12) ρ is a complex quantity, since it is the ratio between two field strengths, which in general have different phases. Furthermore, in order to ensure energy conservation, $|\rho|$ always has to be smaller than or equal 1 (i.e., $|\rho| \leq 1$).
The mean square of $|\rho| = \sqrt{\rho\rho^*}$ is given as

$$\langle \rho\rho^* \rangle = \langle |\rho|^2 \rangle = \left\langle \left| \frac{E_s}{E_{s0}} \right|^2 \right\rangle, \tag{B.15}$$

and is proportional to the mean scattered power. It may also be written as

$$\langle \rho\rho^* \rangle = \langle \rho \rangle \langle \rho^* \rangle + D\{\rho\}, \tag{B.16}$$

where the first term on the right hand side denotes the mean value of $\langle \rho\rho^* \rangle$ and the second term its variance $D\{\rho\}$. This variance can also be expressed in terms of the variance of the scattered field $D\{E_s\}$ as

$$D\{\rho\} = \frac{1}{|E_{s0}|^2} D\{E_s\}. \tag{B.17}$$

Due to the fact, that $D\{E_s\}$ is related to the diffusely scattered power, we examine Eq. (B.17) in more detail. The variance of ρ for a two-dimensional rough surface, assuming a Gaussian surface height distribution and a Gaussian surface correlation function (see Eq. (2.2) and (2.10)), is defined in [6] (page 86) as

$$D\{\rho\} = \frac{\pi l_0^2 F^2 \exp(-g)}{A} \sum_{m=1}^{\infty} \frac{g^m}{m!m} \exp(-\frac{v_{xy}^2 l_0^2}{4m}), \tag{B.18}$$

where

$$F = \frac{1 + \cos\Theta_i \cos\Theta_s - \sin\Theta_i \sin\Theta_s \cos\Phi_s}{\cos\Theta_i (\cos\Theta_i + \cos\Theta_s)}, \tag{B.19}$$

and

$$\sqrt{g} = u = kh_0(\cos\Theta_i + \cos\Theta_s) \tag{B.20}$$

is the roughness parameter defined in Section 2.2.2 (Eq. (2.28)) and l_0 is the sea surface correlation length (see Section 2.1.1.2). The quantity v_{xy} is given by

$$v_{xy} = \sqrt{v_x^2 + v_y^2}, \tag{B.21}$$

with

$$v_x = k\left(\sin\Theta_i - \sin\Theta_s \cos\Phi_s\right), \tag{B.22}$$

and

$$v_y = -k\left(\sin\Theta_s \sin\Phi_s\right) \tag{B.23}$$

Rearranging Eq. (B.17) and using the expressions for E_{s0} and $D\{\rho\}$ defined in (B.13) and (B.18), we can write the variance of the scattered field $D\{E_s\}$ as

$$\begin{aligned} D\{E_s\} &= |E_{s0}|^2 D\{\rho\} \\ &= \left|\frac{2jk\exp(jkR)\,XY\cos\Theta_i}{\pi R}\right|^2 \frac{\pi l_0^2 F^2\exp(-g)}{A}\sum_{m=1}^{\infty}\frac{g^m}{m!m}\exp\left(-\frac{v_{xy}^2 l_0^2}{4m}\right) \\ &= \frac{4k^2(XY)^2\cos^2\Theta_i}{\pi^2 R^2}\frac{\pi l_0^2 F^2\exp(-g)}{4XY}\sum_{m=1}^{\infty}\frac{g^m}{m!m}\exp\left(-\frac{v_{xy}^2 l_0^2}{4m}\right) \\ &= \frac{\pi l_0^2\cos^2\Theta_i F^2\exp(-g)}{\lambda^2 R^2}A\sum_{m=1}^{\infty}\frac{g^m}{m!m}\exp\left(-\frac{v_{xy}^2 l_0^2}{4m}\right), \end{aligned} \tag{B.24}$$

which is equivalent to Karasawa's result for the variance of the scattered field and therefore to the mean diffusely scattered (or incoherent) power ([4]). Furthermore, this expression for $D\{E_s\}$ is proportional to the RCS σ. The RCS per unit area σ_0 is obtained by multiplying Eq. (B.24) with the normalization factor $4\pi R^2/A$ as shown in (B.11):

$$\begin{aligned} \sigma_0 &= \frac{4\pi R^2}{A}D\{E_s\} \\ &= \frac{4\pi R^2}{A}\frac{\pi l_0^2\cos^2\Theta_i F^2\exp(-g)}{\lambda^2 R^2}A\sum_{m=1}^{\infty}\frac{g^m}{m!m}\exp\left(-\frac{v_{xy}^2 l_0^2}{4m}\right) \\ &= \frac{4\pi^2\cos^2\Theta_i l_0^2 F^2\exp(-g)}{\lambda^2}\frac{4h_0^2}{4h_0^2}\sum_{m=1}^{\infty}\frac{g^m}{m!m}\exp\left(-\frac{v_{xy}^2 l_0^2}{4m}\right) \\ &= \frac{k^2 h_0^2 4\cos^2\Theta_i l_0^2}{4h_0^2}F^2\exp(-g)\sum_{m=1}^{\infty}\frac{g^m}{m!m}\exp\left(-\frac{v_{xy}^2 l_0^2}{4m}\right) \\ &= \frac{g}{2\beta_0^2}F^2\exp(-g)\sum_{m=1}^{\infty}\frac{g^m}{m!m}\exp\left(-\frac{v_{xy}^2 l_0^2}{4m}\right) \\ &= \frac{u^2}{2\beta_0^2}F^2\exp(-u^2)\sum_{m=1}^{\infty}\frac{u^{2m}}{m!m}\exp\left(-\frac{v_{xy}^2 l_0^2}{4m}\right), \end{aligned} \tag{B.25}$$

where β_0 is defined in (2.17) and u denotes the roughness parameter under the assumption that incident and scattered angles are equal (i.e., $\Theta_i = \Theta_s$). This result can be further simplified by rearranging the exponential term under the sum in the following way:

$$\begin{aligned} \sigma_0 &= \frac{u^2}{2\beta_0^2}F^2\exp(-u^2)\sum_{m=1}^{\infty}\frac{u^{2m}}{m!m}\exp\left(-\frac{v_{xy}^2 l_0^2}{4m}\right) \\ &= \frac{u^2}{2\beta_0^2}F^2\exp(-u^2)\sum_{m=1}^{\infty}\frac{u^{2m}}{m!m}\exp\left(-\frac{\tan^2\gamma v_z^2 l_0^2}{4m}\frac{h_0^2}{h_0^2}\right) \\ &= \frac{u^2}{2\beta_0^2}F^2\exp(-u^2)\sum_{m=1}^{\infty}\frac{u^{2m}}{m!m}\exp\left(-\frac{\tan^2\gamma u^2}{2m\beta_0^2}\right) \\ &= \frac{u^2}{2\beta_0^2}F^2\sum_{m=1}^{\infty}\frac{u^{2m}}{m!m}\exp\left(-u^2\left[1+\frac{\tan^2\gamma}{2m\beta_0^2}\right]\right), \end{aligned} \tag{B.26}$$

where v_{xy}, given in Eq. (B.21), is written as

$$v_{xy} = \sqrt{v_x^2 + v_y^2} = \tan\gamma v_z, \tag{B.27}$$

with the angle γ defined in Section 2.3.3 (Eq. (2.54)) as

$$\gamma = \arctan\left\{\frac{\sqrt{\sin^2\Theta_i - 2\sin\Theta_i\sin\Theta_s\cos\Phi_s + \sin^2\Theta_s}}{\cos\Theta_i + \cos\Theta_s}\right\}. \tag{B.28}$$

The roughness parameter u is expressed in terms of v_z as

$$u = kh_0\left(\cos\Theta_i + \cos\Theta_s\right) = kv_z, \tag{B.29}$$

with

$$v_z = k(\cos\Theta_i + \cos\Theta_s). \tag{B.30}$$

Under the assumption, that incident and scattered angle are equal, the factor F is related to γ by

$$F = \frac{1 + \cos\Theta_i\cos\Theta_s - \sin\Theta_i\sin\Theta_s\cos\Phi_s}{\cos\Theta_i(\cos\Theta_i + \cos\Theta_s)} = \sec^2\gamma, \tag{B.31}$$

where

$$\sec\gamma = \frac{v}{v_z}, \tag{B.32}$$

and

$$v = \|\vec{v}\| = \left\|(v_x, v_y, v_z)^T\right\| = \left\|\vec{k_i} - \vec{k_s}\right\| = \sqrt{v_x^2 + v_y^2 + v_z^2}. \tag{B.33}$$

Using Eq. (B.31), we obtain the final result for the scattering coefficient σ_0 as

$$\sigma_0 = \frac{u^2}{2\beta_0^2}\sec^4\gamma\sum_{m=1}^{\infty}\frac{u^{2m}}{m!m}\exp\left(-u^2\left[1 + \frac{\tan^2\gamma}{2m\beta_0^2}\right]\right). \tag{B.34}$$

This result is similar to that in [4]. The only difference in Karasawa's result is the missing factor 2 in combination with β_0^2, because Karasawa's model defines $\beta_0 = 2h_0/l_0$ (in contrast to our assumption that $\beta_0 = \sqrt{2}h_0/l_0$).
As in [4] the roughness parameter is used to distinguish between smooth and rough sea surface and Eq. (B.34) can be simplified depending on u as

$$\sigma_0(\Theta_i, \Theta_s, \Phi_s) = \begin{cases} \frac{u^4}{2\beta_0^2}\sec^4\gamma\exp\left(-u^2\left[1 + \frac{\tan^2\gamma}{2m\beta_0^2}\right]\right)\left|S\Gamma_{rough}\right|^2, & u^2 \ll 1 \text{ (smooth sea)} \\ \frac{1}{2\beta_0^2}\sec^4\gamma\exp\left(-\frac{\tan^2\gamma}{2m\beta_0^2}\right)\left|S\Gamma_{rough}\right|^2, & u^2 \gg 1 \text{ (rough sea)} \end{cases} \tag{B.35}$$

where the shadowing factor S for bistatic scattering according to Eq. (2.39) and the modified Fresnel reflection coefficient for rough surfaces Γ_{rough} defined in Eq. (2.29) are already included to facilitate the usage of σ_0 in Section 2.3.3.

Appendix C: Path loss model results

The simulation results of the ITU model, REL model and PO model for the scenarios

- Wednesday/hotel/upper floor
  - $h_{\mathrm{RX}} = 48.0$ m above MSL
  - estimated $h_{\mathrm{TX,m}} = 6.28m$ above MSL
  - $h_0 = 0.146$ m
  - estimated $\beta_0 = 0.0236$
- Wednesday/hotel/lower floor
  - $h_{\mathrm{RX}} = 32.3$ m above MSL
  - estimated $h_{\mathrm{TX,m}} = 6.32$m above MSL
  - $h_0 = 0.195$ m
  - estimated $\beta_0 = 0.0184$

are presented in this appendix.

ITU model

Figures C.1 and C.2 visualize the ITU model results for the above listed scenarios. For both scenarios, the predictions are too high for the different percentage times, e.g. the red line is not exceed at 50 % of time. The ITU model does not account for the power variations, caused by interference between direct, specularly reflected and scattered waves.

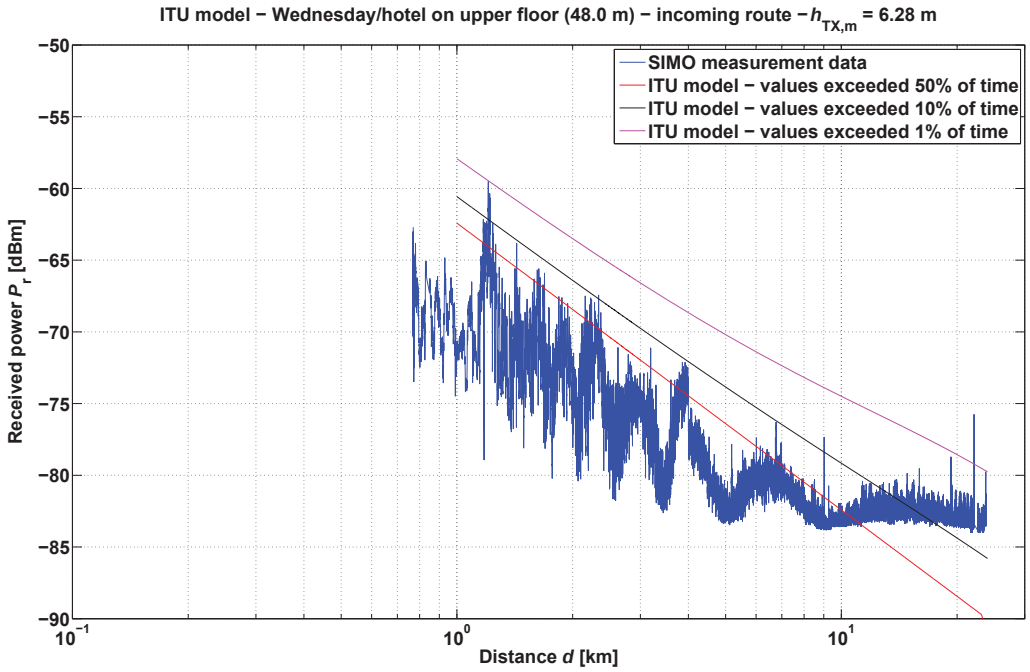

Figure C.1: ITU model results for hotel/upper floor

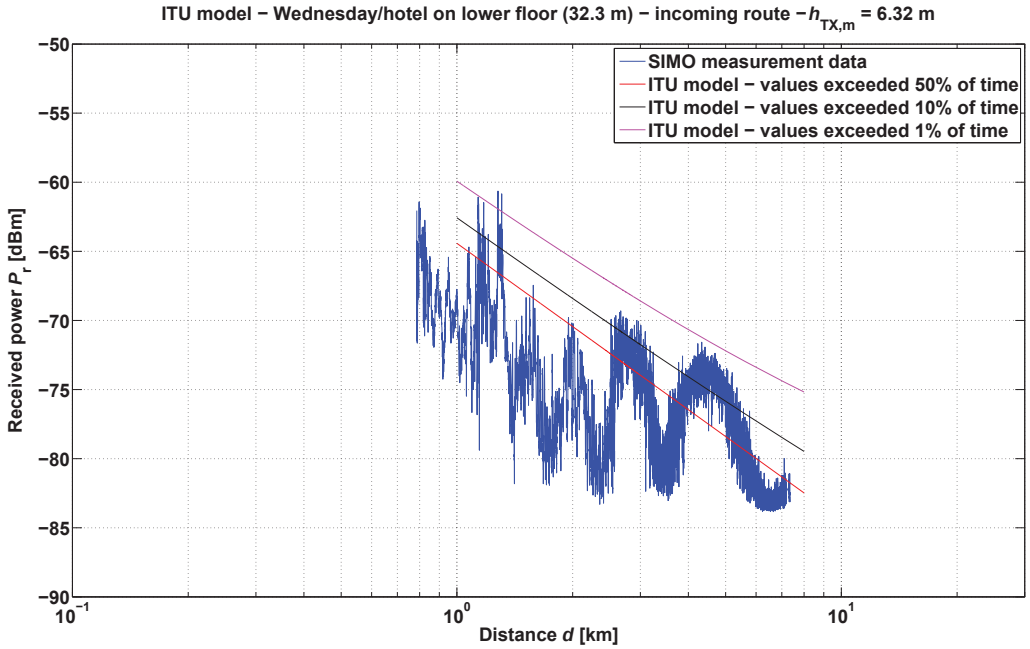

Figure C.2: ITU model results for hotel/lower floor

REL model

Figure C.3 shows the REL model results for Wednesday/hotel/upper floor. The computed power appears too high for distances below 8 km. At 8 km the measurement reaches the noise floor and flattens out. Since noise is not considered for the simulations, the computed power is lower than the measured power, for distances above ∼8 km. The simulated fading depths and periods fit well to the measurements. However, for TX-RX-distances below ∼2 km, the REL model cannot predict the random power fluctuations of the measurement. The fast power variations of the REL model are caused by the changing ship height.

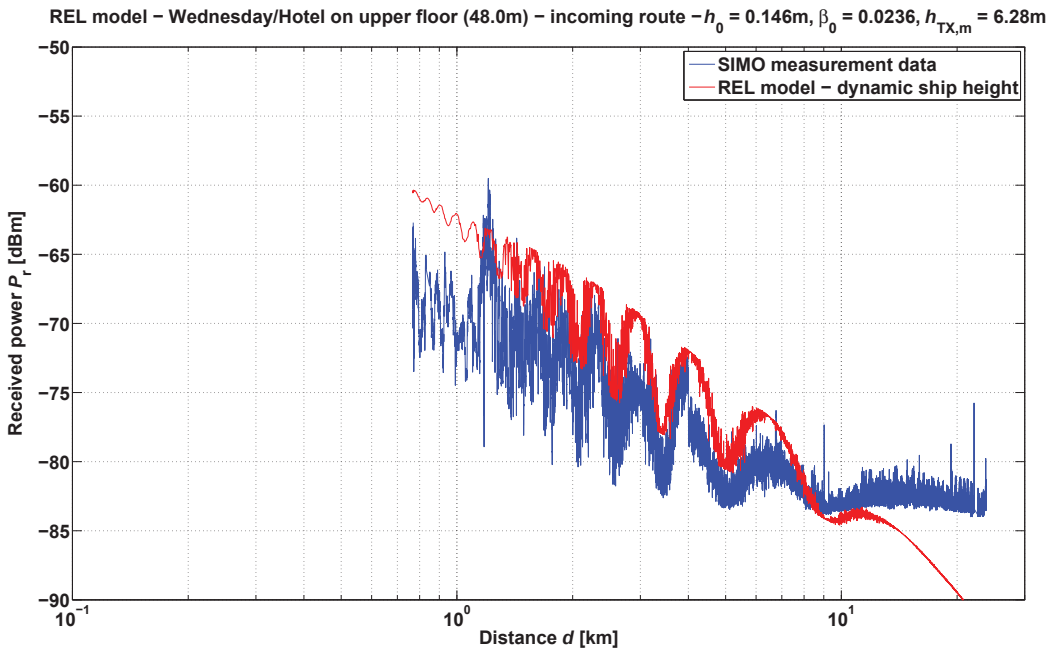

Figure C.3: REL model results for hotel/upper floor

Figure C.4 presents the REL model results for Wednesday/hotel/lower floor. The simulation matches well to the measurement from 3 km to 7 km. Below 3 km the REL model starts to deviate from the measurements and predicts a too high received power. Furthermore, the model does not account for the random signal fluctuations for short distances. The fast power variations simulated by the REL model are again induced by the ship movement.

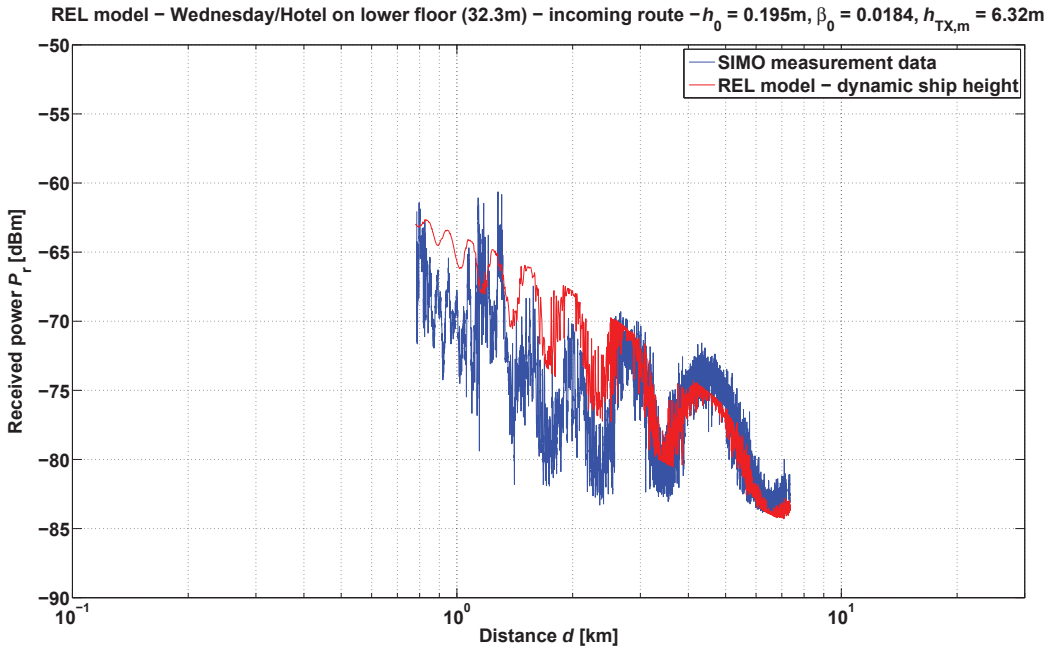

Figure C.4: REL model results for hotel/lower floor

PO model

Figure C.5 shows the PO model results for Wednesday/hotel/upper floor. Similar to the REL model simulations for this scenario in Figure C.3, the predicted power seems to be too high for distances below 8 km. This is caused by leaving out the noise in the model. Apart from that, the PO model delivers very good results. On the one hand, it can predict the fading above 2 km, caused by the interference between LOS component and specular component. On the other hand, the PO model also simulates fast power fluctuations for shorter distances, similar to the measurements. The random power variations are caused by the diffusely scattered component from the sea surface.

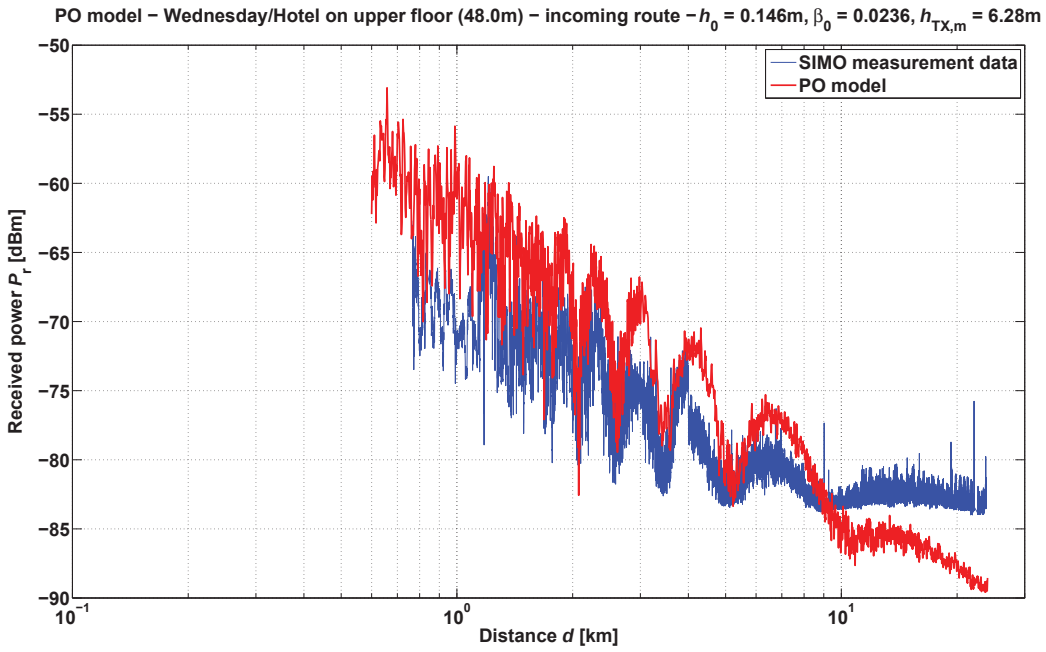

Figure C.5: PO model results for hotel/upper floor

The different components of the PO model for Wednesday/hotel/lower floor are illustrated in Figure C.6. For short distances the coherent component is very low and the LOS signal is mainly superimposed by the fluctuating incoherent component. At 2 km, the coherent component starts to exceed the incoherent component and the characteristic fading for a two-ray propagation starts to appear. With increasing distance, both coherent and incoherent component decrease faster than the LOS signal. Therefore, also the interferences become less significant. The green line represents the received power without diffuse scattering and is similar to the REL model result in Figure C.3.
The PO model uses a static transmitter height, i.e. no height variations were taking into account for the simulation.

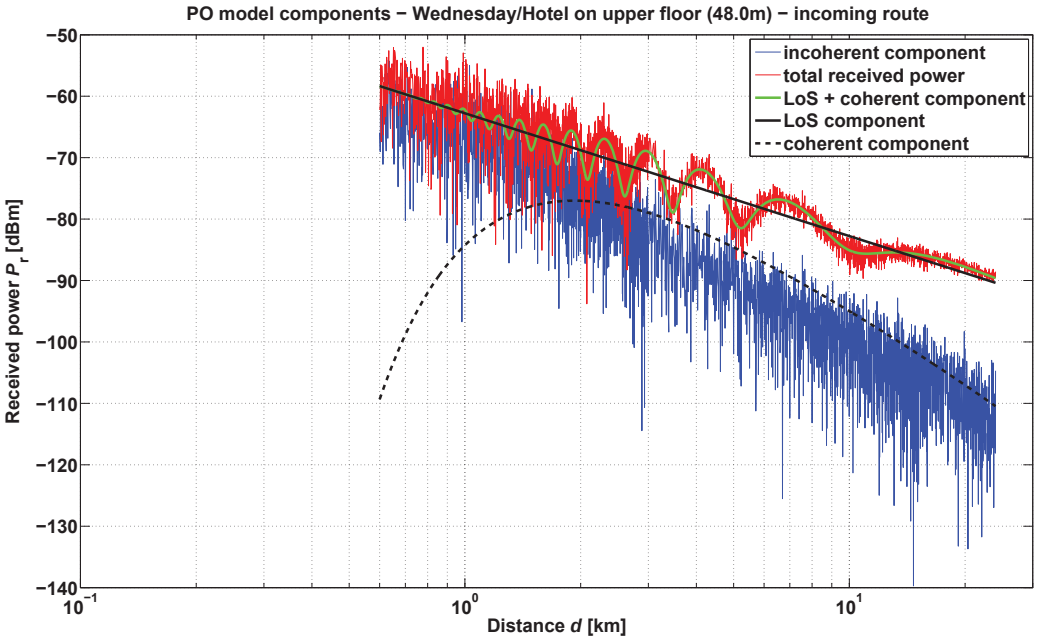

Figure C.6: PO model - separated components for hotel/upper floor

Figure C.7 shows the PO model results for Wednesday/hotel/lower floor. It can be seen, that the results fit very well to the measurements above 2 km, where the interference between LOS signal and specular reflection is dominant. For shorter distances, the computed power is too high, but the predicted random fluctuations fit well to the measurements.

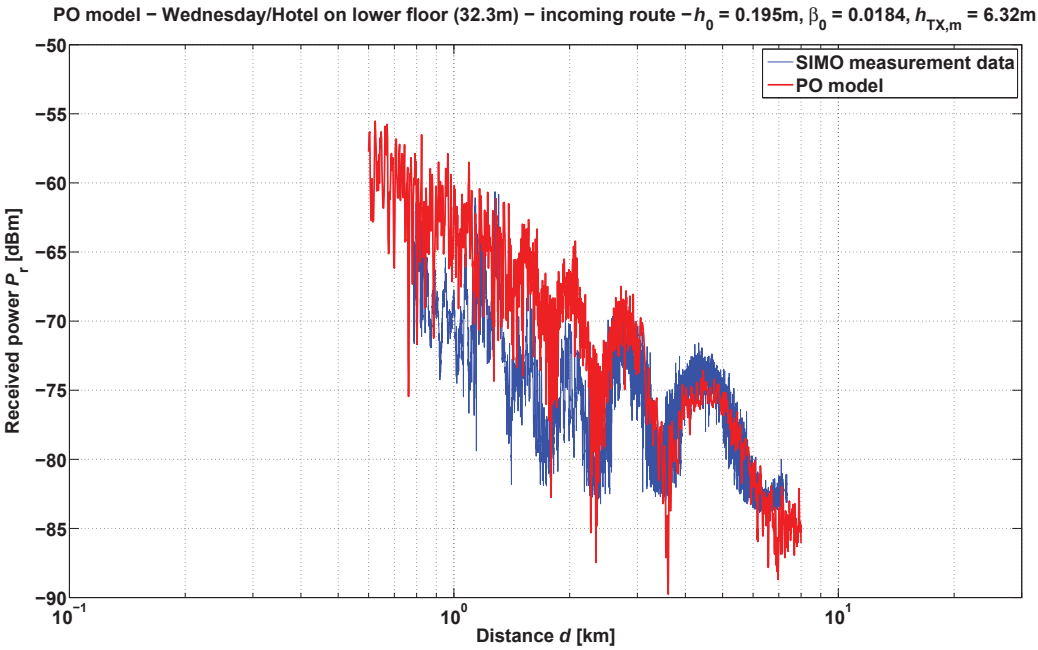

Figure C.7: PO model results for hotel/lower floor

Figure C.8 illustrates the different PO model components for Wednesday/hotel/lower floor. Similar to the results of the previous scenario in Figure C.6, the incoherent component is predominant for distances below 2 km and causes random fluctuations on the LOS signal. Above 2 km the coherent component exceeds the incoherent component. Therefore, the two-ray propagation dominates and the random power variations decrease.

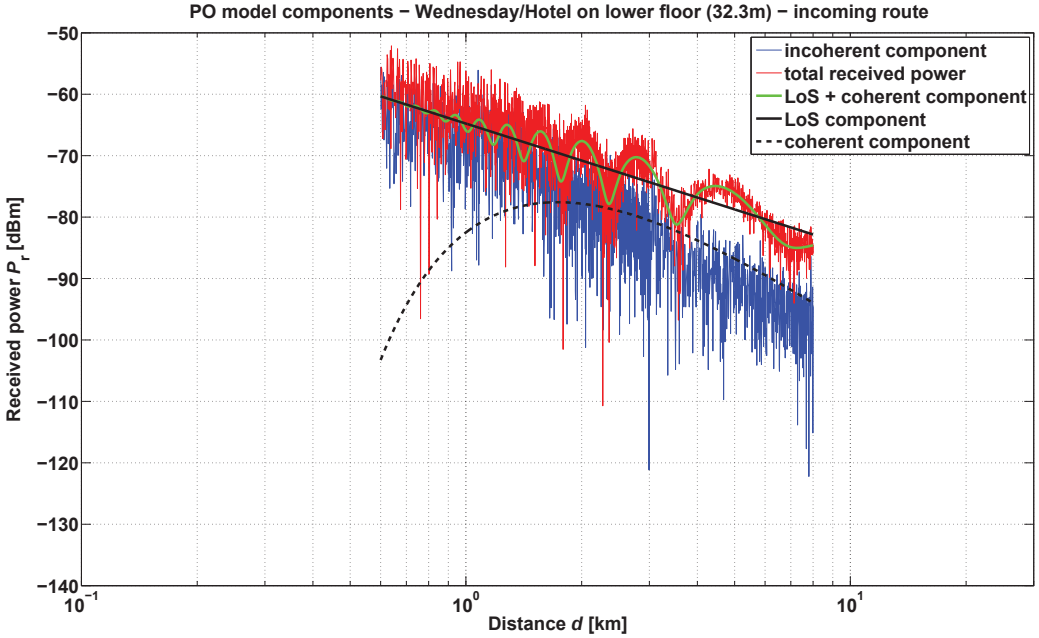

Figure C.8: PO model - separated components for hotel/lower floor

Appendix D: Power delay profiles

This appendix contains the power delay profiles of the measurements and the simulations for Tuesday/lighthouse/upper floor (3 km and 4 km) and Wednesday/hotel/upper and lower floor (3 km, 4 km and 5 km). For all figures the maximum shown delay is 1000 ns.
The calculated values for mean excess delay m_{D} and RMS delay spread σ_{D} for all PDPs in this appendix, are summarized in Tables 5.1 and 5.2, respectively.

Measurement results

Figures D.9 to D.10 show the power delay profiles of the measurements for Tuesday/lighthouse/upper floor for TX-RX-distances of 3 km and 4 km. The shape of the PDPs are approximately equal. The width of the LOS peak is very similar for both distances. No other multipaths arrive within 1000 ns after the LOS signal.

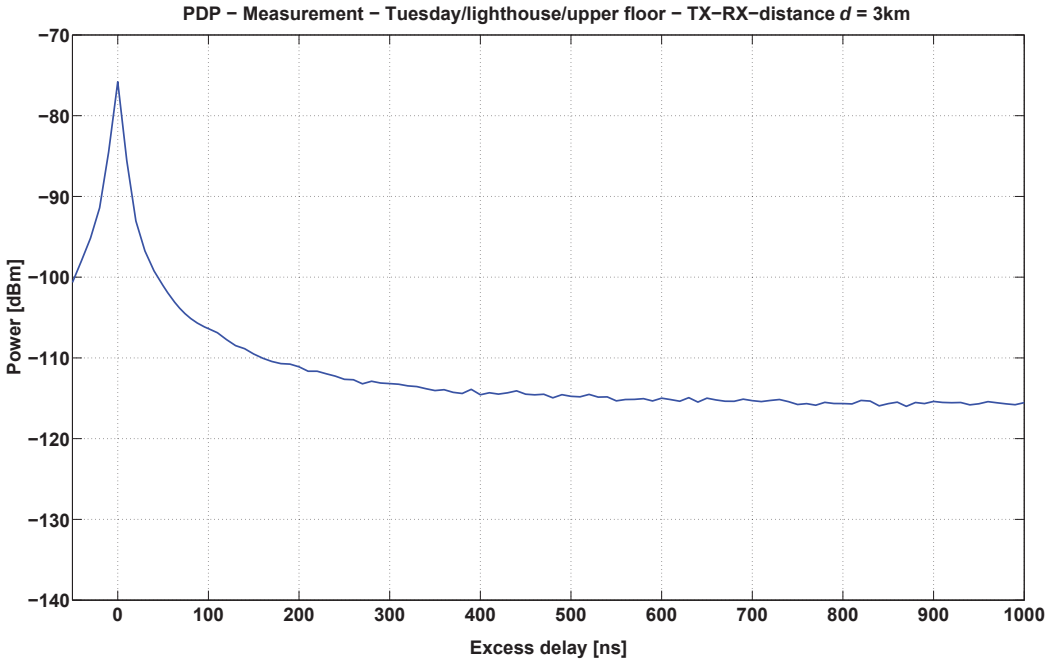

Figure D.9: PDP of the measurement for lighthouse/upper floor for a TX-RX-distance of 3 km

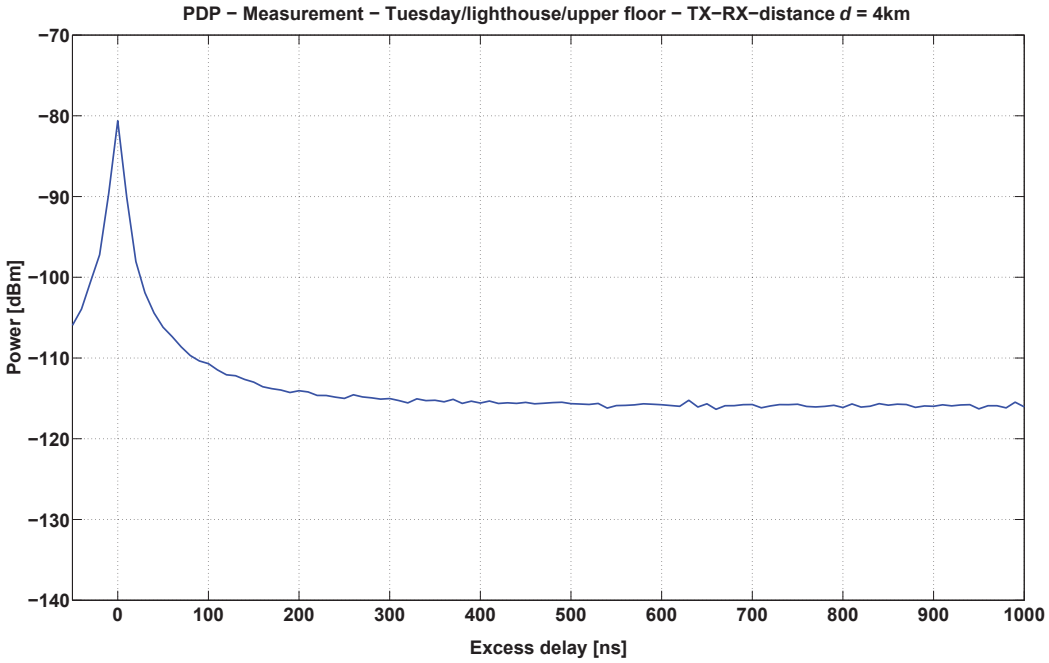

Figure D.10: PDP of the measurement for lighthouse/upper floor for a TX-RX-distance of 4 km

Figures D.11 to D.13 show the power delay profiles of the measurements for Wednesday/hotel/upper floor. We can see, that the LOS signal falls off rapidly. The width of the LOS peak is approximately the same for all distances. It can be observed, that the SNR decreases with increasing distance. Furthermore, no other multipaths occur within 1000 ns after the LOS signal.

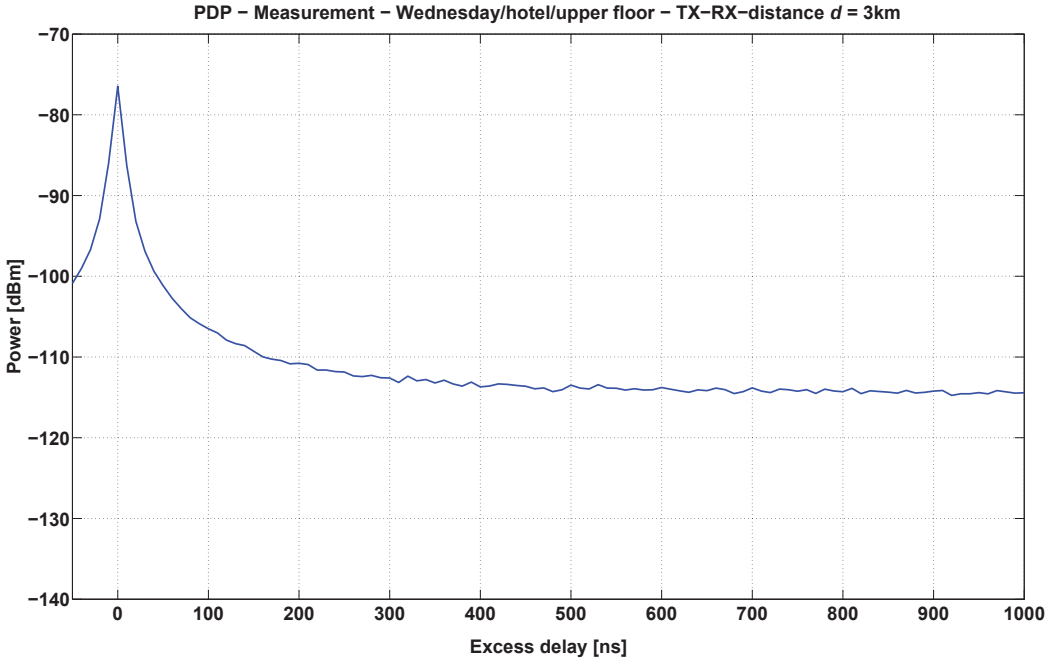

Figure D.11: PDP of the measurement for hotel/upper floor for a TX-RX-distance of 3 km

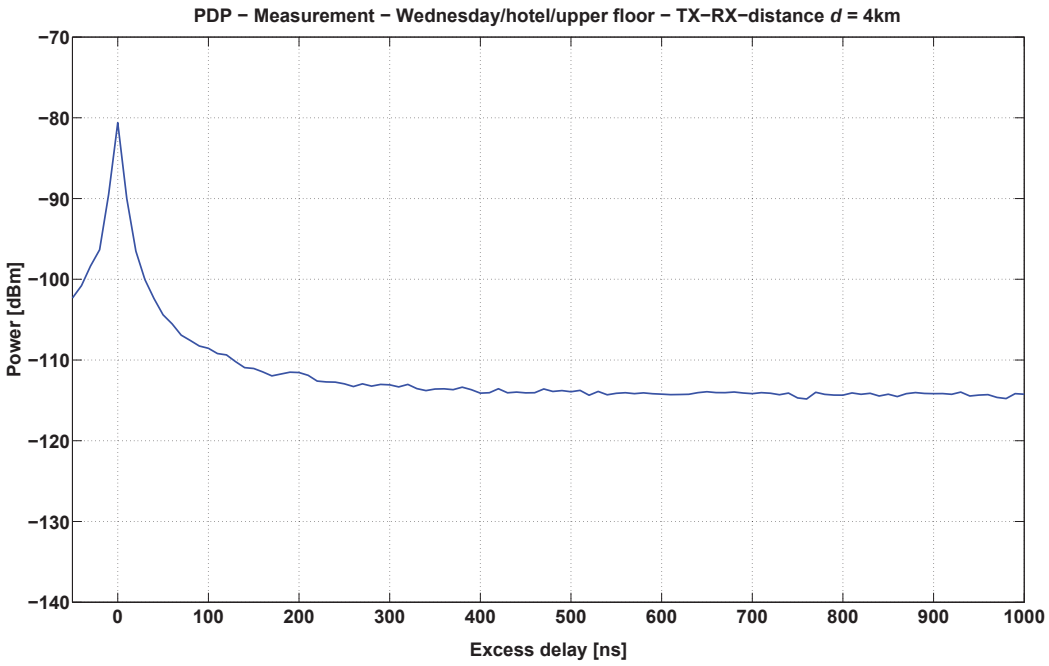

Figure D.12: PDP of the measurement for hotel/upper floor for a TX-RX-distance of 4 km

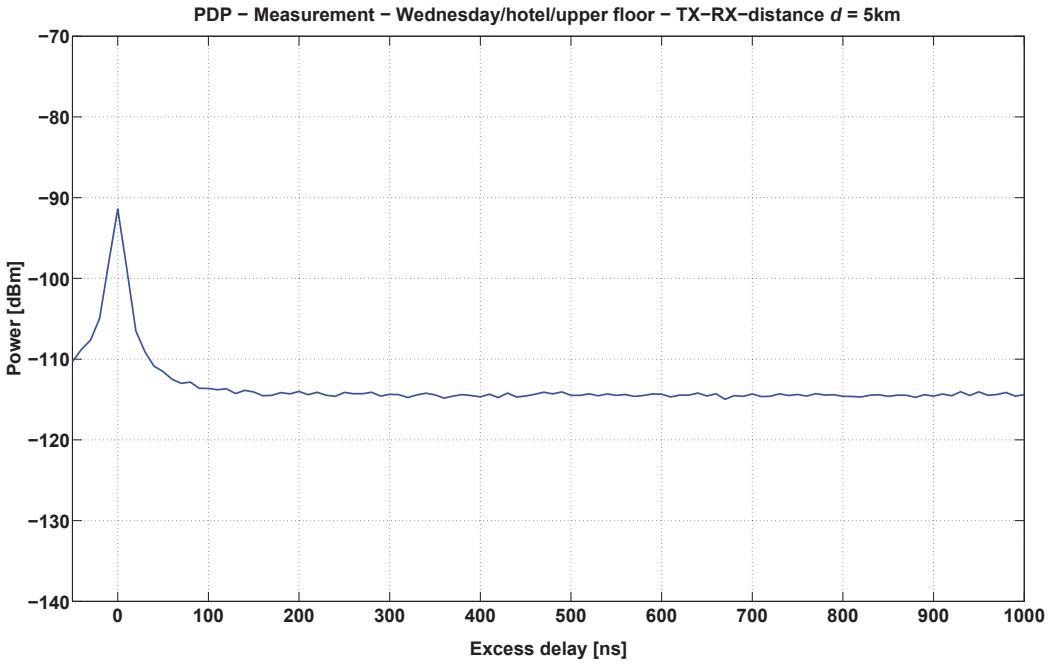

Figure D.13: PDP of the measurement for hotel/upper floor for a TX-RX-distance of 5 km

Figures D.14 to D.16 show the power delay profiles of the measurements for Wednesday/hotel/lower floor. The shape of the PDPs are approximately equal. The width of the LOS peak, as well as the noise floor is very similar for all three distances. No other multipaths arrive within 1000 ns after the LOS signal.

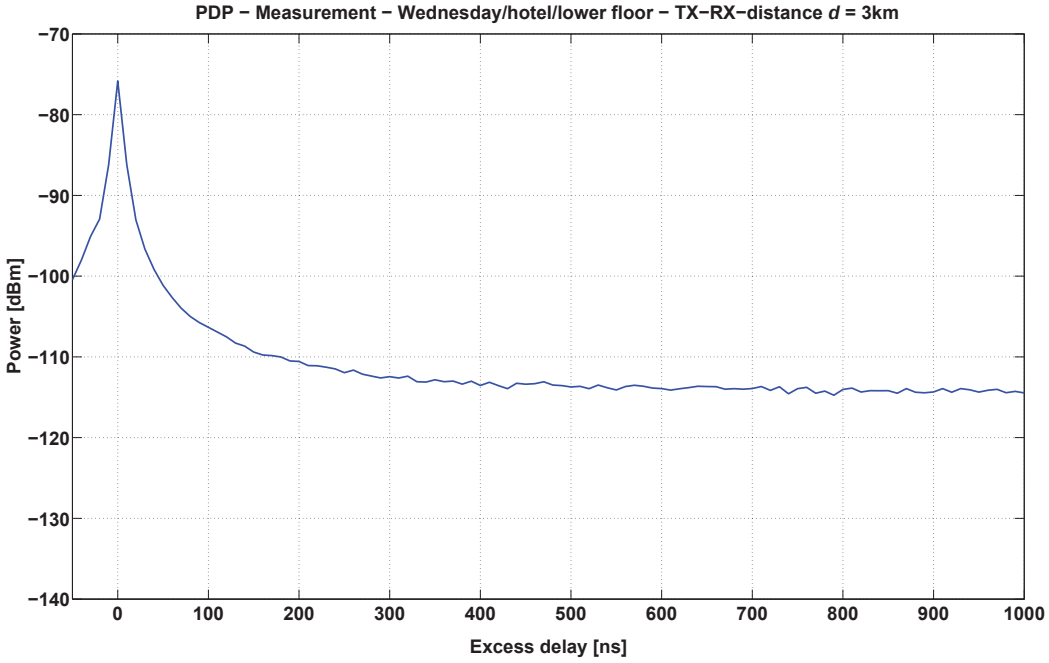

Figure D.14: PDP of the measurement for hotel/lower floor for a TX-RX-distance of 3 km

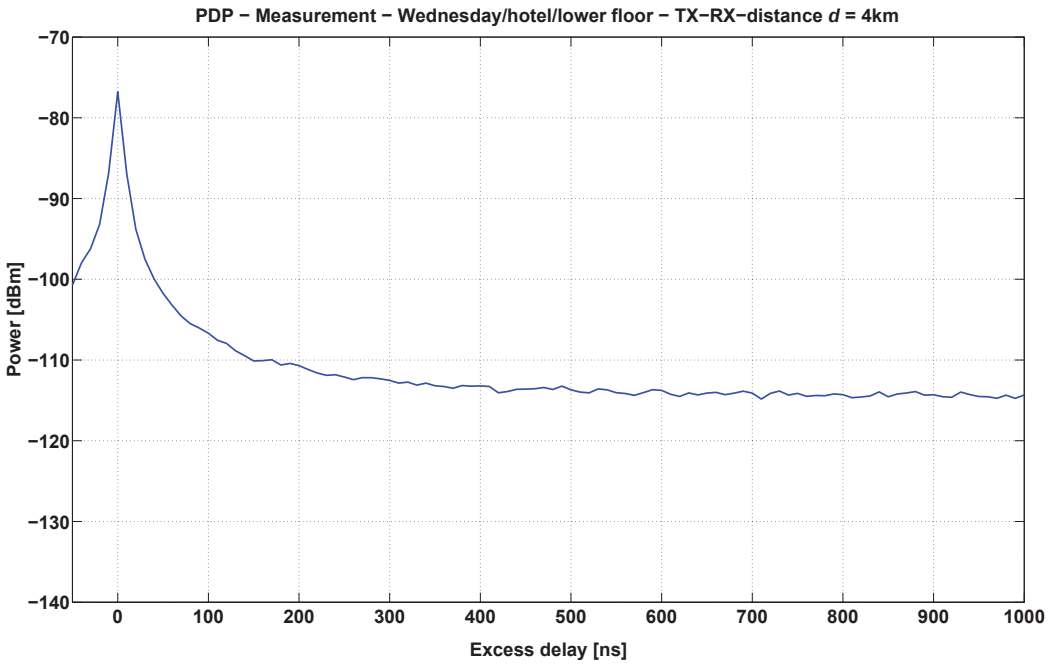

Figure D.15: PDP of the measurement for hotel/lower floor for a TX-RX-distance of 4 km

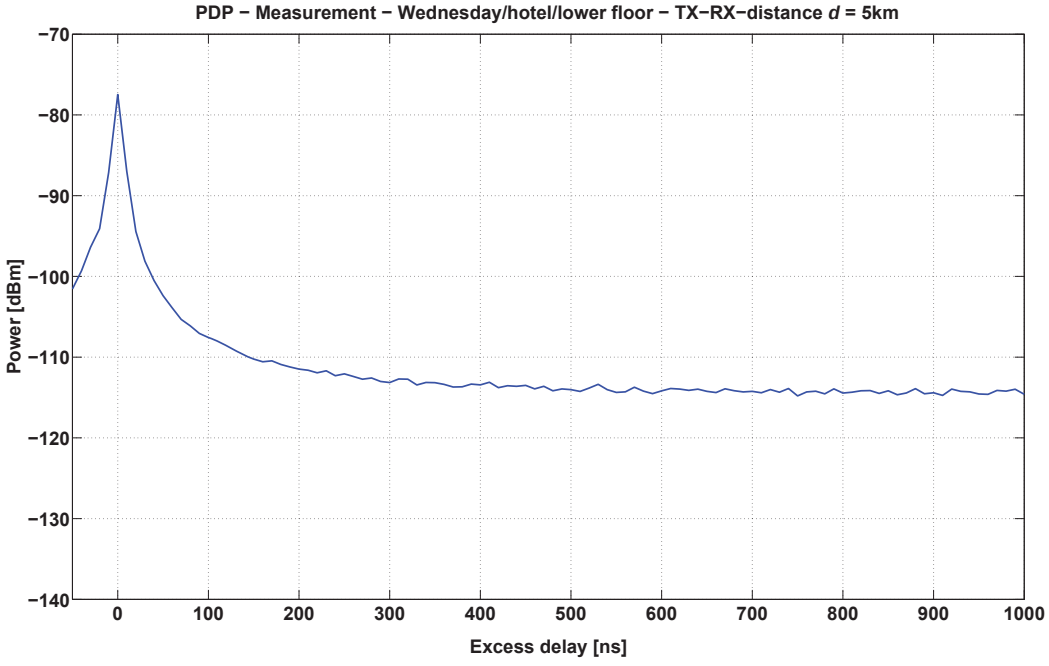

Figure D.16: PDP of the measurement for hotel/lower floor for a TX-RX-distance of 5 km

Wideband model results

The simulation results of the wideband model for the scenarios

- Tuesday/lighthouse/upper floor (3 km and 4 km)
  - $h_{\mathrm{RX}} = 32.9$ m above MSL,
  - estimated $h_{\mathrm{TX},m} = 6.26$m above MSL,
  - RMS surface height of the large scale waves: $h_0 = 0.1347$ m,
  - assumed RMS surface height of the small scale waves: $h_{0,\mathrm{s}} = 0.5$ cm,
  - assumed RMS surface slope of the small scale waves: $\beta_{0,\mathrm{s}} = 0.05$.
- Wednesday/hotel/upper floor
  - $h_{\mathrm{RX}} = 48.0$ m above MSL,
  - estimated $h_{\mathrm{TX},m} = 6.28$m above MSL,
  - RMS surface height of the large scale waves: $h_0 = 0.146$ m,
  - assumed RMS surface height of the small scale waves: $h_{0,\mathrm{s}} = 0.5$ cm,
  - assumed RMS surface slope of the small scale waves: $\beta_{0,\mathrm{s}} = 0.05$.
- Wednesday/hotel/lower floor
  - $h_{\mathrm{RX}} = 32.3$ m above MSL,
  - estimated $h_{\mathrm{TX},m} = 6.32$m above MSL,
  - RMS surface height of the large scale waves: $h_0 = 0.195$ m,
  - assumed RMS surface height of the small scale waves: $h_{0,\mathrm{s}} = 0.5$ cm,
  - assumed RMS surface slope of the small scale waves: $\beta_{0,\mathrm{s}} = 0.05$.

are presented in this section. Figures D.17 and D.18 illustrate the PDPs for Tuesday/lighthouse/upper floor (3 km and 4 km), Figures D.19 to D.21 visualize the PDPs for Wednesday/hotel/upper floor and Figures D.22 to D.24 show the PDPs for Wednesday/hotel/lower floor. The TX-RX-distances for the scenarios Wednesday/hotel upper and lower floor are 3 km, 4 km and 5 km, respectively.

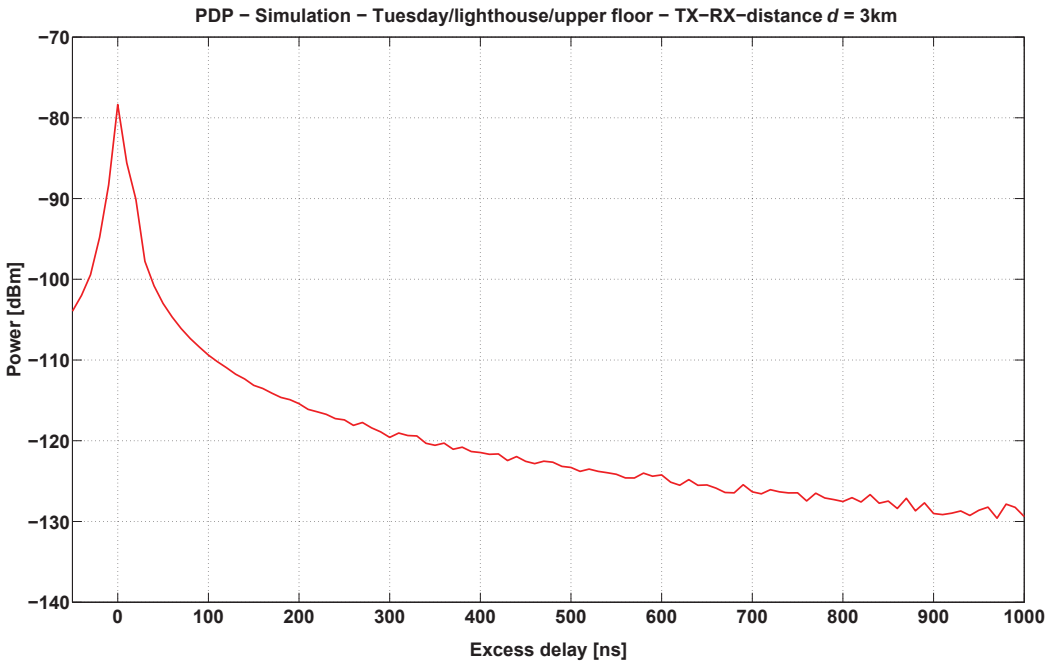

Figure D.17: PDP of the simulation for lighthouse/upper floor for a TX-RX-distance of 3 km

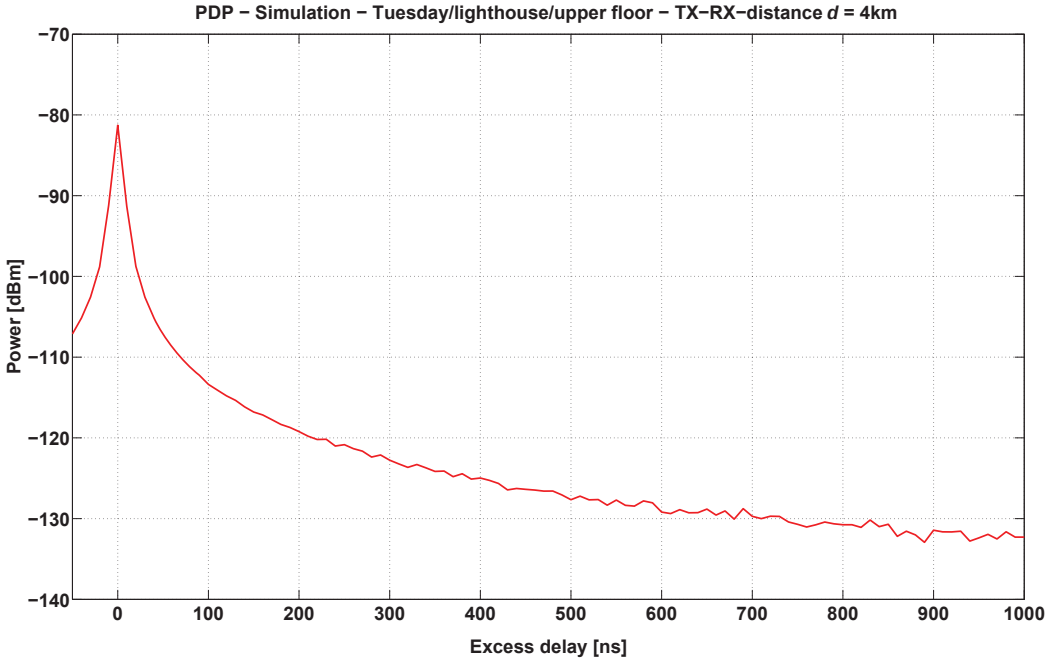

Figure D.18: PDP of the simulation for lighthouse/upper floor for a TX-RX-distance of 4 km

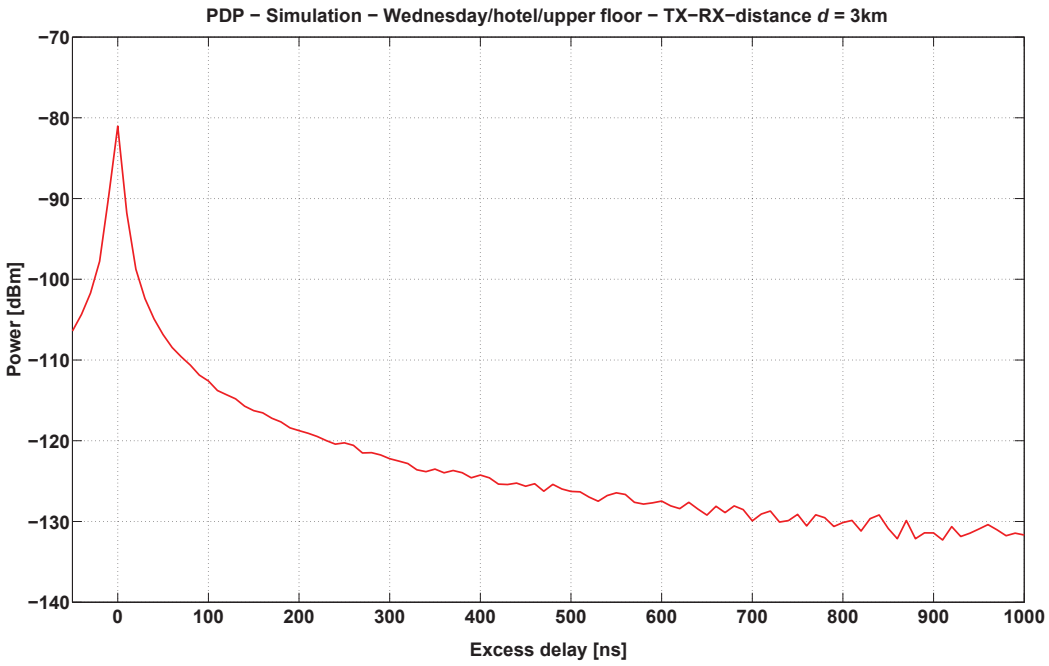

Figure D.19: PDP of the simulation for hotel/upper floor for a TX-RX-distance of 3 km

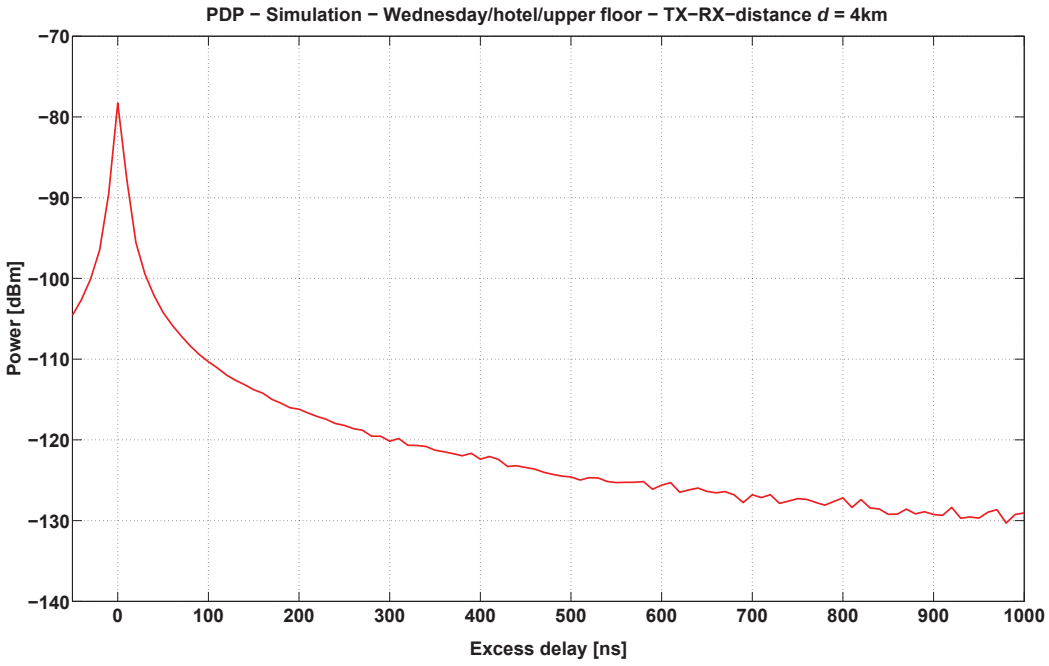

Figure D.20: PDP of the simulation for hotel/upper floor for a TX-RX-distance of 4 km

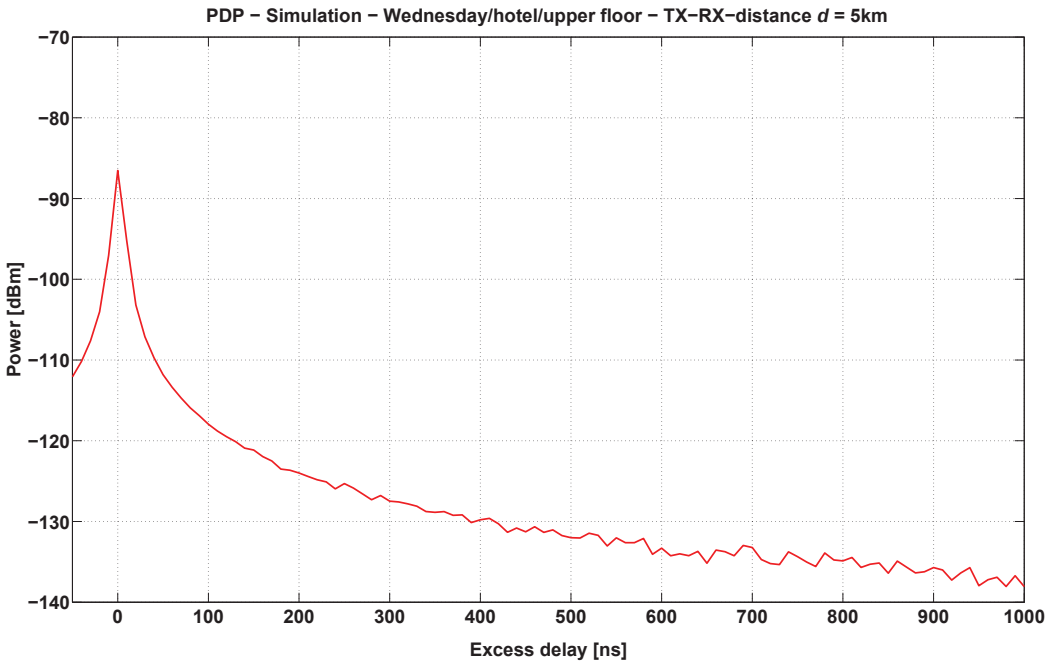

Figure D.21: PDP of the simulation for hotel/upper floor for a TX-RX-distance of 5 km

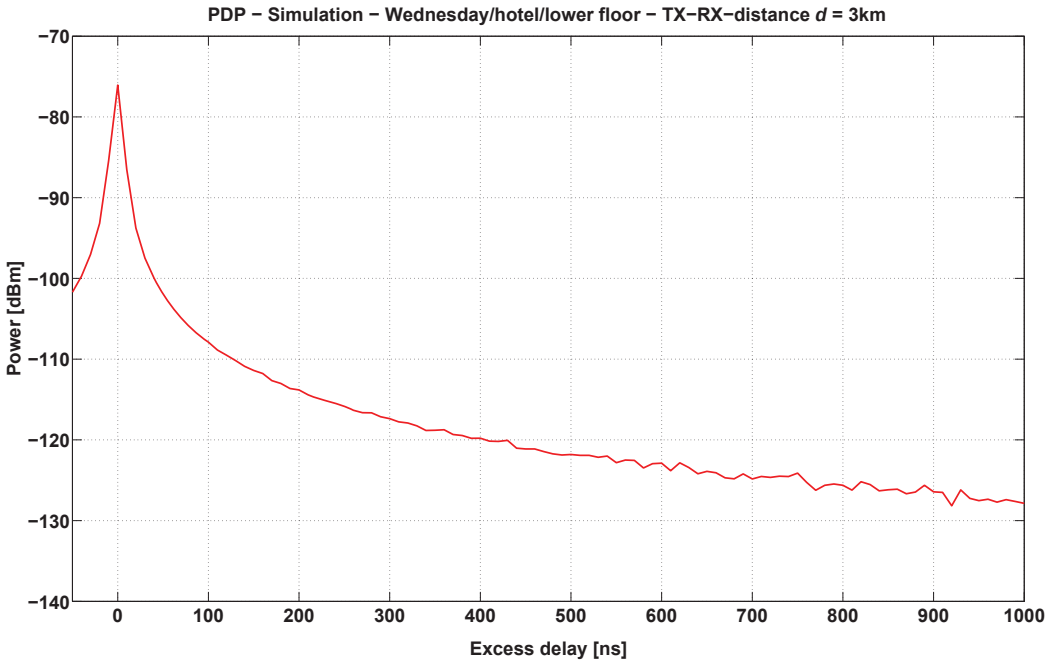

Figure D.22: PDP of the simulation for hotel/lower floor for a TX-RX-distance of 3 km

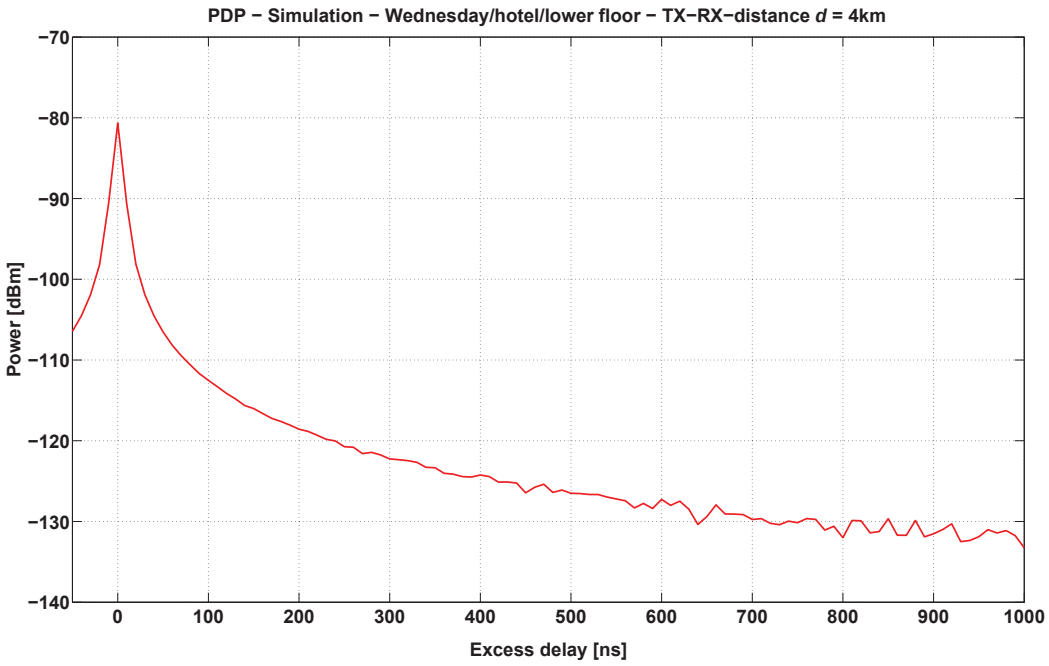

Figure D.23: PDP of the simulation for hotel/lower floor for a TX-RX-distance of 4 km

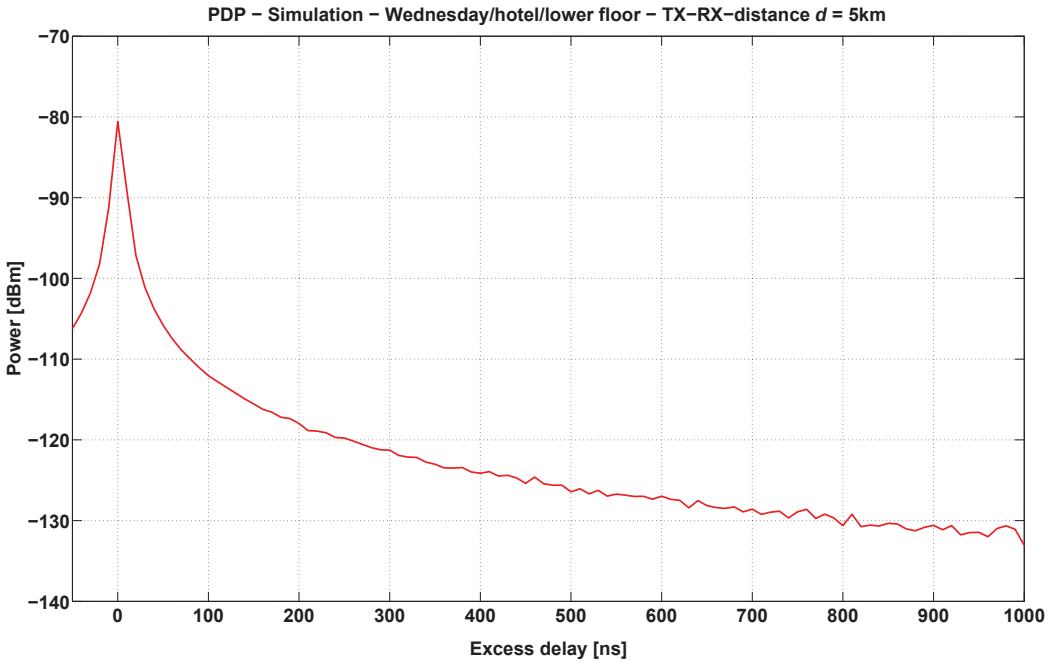

Figure D.24: PDP of the simulation for hotel/lower floor for a TX-RX-distance of 5 km

Comparison between the measurements and the simulations

In this section the comparisons of the PDPs between the measurements and the simulations of Tuesday/lighthouse/upper floor (3 km and 4 km), Wednesday/hotel upper and lower floor, respectively, are illustrated. The TX-RX-distances for the scenarios Wednesday/hotel upper and lower floor are 3 km, 4 km and 5 km, respectively. Particularly, Figures D.26 and D.30 show a very good match between measurements and simulations below 100 ns. After 100 ns, they deviate from each other, because the power of the measurement reaches the noise floor. The remaining PDPs show slightly larger deviations between measurements and simulations, which is expected to be caused by scattering.

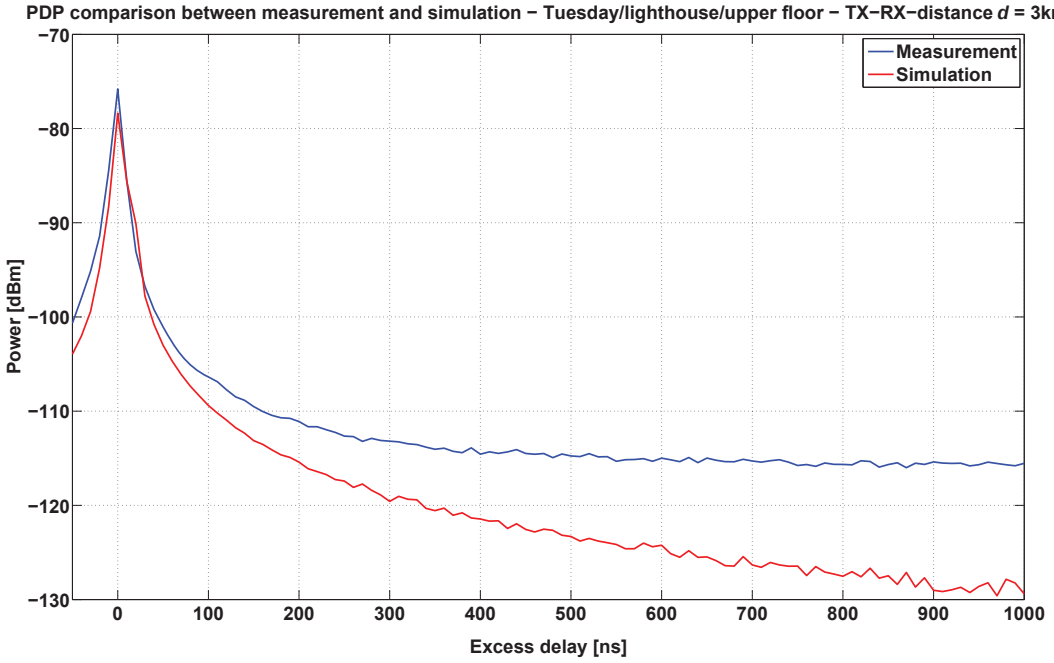

Figure D.25: PDP comparison for lighthouse/upper floor for a TX-RX-distance of 3 km

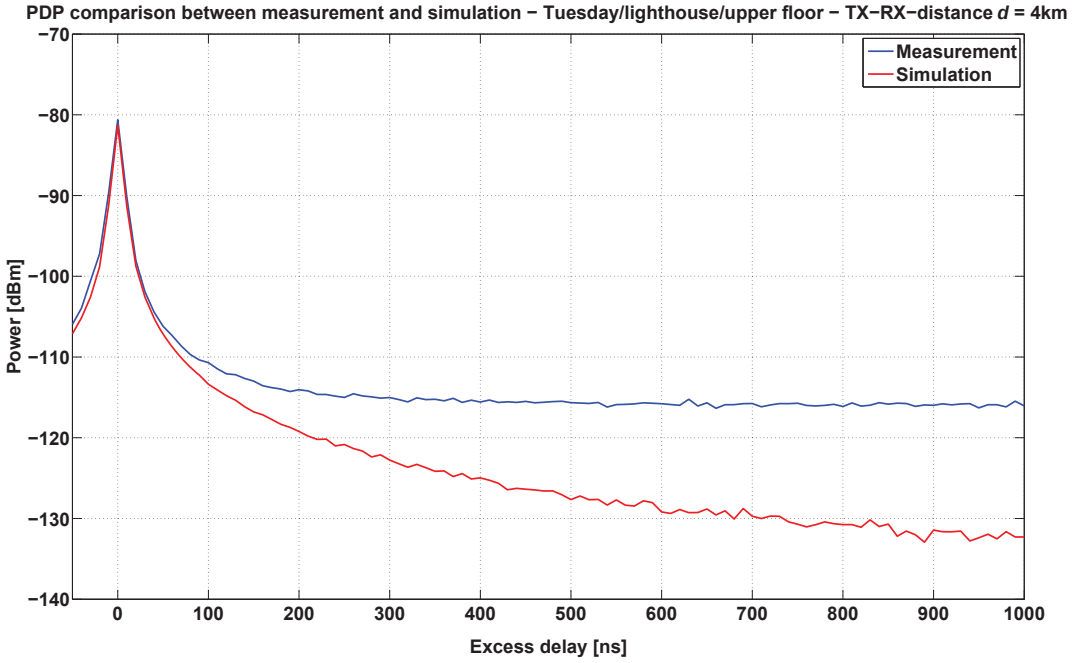

Figure D.26: PDP comparison for lighthouse/upper floor for a TX-RX-distance of 4 km

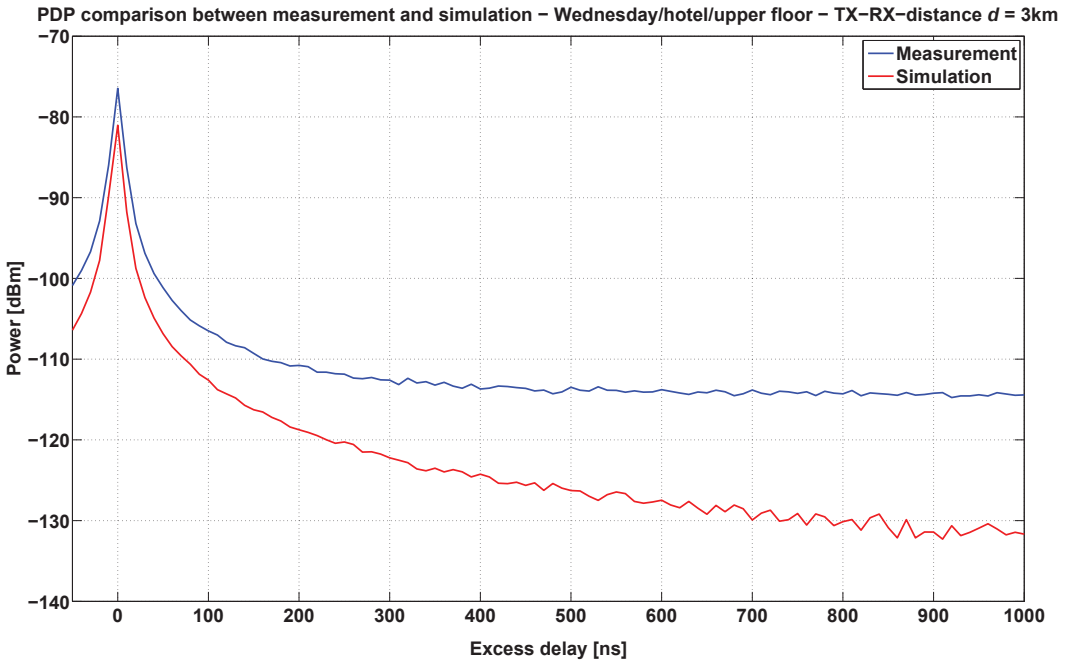

Figure D.27: PDP comparison for hotel/upper floor for a TX-RX-distance of 3 km

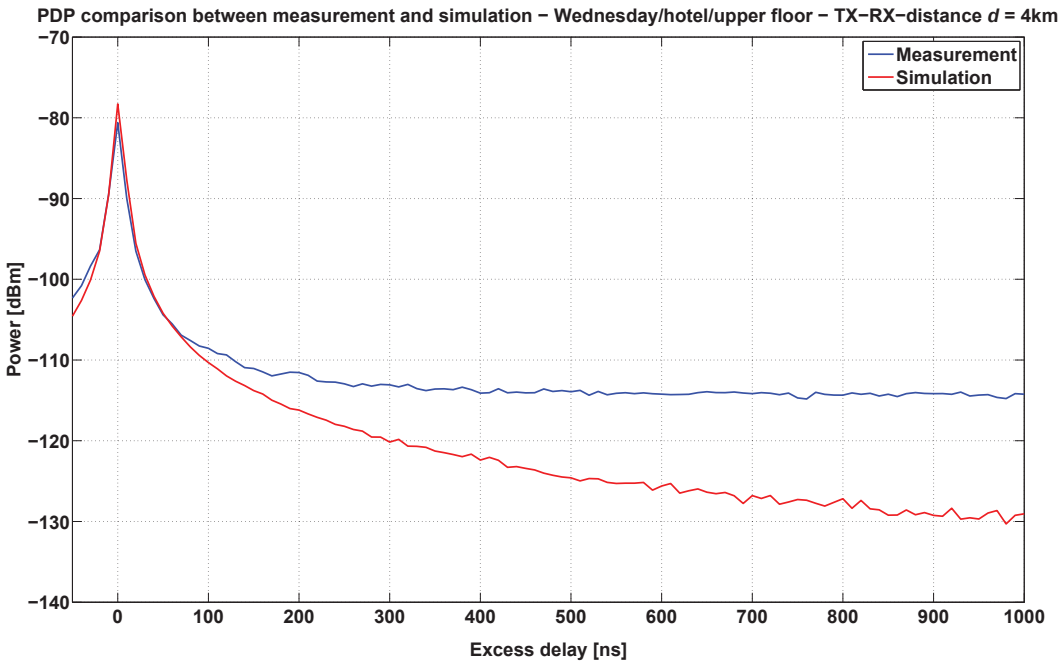

Figure D.28: PDP comparison for hotel/upper floor for a TX-RX-distance of 4 km

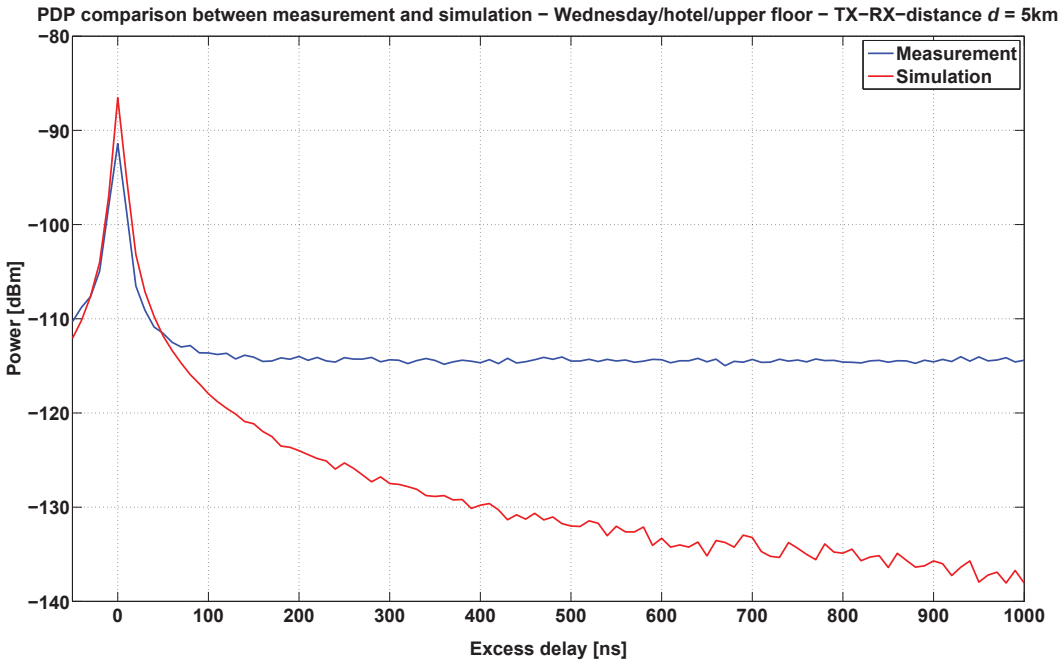

Figure D.29: PDP comparison for hotel/upper floor for a TX-RX-distance of 5 km

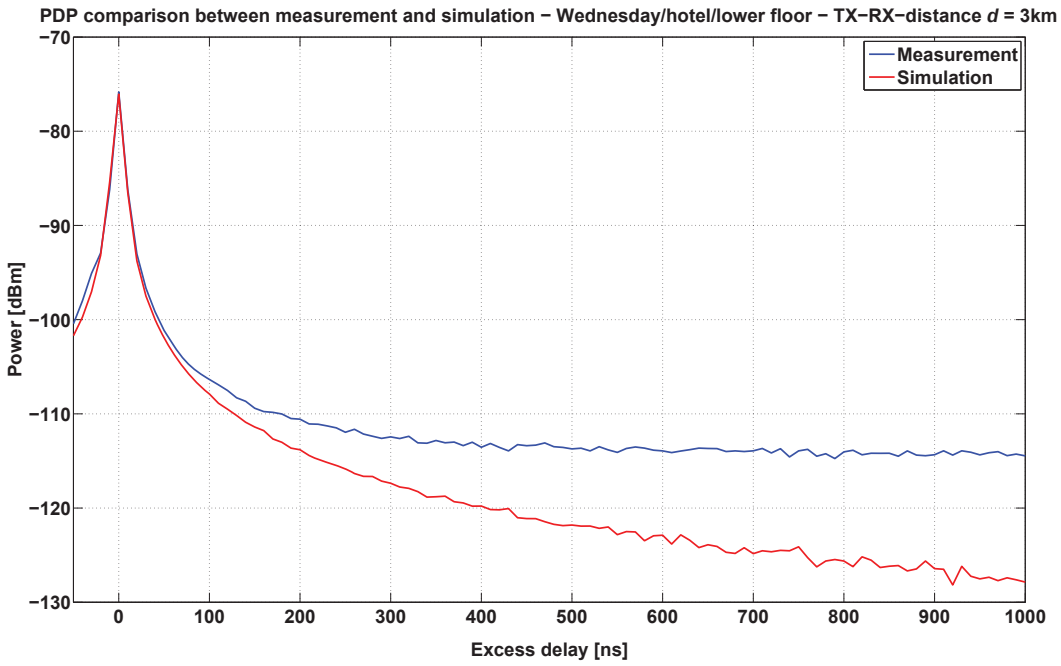

Figure D.30: PDP comparison for hotel/lower floor for a TX-RX-distance of 3 km

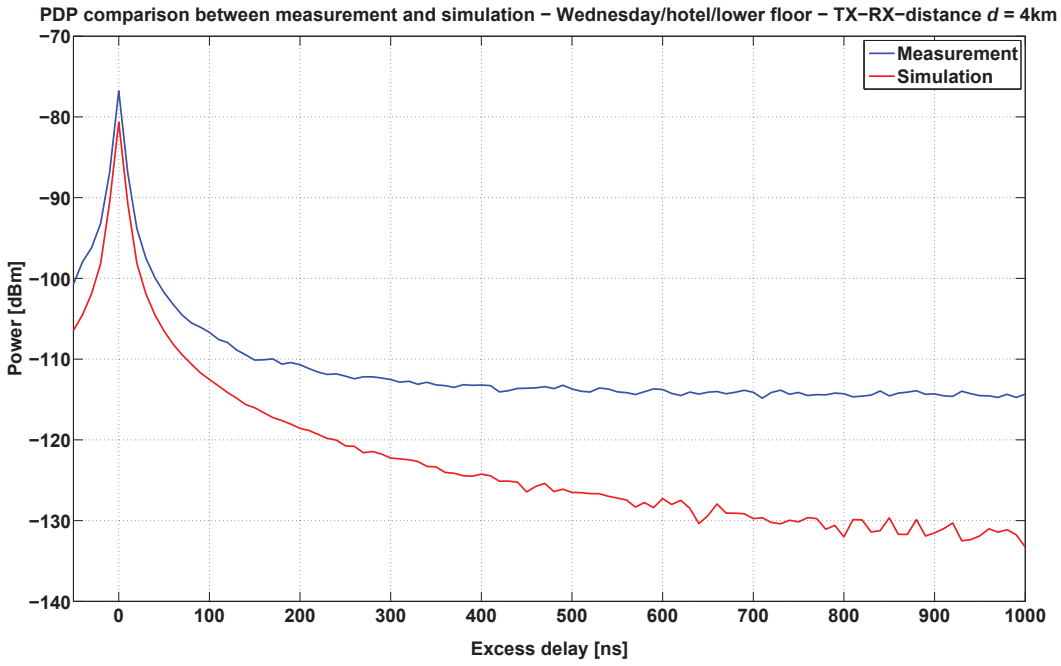

Figure D.31: PDP comparison for hotel/lower floor for a TX-RX-distance of 4 km

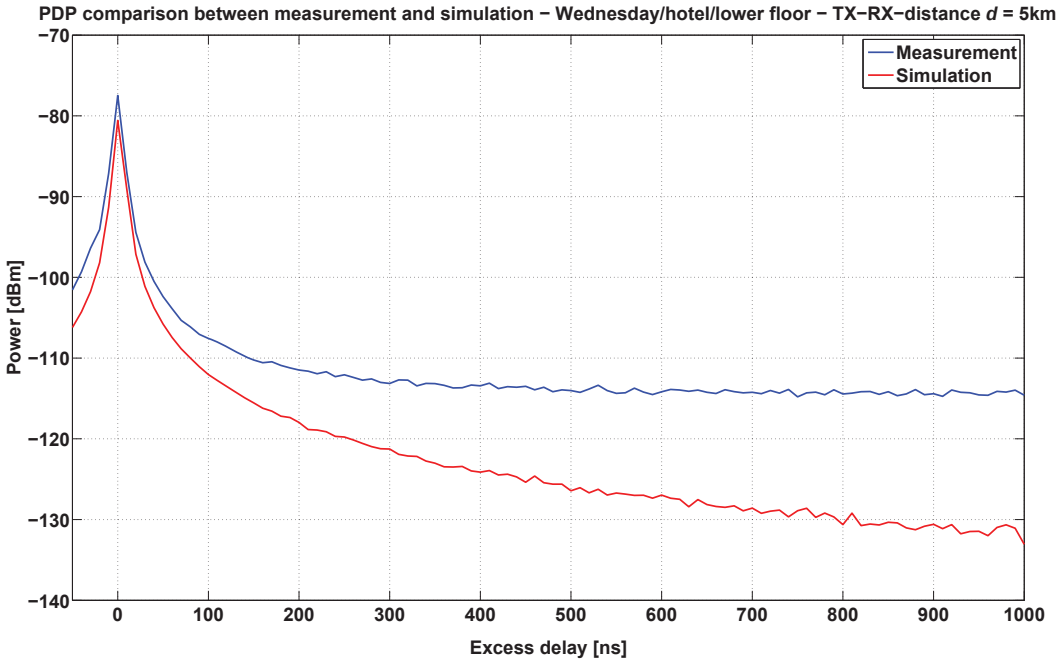

Figure D.32: PDP comparison for hotel/lower floor for a TX-RX-distance of 5 km